COMPUTATION OF RADAR CROSS SECTIONS OF COMPLEX TARGETS
BY PHYSICAL OPTICS WITH MODIFIED SURFACE NORMALS

A THESIS SUBMITTED TO
THE GRADUATE SCHOOL OF NATURAL AND APPLIED SCIENCES
OF
MIDDLE EAST TECHNICAL UNIVERSITY

BY

AHMET CEMAL DURGUN

IN PARTIAL FULFILLMENT OF THE REQUIREMENTS
FOR
THE DEGREE OF MASTER OF SCIENCE
IN
ELECTRICAL AND ELECTRONICS ENGINEERING

AUGUST 2008

Approval of the thesis

COMPUTATION OF RADAR CROSS SECTIONS OF COMPLEX TARGETS BY PHYSICAL OPTICS WITH MODIFIED SURFACE NORMALS

submitted by **AHMET CEMAL DURGUN** in partial fulfillment of the requirements for the degree of **Master of Science in Electrical and Electronics Engineering, Middle East Technical University** by,

Prof. Dr. Canan Özgen
Dean, Graduate School of **Natural and Applied Sciences**   _____

Prof. Dr. İsmet Erkmen
Head of Department, **Electrical and Electronics Engineering**   _____

Prof. Dr. Mustafa Kuzuoğlu
Supervisor, **Electrical and Electronics Engineering, METU**   _____

Examining Committee Members:

Prof. Dr. Gönül Turhan Sayan
Electrical and Electronics Engineering, METU   _____

Prof. Dr. Mustafa Kuzuoğlu
Electrical and Electronics Engineering, METU   _____

Prof. Dr. Gülbin Dural
Electrical and Electronics Engineering, METU   _____

Assist. Prof. Dr. Lale Alatan
Electrical and Electronics Engineering, METU   _____

Dr. Erdal Oktay
EDA Engineering Design and Analysis Inc.,   _____

Date: 29.08.2008

I hereby declare that all information in this document has been obtained and presented in accordance with academic rules and ethical conduct. I also declare that, as required by these rules and conduct, I have fully cited and referenced all material and results that are not original to this work.

Name, Last name: Ahmet Cemal Durgun

Signature   :

ABSTRACT

COMPUTATION OF RADAR CROSS SECTIONS OF COMPLEX TARGETS BY PHYSICAL OPTICS WITH MODIFIED SURFACE NORMALS

Durgun, Ahmet Cemal

M.S., Department of Electrical and Electronics Engineering

Supervisor: Prof. Dr. Mustafa Kuzuoğlu

August 2008, 136 Pages

In this study, a computer code is developed in MATLAB® to compute the Radar Cross Section (RCS) of arbitrary shaped complex targets by using Physical Optics (PO) and Modified PO. To increase the computational efficiency of the code, a novel fast integration procedure for oscillatory integrals, called Levin's integration, is applied to PO integrals.

In order to improve the performance of PO near grazing angles and to model diffraction effects, a method called PO with Modified Surface Normal Vectors is implemented. In this method, new surface normals are defined to model the diffraction mechanism.

Secondary scattering mechanisms like multiple scattering and shadowing algorithms are also included into the code to obtain a complete RCS prediction tool. For this purpose, an iterative version of PO is used to account for multiple scattering effects. Indeed, accounting for multiple scattering effects automatically solves the shadowing problem with a minor modification. Therefore, a special code for shadowing problem is not developed.

In addition to frequency domain solutions of scattering problems, a waveform analysis of scattered fields in time domain is also comprised into this thesis. Instead of direct time domain methods like Time Domain Physical Optics, a Fourier domain approach is preferred to obtain the time domain expressions of the scattered fields.

Frequency and time domain solutions are obtained for some simple shapes and for a complex tank model for differently polarized incident fields. Furthermore, a statistical analysis for the scattered field from the tank model is conducted.

Keywords: Physical Optics (PO), Modified Surface Normal Vectors, Radar Cross Section (RCS), Levin's Integration Method, Fast Integration Methods

ÖZ

DEĞİŞTİRİLMİŞ YÜZEY NORMALLİ FİZİKSEL OPTİKLE KARMAŞIK HEDEFLERİN RADAR KESİT ALANLARININ HESAPLANMASI

Durgun, Ahmet Cemal

Yüksek Lisans, Elektrik-Elektronik Mühendisliği Bölümü

Tez Yöneticisi: Prof. Dr. Mustafa Kuzuoğlu

Ağustos 2008, 136 sayfa

Bu çalışmada, herhangi bir şekle sahip karmaşık geometrili cisimlerin Radar Kesit Alanlarını Fiziksel Optik ve Değiştirilmiş Fiziksel Optik yöntemlerini kullanarak hesaplayan bir MATLAB® programı geliştirilmiştir. Geliştirilen bilgisayar kodunun verimliliğini artırmak amacıyla, Levin integrasyon yöntemi olarak bilinen yeni bir hızlı integral hesaplama yöntemi fiziksel optik integrallerine uygulanmıştır.

Fiziksel Optik yönteminin sıyırma açıları yakınındaki başarımını artırmak ve kırınım etkilerini modelleyebilmek için Değiştirilmiş Yüzey Normalli Fiziksel Optik adı verilen bir yöntem uygulanmıştır. Bu yöntemde, yeni yüzey normalleri tanımlanarak kırınım mekanizması modellenmiş olur.

Radar Kesit Alanını eksiksiz olarak hesaplayan bir bilgisayar programı elde edebilmek için, çoklu saçılmalar gibi ikincil etkiye sahip saçılma mekanizmalarıyla birlikte gölgeleme algoritmaları da programa eklenmiştir. Bu amaçla, çoklu saçılmaları hesaba katabilmek için Yinelemeli Fiziksel Optik yöntemi programa eklenmiştir. Çoklu saçılmaların etkilerinin hesaplanması, Küçük bir değişiklikle, gölgeleme problemini de otomatik olarak çözdüğünden ayrıca bir gölgeleme algoritması geliştirilmemiştir.

Elektromanyetik saçılım problemlerinin frekans bölgesi çözümlerine ek olarak, cisimlerden saçılan dalga şekillerinin zaman bölgesindeki analizleri de bu tezin içeriğine dahil edilmiştir. Burada, saçılan dalgaların zaman bölgesindeki ifadelerin elde edilebilmesi için Zaman Bölgesi Fiziksel Optik yöntemi gibi doğrudan zaman bölgesinde yapılan çözümler yerine, Fourier bölgesi yaklaşımı kullanılmıştır.

Frekans ve zaman bölgesi çözümleri bazı basit cisimler ve bir tank modeli için değişik polarizasyonlu dalgalar kullanılarak elde edilmiştir. Bunlara ek olarak tank modelinden saçılan alanın istatistiksel analizi de yapılmıştır.

Anahtar Sözcükler: Fiziksel Optik, Değiştirilmiş Yüzey Normalleri, Radar Kesit Alanı, Levin İntegrasyon Yöntemi, Hızlı İntegrasyon Yöntemleri

To my Family

ACKNOWLEDGEMENTS

I would like to express my gratitude to my supervisor Prof. Dr. Mustafa Kuzuoğlu for his invaluable guidance and suggestions. Studying with him for the last three years has been a great privilege for me.

I would like to thank my family and to Pınar for their understanding and patience throughout this work. I cannot accomplish this thesis without their support and encouragement. Besides, my special thanks go to my sister for her enormous patience to leaving her alone at home for most of the time in last year.

Also, I would like to express my thanks to my colleagues Volkan Sezgin, Ozan Keysan and Koray Özdal Özkan for their great friendship and for the enjoyable lunches and tea breaks they share with me.

Lastly, I see it as a duty to utter my gratitude to Prof. Dr. Nevzat Gencer for permitting me to use the computer facilities of the Biomedical Research Laboratory, to Dr. Erdal Oktay for his help in complex target modeling and to Dr. Özlem Özgün for the FEM results she has provided.

TABLE OF CONTENTS

LIST OF TABLES

LIST OF FIGURES

CHAPTER 1

INTRODUCTION

Electromagnetic scattering problems have been investigated starting from the late 19th century after the proposal of electromagnetic wave theory. Especially with the widespread usage of radars during World War II, the research on the estimation of scattered field power has been accelerated dramatically [1]. In order to determine the scattered field power rigorously and to generate a common sense between the researchers, a fictitious area was defined for targets to which the scattered field power is proportional. This fictitious area, which is denoted as Radar Cross Section (RCS), is defined as the square of the ratio of the scattered and incident electric fields. The mathematical expression of this definition is given in equation (1.1).

$$\sigma = \lim_{R \to \infty} 4\pi R^2 \frac{|E_s|^2}{|E_i|^2} = \lim_{R \to \infty} 4\pi R^2 \frac{|H_s|^2}{|H_i|^2} \tag{1.1}$$

After defining RCS in mathematical means, thousands of papers have been published by scientists because estimation of RCS opens a very practical way for determining the scattered field for plane wave illumination [1]. In the first papers related to this topic, the RCS estimation problem was solved for simple targets like plates and spheres. However, for real problems, it was impossible to obtain an analytical solution because of the complex geometry of targets. Therefore, new

computational methods were developed to estimate the RCS of complex targets. These computational methods can be classified into two groups such as the exact and approximate solution techniques.

The exact methods, like the Method of Moments (MoM) and the Finite Elements Method (FEM), are rigorous solutions based on the integral and differential equations, respectively. However, some approximations may be performed when solving the integral or differential equations by numerical techniques. In these methods, the target geometry is modeled by small patches and the integral equations are reduced to a set of linear equations that can be solved by standard matrix algebra [3], with the help of some basis or shape functions defined on each patch. Although these methods give very accurate results, they are limited to low frequency and resonant frequency ranges [4]. Since the number of patches increases with frequency, the sizes of the matrices attained in these methods grow too much which result in long computation time at high frequencies.

The approximate methods were proposed to overcome the limitations of exact methods at high frequencies. In these methods, the surface currents induced on the target surface are approximated by using some assumptions such that the scattering problem can be solved quite easily. The first method suggested was the geometric optics (GO) method which is based on the assumption that the energy propagate along rays [1]. Hence, ray tracing is used to compute the reflected waves. The main advantage of this method is its computational simplicity but it gives zero field when no specular points exist [5]. The second method was the physical optics (PO) method (which is the main topic of this thesis and will be discussed in detail in the following paragraphs) which estimates the scattered fields simply by the integration of induced currents found by GO. Although PO improved the results of GO significantly near specular region, the results for grazing angles were still inaccurate.

To improve the performance of optical techniques, two new methods have been developed by Keller and Ufimtsev which were the extensions of GO and PO. The geometrical theory of diffraction (GTD) and the physical theory of diffraction (PTD) were both derived from rigorous solutions to the infinite wedge problem and improved the performance of the previous methods for edge effects [5].

In addition to these methods, some hybrid methods were developed to take the advantage of both exact techniques at low frequencies and approximate techniques at high frequencies. In the hybrid methods for the appropriate portions of the target surface the approximate methods are used to obtain the initial currents named as ''Ansatz'' currents which can be used as effective sources in a surface integral equation formulation problem solved by MoM [6]. By this way the computation time may be increased for complex structures.

Apart from the frequency domain solutions, time domain analysis of scattered waves has also been a very important topic in electromagnetic theory. The finite difference time domain method is a very popular and effective tool for transient analysis of waves in which the differential equation form of the Maxwell's equations are solved by employing the boundary conditions on the discretized target surface [3]. However, similar to MoM and FEM, this method also suffers for the necessity of large number of sampling points at high frequencies. Undeniably, the time domain version of physical optics (TDPO) is also an efficient way for transient response analysis at those frequency ranges [48].

As it can be observed from the introductory discussion given here, many numerical techniques have been developed for electromagnetic scattering problems since the start of widespread application of radars. Even though there are more advanced methods in the literature, PO is still a powerful tool for RCS estimation problems at high frequencies for both frequency and time domain solutions. The main reason of this situation is straightforward application of PO. Moreover, the performance of PO can be improved further, by some

3

modifications or by adding some correction terms, without hindering the simplicity of its implementation [19]-[23]. Furthermore, being a very productive academic topic, PO still remains open for further improvements. That is why we have chosen it as the main concern of this thesis.

1.1   Scope of the Thesis

Since PO is a high frequency technique, the numerical integration may become intractable in terms of computational aspects. Starting from the proposal of PO theory, many techniques have been suggested to compute these integrals. A detailed summary of the earliest methods are given in [7]. Concomitant to the progress in computer technology, more advanced techniques have been suggested by researchers to improve the computational efficiency [8]-[14]. Indeed, the basic motivation behind this study stands on this most intricate part of PO; the numerical integration. A novel fast integration algorithm has been developed for the solution of electromagnetic scattering and RCS estimation problems by PO.

There is another important issue related to PO is that, while applying this theory to complex targets, one should make some extra efforts to account for the effects which cannot be modeled by classical PO approach. Some modifications should be done to improve the performance of PO for edge effects like diffraction and for measuring the polarization dependence of RCS. Moreover, to attain accurate results, the secondary effects like multiple scattering and shadowing should be taken into account. These topics are also included to the scope of this thesis in order to implement a complete tool for RCS prediction of complex targets.

1.2   Outline of the Thesis

The thesis is composed of three main parts involving the aforementioned subjects related to PO method.

Chapter-2 will be devoted to the derivation of a novel integration technique, namely the Levin's Integration Method, and its applications to electromagnetic scattering problems. In this chapter, firstly, the derivation of the PO integral for an arbitrary surface will be discussed. Then a summary of the integration methods that exist in the literature will be given before the novel integration scheme will be proposed for these integrals. Thirdly, a discussion will be done on a modified version of PO (PO with Modified Surface Normal Vectors) which is suggested to improve the performance of PO for edge effects. Lastly, the validity of the novel integration method and modified PO will be proven by experimental results.

In Chapter-3, the additional tools needed for the application of PO to complex targets will be emphasized. In the first part of this chapter, the target modeling technique used in this study will be summarized. Secondly the iterative physical optics method will be examined for multiple scattering and shadowing problems. Lastly, the experimental results will be given and the results will be compared with the ones states in the literature. In this chapter, the literature review for each section will be done separately.

Chapter-4 will focus on time domain analysis of the waveforms of the scattered waves. After a brief literature review on time domain techniques, the derivation of TDPO formula will be handled. Then, Fourier transform approach for finding the time domain expression of the scattered waves will be presented and the experimental results related to time domain methods will be examined.

In Chapter-5, the theories asserted during the thesis will be supported by frequency and time domain numerical experiments performed on simple and

complex scatterers. The results attained will also be compared with the results given in the literature.

Finally in Chapter-6, all of the work done during this study will be summarized. The advantages and disadvantages of the methods suggested in the thesis will be discussed and concluding remarks will be done on the experimental results. Lastly, the future endeavors involving the enhancement of the proposed algorithm will be described with some recommendations.

CHAPTER 2

PHYSICAL OPTICS SOLUTION IN FREQUENCY DOMAIN

2.1 Formulation of the Physical Optics Solution

Similar to the other scattering problems in electromagnetic theory, the frequency domain solution of physical optics approximation may be obtained starting from the Maxwell's equations in the frequency domain. If ω time dependence is accepted for the fields, then the Maxwell's equations in the frequency domain can be written as:

$$\nabla \times \overline{E} = -j\omega\mu\overline{H} - \overline{M} \tag{2.1}$$

$$\nabla \times \overline{H} = j\omega\varepsilon\overline{E} + \overline{J} \tag{2.2}$$

$$\nabla \cdot \overline{D} = \rho_e \tag{2.3}$$

$$\nabla \cdot \overline{B} = \rho_m \tag{2.4}$$

If we apply the curl operator to Equation (2.2), the wave equation for the magnetic field can be obtained.

$$\nabla \times \nabla \times \overline{H} = j\omega\varepsilon\nabla \times \overline{E} + \nabla \times \overline{J}$$

$$\Rightarrow \nabla(\nabla \cdot \overline{H}) - \nabla^2\overline{H} = j\omega\varepsilon(-j\omega\mu\overline{H} - \overline{M}) + \nabla \times \overline{J}$$

$$\Rightarrow \nabla(\frac{\rho_m}{\mu}) - \nabla^2\overline{H} = k^2\overline{H} - j\omega\varepsilon\overline{M} + \nabla \times \overline{J}$$

$$\Rightarrow (\nabla^2 + k^2)\overline{H} = j\omega\varepsilon\overline{M} + \nabla(\frac{\rho_m}{\mu}) - \nabla \times \overline{J} \tag{2.5}$$

Using the Green's function for the magnetic field in free space to solve the wave equation, the following expression is obtained for the scattered magnetic field:

$$\overline{H}^s(\overline{r}) = \frac{-1}{4\pi}\int_V (j\omega\varepsilon\overline{M}(\overline{r}') + \frac{\nabla'}{\mu}\rho_m(\overline{r}') - \nabla \times \overline{J}(\overline{r}'))G_0 dV'$$

$$\Rightarrow \overline{H}^s(\overline{r}) = \frac{-1}{4\pi}\int_V (j\omega\varepsilon\overline{M}(\overline{r}')G_0 - \frac{1}{\mu}\rho_m(\overline{r}')\nabla'G_0 - \overline{J}(\overline{r}') \times \nabla'G_0)dV' \tag{2.6}$$

Now if we convert the volume integral to a surface integral and if we use surface sources instead of volume sources, we obtain the well known Stratton-Chu equation.

$$\overline{H}^s(\overline{r}) = \frac{1}{4\pi}\oint_S (-j\omega\varepsilon\overline{M}_S(\overline{r}')G_0 + \frac{1}{\mu}\rho_{ms}(\overline{r}')\nabla'G_0 + \overline{J}_S(\overline{r}') \times \nabla'G_0)dS' \tag{2.7}$$

In addition to Stratton-Chu equation, by definition, we also have the following three equations:

$$\rho_m = \mu\hat{n} \cdot \overline{H}^T \tag{2.8}$$

$$M_S(\overline{r}') = -\hat{n} \times \overline{E}^T \tag{2.9}$$

$$J_S(\overline{r}') = \hat{n} \times \overline{H}^T \tag{2.10}$$

If we substitute the equations (2.8)-(2.10) into (2.7), the magnetic field scattered from an arbitrary illuminated surface is obtained.

$$\overline{H}^s(\overline{r}) = \frac{1}{4\pi} \oint_S (j\omega\varepsilon(\hat{n}\times\overline{E}^T)G_0 + (\hat{n}\cdot\overline{H}^T)\nabla'G_0 + (\hat{n}\times\overline{H}^T)\times\nabla'G_0)dS' \quad (2.11)$$

Here, $G_0 = \dfrac{e^{-jk|\overline{r}-\overline{r}'|}}{|\overline{r}-\overline{r}'|}$ is the Green's function for the magnetic field in free space.

In case of a PEC scatterer the relations $\hat{n}\times\overline{E}^T = \hat{n}\cdot\overline{H}^T = 0$ will be valid and the scattered magnetic field may be expressed as:

$$\Rightarrow \overline{H}^s(\overline{r}) = \frac{1}{4\pi}\int_S (\hat{n}\times\overline{H}^T)\times\nabla'G_0 dS' \quad (2.12)$$

where S is the illuminated surface.

If we assume that the observer is in the far field and if we substitute the divergence of the Green's function in (2.12) by $\nabla'G_0 = -jk\dfrac{e^{-jk|\overline{r}-\overline{r}'|}}{|\overline{r}-\overline{r}'|}\hat{a}_{(\overline{r}-\overline{r}')}$, the scattered magnetic field is obtained as in equation (2.13).

$$\overline{H}^s = \frac{-jke^{-jkR_0}}{4\pi R_0}\int_S \overline{J}_S \times \hat{k}_s e^{jk\hat{k}_s\cdot\overline{r}'}dS' \quad (2.13)$$

where $R_0 = |\overline{r}|$ is taken and $\hat{k}_s$ is the unit vector in the direction of scattering.

To find the scattered magnetic field and to compute the RCS of the scatterer, one should use equation (2.13). However, up to this point no approximation is assumed related to physical optics. In order to apply the physical optics approximation, equation (2.14) should be employed instead of the surface current density.

9

$$\overline{J}_S = 2\hat{n} \times \overline{H}^i \tag{2.14}$$

As a consequence the physical optics integral for the scattered magnetic field is found to be:

$$\overline{H}^s = \frac{-jke^{-jkR_0}}{4\pi R_0} \int_S (2\hat{n} \times \overline{H}^i) \times \hat{k}_s e^{jk\hat{k}_s \cdot \overline{r}'} dS' \tag{2.15}$$

2.2 Levin's Method for Computing the Integrals of Functions with Rapid Oscillations

The integrand of the physical optics integral obtained in (2.15) is a very oscillatory function especially at high frequencies. Therefore it is very costly to compute these kinds of integrals by simple numerical integration techniques. Some special techniques are needed in order to compute these integrals accurately and effectively. In fact, there are many techniques on this subject in the literature.

The earlier methods suggested to solve this problem were the methods like "Simpson's Rule" and "Newton-Cotes Formulas" which were based on the idea of approximating the integrand as a combination of partial polynomials. These methods might give quite accurate results however they were not satisfactory in terms of computation speed because, too many sampling points were needed to compute the integrals accurately. In order to defeat this difficulty, another algorithm was suggested by Ludwig in which the integration domain is divided into small planar sub domains and on each of them the amplitude and phase components of the integrand are approximated by first degree polynomials [8]. The most significant disadvantage of this method is that, since planar sub domains are used to model the integration domain, too many facets are needed for the accuracy of the computation, especially around the regions where the curvature is

very high when compared with the wavelength. Consequently, this situation leads to a very long integration time.

On the other hand, if curved surfaces are used to model the targets, the computation speed may be increased considerably. In the literature, there are some other methods employing this idea. A good example of these methods is the one proposed by Kobayashi, Hongo and Tanaka. In this method, the integration domain is modeled as a combination of smaller surfaces which are approximated by second degree polynomials and the whole integral can be converted to summation of some easy recursive integrals. By this way, the number of sub domains used in target modeling can be decreased [10].

Apart from the aforementioned techniques, another frequently used method to calculate the integrals of functions with rapid oscillations is Filon's method. In the first step of this method, the integration domain is divided into sub domains. A second degree polynomial is then fitted to the first and last points of each sub domain. After applying integration by parts twice, an algebraic expression is obtained for each sub domain and the summation of these expressions simply gives the result [11]. However, Filon's method is only applicable to the integrals in which the phase variation of the integrand is linear. In cases of nonlinear phase variations, a modified version of this method may be employed in which the integration domain is parametrized by some shape functions on 9 points on the surface. Then the whole integral may be converted to summation of 9 integrals which can easily be expressed in terms of *"error function"* [12].

Another application of Filon's method present in the literature is used in monostatic RCS computation by PO approximation. The solution starts with the mapping of an integration domain, which is expressed analytically, to a rectangular domain with the help of Fubini's theorem. Then depending on the position of the stationary phase points, different approaches are chosen for computation of the integral. In the neighborhood of stationary phase point, the

integral is converted to simpler forms which have already been solved by approximating the amplitude and phase terms of the integrand with second degree polynomials. However, at the points where the phase is not stationary, the surface integral is converted to the summation of oscillatory line integrals by applying Stokes theorem. Finally, these line integrals are computed by Filon's method [13].

An additional improved version of the Filon's method is suggested by Levin. Although Filon's method can be applied to any kind of integrals, the most accurate results are obtained for constant frequency (linear phase variation i.e.) cases [14]. On the other hand the performance of Levin's method for variable frequencies is better.

2.2.1 Levin's Method for One Dimensional Integrals

One dimensional oscillatory integrals may be expressed in the following form:

$$I = \int_a^b f(x)e^{jq(x)}dx \tag{2.16}$$

In this integral, if f is a smooth and nonoscillatory function and if the condition $|q'(x)| \gg (b-a)^{-1}$ is satisfied, then this integral can easily be computed using only a small number of values of f and q' in [a,b].

In his paper, Levin proposed that if f is of the form

$$f(x) = jq'(x)p(x) + p'(x) \equiv L^{(1)}p(x) \tag{2.17}$$

then the integral can be evaluated as

$$I = \int_a^b \frac{d}{dx}(p(x)e^{jq(x)})dx = p(b)e^{jq(b)} - p(a)e^{jq(a)} \tag{2.18}$$

12

where the general solution for p is given as

$$p(x) = e^{-jq(x)} \left(\int_a^x f(t)e^{jq(t)}dt + c \right) \qquad (2.19)$$

Since $p(x)$ is also as oscillatory as the integral in the equation (2.19), it is proved by Levin that if f and q' are slowly oscillatory then, there exists a slowly oscillatory particular solution p_0 of (2.17). (The proof is given in Appendix-A.) Then the result of the integral in (2.16) can be expressed as

$$I = p_0(b)e^{jq(b)} - p_0(a)e^{jq(a)} \qquad (2.20)$$

After this point, an n-point collocation approximation can be made to the function p in terms of some linearly independent basis functions u_k,

$$p_n(x) = \sum_{k=1}^{n} a_k u_k(x) \qquad (2.21)$$

where the coefficients a_k are determined by the n collocation conditions. Now, the problem reduces to finding the coefficients a_k. If we substitute equation (2.21) into equation (2.17), we get

$$L^{(1)}(p_n(x)) = L^{(1)}\left(\sum_{k=1}^{n} a_k u_k(x) \right) = \sum_{k=1}^{n} a_k L^{(1)}(u_k(x)) = f(x) \qquad (2.22)$$

Equation (2.22) can easily be converted to an inverse problem in the form of $Ax = b$, where A, b and x are defined as follows:

$$\begin{bmatrix} L^{(1)}u_1(x_1) & L^{(1)}u_2(x_1) & .... & .... & L^{(1)}u_n(x_1) \\ \vdots & \vdots & \vdots & \vdots & \vdots \\ L^{(1)}u_1(x_n) & L^{(1)}u_2(x_n) & .... & .... & L^{(1)}u_n(x_n) \end{bmatrix} \begin{bmatrix} a_1 \\ \vdots \\ a_n \end{bmatrix} = \begin{bmatrix} f(x_1) \\ \vdots \\ f(x_n) \end{bmatrix} \qquad (2.23)$$

Therefore it is enough to solve this system of linear equations to find the result of the integral given in equation (2.16).

2.2.2 Levin's Method for Two Dimensional Integrals

The two dimensional approach of Levin's method is very similar to one dimensional problem. In this case, a two dimensional oscillatory integral is to be solved which is in the form:

$$I = \int_a^b \int_c^d f(\xi, \eta) e^{jq(\xi, \eta)} d\xi d\eta \qquad (2.24)$$

In order to apply the Levin's method to this kind of integrals, f should be smooth and nonoscillatory as in the one dimensional case. However, the conditions that should be satisfied by q are expanded to two dimensional space.

$$\frac{\partial q}{\partial \xi} = q_\xi \gg (b-a)^{-1}$$
$$\frac{\partial q}{\partial \eta} = q_\eta \gg (d-c)^{-1} \qquad (2.25)$$

In addition to this, a new operator should be defined instead of the operator given in equation (2.17). The new operator is:

$$L(p) = p_{\xi\eta} + jq_\xi p_\eta + jq_\eta p_\xi + (jq_{\xi\eta} - q_\xi q_\eta)p = f \qquad (2.26)$$

Then, by using the equation (2.27)

$$\frac{\partial^2}{\partial\xi\partial\eta}(pe^{jq}) = (p_{\xi\eta} + jq_{\xi}p_{\eta} + jq_{\eta}p_{\xi} + (jq_{\xi\eta} - q_{\xi}q_{\eta})p)e^{jq} \qquad (2.27)$$

one can show that the solution of the integral in (2.24) is equal to

$$\Rightarrow I = p(b,d)e^{jq(b,d)} - p(a,d)e^{jq(a,d)} - p(b,c)e^{jq(b,c)} + p(a,c)e^{jq(a,c)} \quad (2.28)$$

Making the use of n-point collocation, p can be approximated by p_n and the function f may be written as:

$$p = \sum_{k=1}^{n} a_k u_k \Rightarrow L(\sum_{k=1}^{n} a_k u_k)(\xi_j, \eta_j) = f(\xi_j, \eta_j)$$
$$\ni \{u_k\}_{k=1}^{n^2} = \{\xi^i \eta^j \mid 0 \le i, j \le n-1\}$$
$$(2.29)$$

Note that in equation (2.29), two dimensional monomials are used as basis functions.

As a result, the inverse problem to be solved is obtained as

$$\begin{bmatrix} Lu_1(\bar{x}_1) & Lu_2(\bar{x}_1) & \cdots & \cdots & Lu_n(\bar{x}_1) \\ \vdots & \vdots & \vdots & \vdots & \vdots \\ Lu_1(\bar{x}_n) & Lu_2(\bar{x}_n) & \cdots & \cdots & Lu_n(\bar{x}_n) \end{bmatrix} \begin{bmatrix} a_1 \\ \vdots \\ a_n \end{bmatrix} = \begin{bmatrix} f(\bar{x}_1) \\ \vdots \\ f(\bar{x}_n) \end{bmatrix} \qquad (2.30)$$

where each $\bar{x}_i$ is a two dimensional vector.

2.2.3 Levin's Method for Three Dimensional Surfaces

The procedure explained in Section 1.1.2 is only applicable to rectangular domains in two dimensional spaces. However, in radar cross section problems the integration domain is generally an arbitrary three dimensional surface and the integrals are in the form of equation (2.31). Therefore, a special treatment is needed to use Levin's method to RCS problems.

$$I = \int_{\varphi} f(x, y, z) e^{jq(x,y,z)} d\varphi \qquad (2.31)$$

Let $\varphi = (x, y, z)$ be an arbitrary surface in $\Re^3$. It is possible to map any surface φ to a rectangular domain $[-1,1] \times [-1,1]$ in (ξ, η) local coordinates [15]. A mapping example is illustrated in Figure 2-1.
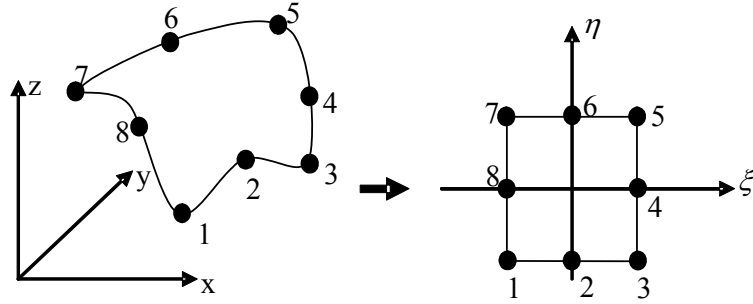
Figure 2-1: Mapping Example

If *x, y and z* components of an 8-noded isoparametric surface are expressed in terms of some shape functions with variables (ξ, η), then such a mapping is possible. Using the collocation points (x_i, y_i, z_i), *x, y and z* components can be written as:

$$x(\xi, \eta) = \sum_{i=1}^{8} x_i N_i(\xi, \eta)$$

$$y(\xi, \eta) = \sum_{i=1}^{8} y_i N_i(\xi, \eta) \qquad (2.32)$$

$$z(\xi, \eta) = \sum_{i=1}^{8} z_i N_i(\xi, \eta)$$

where the shape functions N_i are defined in equations (2.33) and (2.34) [16].

Corner points: $\qquad N_i = \dfrac{1}{4}(1+\xi_i\xi)(1+\eta_i\eta)(\xi_i\xi+\eta_i\eta-1)$ $\qquad\qquad$ (2.33)

Mid points:
$$N_i = \frac{1}{2}(1-\xi^2)(1+\eta_i\eta) \quad if \quad \xi_i = 0$$
$$N_i = \frac{1}{2}(1-\eta^2)(1+\xi_i\xi) \quad if \quad \eta_i = 0$$
$\qquad\qquad$ (2.34)

If these relations are used in a three dimensional oscillatory integral on the surface φ, then the integral given in (2.31) can easily be converted to an integral of the form given in (2.35).

$$I = \int_{-1}^{1}\int_{-1}^{1} f(x(\xi,\eta), y(\xi,\eta), z(\xi,\eta))e^{jq(x(\xi,\eta),y(\xi,\eta),z(\xi,\eta))}\left|\overline{\varphi}_\xi \times \overline{\varphi}_\eta\right| d\xi d\eta \qquad (2.35)$$

By this way, an equivalent expression for equation (2.31) is obtained to which two dimensional Levin's method can be applied directly.

2.2.4 A Special Case: Singularities in Two Dimensional Levin's Method

It was mentioned that, the Levin's method may be applied to oscillatory integrals of the form (2.24) under the condition that the relations given in (2.25) should be satisfied. If these conditions are not satisfied, then the matrix A in the inverse problem of $Ax = b$ becomes very close to a singular matrix. Levin's method does not work properly for those cases. On the other hand, in case where the dimensions of the isoparametric surface are small or the observation point is in the neighborhood of the forward scattering direction, such a problem is inevitable. Therefore, to overcome this problem a special approach should be developed.

Without loss of generality, assume that the condition $q_\xi \gg (b-a)^{-1}$ is not satisfied. Then it can be said that the integrand is not oscillatory in ξ direction. Therefore there is not any need to special techniques to compute the integral in

that direction; the trapezoidal rule may be sufficient to give accurate results. However, the integrand is still oscillatory in the η direction. To compute the integral in that direction Levin's method may be used but in this case the integration will be one dimensional.

Assume that the function F is defined as in equation (2.36).

$$F(\xi) = \int_c^d f(\xi,\eta)e^{jq(\xi,\eta)}d\eta \tag{2.36}$$

If we substitute this equation into the equation (2.24), then we obtain the following integral which can be computed by trapezoidal rule.

$$I = \int_a^b F(\xi)d\xi \tag{2.37}$$

$$\Rightarrow I = \sum_{i=1}^n \frac{\Delta\xi}{2}(F(\xi_{i-1}) + F(\xi_i)) \tag{2.38}$$

where $F(\xi_i)$ is defined as

$$F(\xi_i) = \int_c^d f(\xi_i,\eta)e^{jq(\xi_i,\eta)}d\eta \tag{2.39}$$

If the one dimensional operator given in equation (2.17) is substituted into the equation (2.39)

$$F(\xi_i) = \int_c^d \frac{d}{d\eta}(p(\xi_i,\eta)e^{jq(\xi_i,n)})d\eta = p(\xi_i,d)e^{jq(\xi_i,d)} - p(\xi_i,c)e^{jq(\xi_i,c)} \tag{2.40}$$

is obtained. Now, each $F(\xi_i)$ can be found by one dimensional Levin's method.

If the conditions given in the equation (2.25) are not satisfied in both directions, then the integral can be computed by two dimensional trapezoidal rule assuming that the integrand is not oscillatory.

2.3   Application of Levin's Method to PO Integrals

Levin's method is a very efficient integration method for computing oscillatory integrals and can effortlessly be applied to physical optics integrals given in the equation (2.15). However, to apply Levin's method to physical optics, the oscillatory and non-oscillatory parts of the integrand should be separated properly.

If the incident magnetic field $\overline{H}^i$ is expressed as

$$\overline{H}^i = \overline{H}_0 e^{-jk\hat{k}_i \cdot \overline{r}} \tag{2.41}$$

then, the surface current density on the integration surface takes the following form:

$$\overline{J}_S = 2\hat{n} \times \overline{H}^i \Big|_{S'} = 2\hat{n}' \times \overline{H}_0 e^{-jk\hat{k}_i \cdot \overline{r}'} \tag{2.42}$$

Substituting equation (2.42) into equation (2.15), one can obtain the expression given below.

$$\overline{H}^s = \frac{-jke^{-jkR_0}}{4\pi R_0} \int_S (2\hat{n}' \times \overline{H}_0) \times \hat{k}_s e^{jk(\hat{k}_s - \hat{k}_i) \cdot \overline{r}'} dS' \tag{2.43}$$

Since the oscillatory and non-oscillatory parts of the integrand are separated successfully, the integral in (2.43) is in the form of the integral in (2.31). Nevertheless, Levin's method is still not directly applicable to this integral. The

integration domain should be divided into subdomains modeled by 8-noded isoparametric surfaces. The result is equal to the summation of integrals on these subdomains. Then, following the procedure explained in Section 2.2.3, the integration is mapped onto the (ξ,η) local coordinates for each isoparametric element. Now, Levin's method can directly be applied to compute the integral.

At this point, another important concern arises in terms of computational efficiency of Levin's method. The selection of basis functions and their number may affect the computational cost significantly. Throughout this study the monomials up to 2nd order are used as basis functions, for both one and two dimensional cases, and it is observed that, this selection gives very accurate results with sufficiently low computational cost. In view of the fact that it is out of the scope of this thesis, the effects of using other kinds of basis functions to the results may also be investigated as a future work.

Another important concern regarding the integration is giving the decision of switching from Levin's method to trapezoidal rule. Since each isoparametric element is mapped to the interval [-1,1]x[-1,1] in (ξ,η) domain, the conditions given in (2.25), for applying Levin's method to oscillatory integrals, are converted to

$$q_\xi, q_\eta >> 0.5 \tag{2.44}$$

The experimental results show that choosing q_ξ, q_η 10 times greater than the inverse of the length of the integral gives very accurate results. Therefore, in the cases where $q_\xi, q_\eta > 5$ condition is satisfied, the two dimensional Levin's method is used in this study. If the condition is not satisfied in any direction, then a 10-point trapezoidal integration rule is applied in that direction and the one dimensional Levin's method is applied in the other direction. If the condition is

20

not satisfied in both directions, then a two dimensional trapezoidal rule is conducted over 100 grid points.

2.4 Physical Optics with Modified Surface Normal Vectors

It is a known fact that physical optics approximation gives accurate results only within the neighborhood of the specular region and the degree of error increases as the observer moves away from the specular region. Because physical optics fails to account for the diffraction effects caused by the discontinuities of the target geometry and the discontinuity of the surface currents at the intersections of shadow and lit regions [17]. Therefore, to predict the RCS of the targets more accurately, some modifications are needed to be done. In fact in order to investigate the polarization sensitivity of RCS, these modifications are necessary. This subject may be understood more clearly if the scattering mechanisms at high frequency regimes are explained briefly.

2.4.1 Scattering Mechanisms in High Frequency Regimes

At high frequencies the wavelength becomes very small when compared with the dimensions of the targets and the collective effects of the scattering centers on the targets may be ignored. Therefore, the field scattered from the target can be expressed as a vector summation of the fields scattered from each of the individual scatterers [18]. The scattering mechanisms occur at those scattering centers can be summarized as follows:

- *Specular Reflection:* This is the most dominant scattering mechanism at high frequencies. It forms the main lobe in the specular and forward scattering directions which are illustrated in Figure 2-2.
- *End Region Scattering:* This mechanism models the scattering at the edges of the finite length targets. It contributes to side lobe radiations away from

the specular region. This mechanism with specular reflection can be sufficiently modeled by physical optics approximation.

- _Diffraction:_ Diffraction is due to the induced currents at the edges, tips or the regions where the curvature of the surface changes very rapidly. This mechanism becomes dominant especially away from specular region and is sensitive to polarization changes. Physical optics approximation fails to model diffraction effects. Hence, some modifications are needed. The modified surface normal vectors method is one of the methods found in the literature.

- _Multiple Scattering:_ The interactions between the surfaces of the targets that see each other are modeled by this mechanism. It has secondary effects when compared with the previous 3 mechanisms.
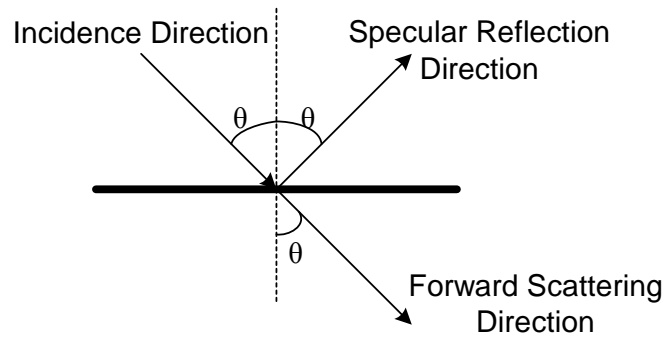
Figure 2-2: Specular Reflection and Forward Scattering Directions

In addition to these mechanisms, there may be diffractions caused by surface traveling waves. However, these are effective at low frequencies.

2.4.2 Modified Surface Normal Vectors

There are several methods in the literature suggested to improve the performance of physical optics for diffraction. The first one of these theories is the "Physical Theory of Diffraction (PTD)" which is suggested by Ufimtsev. In his theory, Ufimtsev expresses the total field as the superposition of the incident, physical

22

optics and diffracted fields. To find the diffracted fields, the incident and physical optics fields are subtracted from the asymptotic solution of the total field [1].

Nearly at the same time with Ufimtsev, Keller proposed his "Geometric Theory of Diffraction (GTD)". In this theory, dissimilar to PTD, the diffracted fields are easily obtained in terms of the incident field and the diffraction coefficients. However, the diffraction coefficients become singular at reflection and shadow boundaries. Also, in case of caustics, the field diverges to infinity. Another disadvantage of this theory is that, the contribution of the diffracted fields cannot be computed for the points lying outside the Keller cone. Therefore, another approach was developed in which equivalent currents are suggested to model the diffracted fields. Since these currents are dependent on the observation point, they are not real physical currents; but only fictitious currents to model the diffraction mechanism [1].

The physical optics with modified surface normal vectors method (will be denoted as Modified PO for the rest of the thesis) has also a similar structure. In this method, the effects of the diffraction coefficients obtained by GTD are modeled by modifying the surface normals according to incidence and observation directions. Thus, the performance of the PO is increased up to the level of GTD by making use of imaginary surface currents [20].

The diffracted fields for the diffraction problem illustrated in Figure 2-3 can be obtained as:

$$\overline{E}^d = \overline{E}^i \overline{\overline{D}} A(\rho_c, r) e^{-jkr} \tag{2.45}$$

In this expression, the dyadic $\overline{\overline{D}}$ contains the diffraction coefficients which are functions of incidence and observation directions. The definition of $\overline{\overline{D}}$ is given in equation (2.46).

23

$$\overline{\overline{D}} = D_s \hat{\theta}_i \hat{\theta}_d - D_h \hat{\phi}_i \hat{\phi}_d \qquad (2.46)$$

where the soft and hard diffraction coefficients are defined as follows:

$$D_s = D_i - D_r$$
$$D_h = D_i + D_r \qquad (2.47)$$

The incident and reflected diffraction coefficients are denoted as D_i and D_r, respectively.
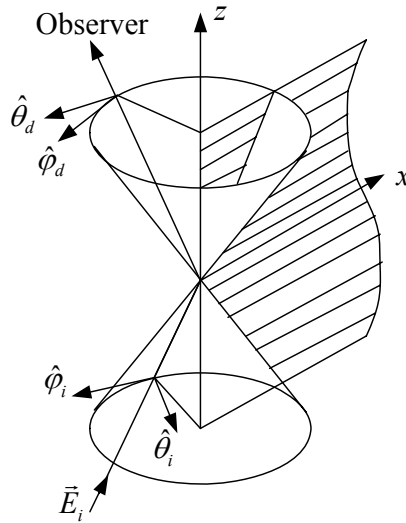
Figure 2-3: The Diffraction Problem and Local Spherical Coordinate System at the Diffraction Point

If the diffraction problem illustrated in Figure 2-3 is solved by the stationary phase method, by following a similar approach to that given in [21] or in [22], the diffraction coefficients for PO and GTD given in Table 1 can be obtained.

Table 1: Diffraction Coefficients for PO and GTD

	PO	GTD
D_i	$-\dfrac{e^{-j\pi/4}}{\sqrt{2\pi k}} \dfrac{\sin\dfrac{\phi_d - \phi_i}{2}}{\cos\dfrac{\phi_d - \phi_i}{2}}$	$-\dfrac{e^{-j\pi/4}}{\sqrt{2\pi k}} \dfrac{1}{\cos\dfrac{\phi_d - \phi_i}{2}}$
D_r	$-\dfrac{e^{-j\pi/4}}{\sqrt{2\pi k}} \dfrac{\sin\dfrac{\phi_d + \phi_i}{2}}{\cos\dfrac{\phi_d + \phi_i}{2}}$	$-\dfrac{e^{-j\pi/4}}{\sqrt{2\pi k}} \dfrac{1}{\cos\dfrac{\phi_d + \phi_i}{2}}$

It can be seen from Figure 2-3 that the only difference between the diffraction coefficients PO and GTD is the sine function in the numerator of the PO diffraction coefficients. In fact, the reason for the failure of PO for modeling the diffraction is that sine function. The modified PO approach is based on the idea of removing this sine function from the numerator of the diffraction coefficients.

In the modified PO method, new surface normal vectors are defined such that the reflection rules are satisfied for both the incident wave and its image with respect to the surface. The definitions of the modified normal vectors in the reflection region are given in equation (2.48) in terms of incidence direction ($\hat{k}_i$), observation direction ($\hat{k}_s$) and the incidence direction of the image field ($\hat{k}_{im}$) which are illustrated in Figure 2-4.

$$\hat{n}_r = \frac{\hat{k}_s - \hat{k}_i}{\left|\hat{k}_s - \hat{k}_i\right|}$$

$$\hat{n}_i = \pm \frac{\hat{k}_s - \hat{k}_{im}}{\left|\hat{k}_s - \hat{k}_{im}\right|}$$

(2.48)

The modified normal vectors can be simplified as $\hat{n}_r = \hat{k}_s = -\hat{k}_i$ and $\hat{n}_i$ becomes a tangential vector to the surface for backscattered RCS calculations [23].
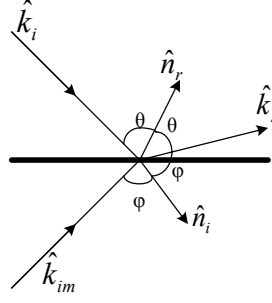
Figure 2-4: Modified Surface Normal Vectors

After the modified normal vectors are defined, the surface current used in PO integral can be modified as follows:

$$\overline{J}_S = 2\left(\hat{n}_r \times \overline{H}^i + \hat{n}_i \times \overline{H}^{im}\right) \tag{2.49}$$

where the image field $\overline{H}^{im}$ can be found by using the image theory.

$$\overline{H}^{im} = -\overline{H}^i + 2\hat{n}(\overline{H}^i \cdot \hat{n}) \tag{2.50}$$

Since this surface current is dependent on the observation and incidence directions, it is not a real current. However, if the stationary phase method is applied to PO with the modified current in (2.49) instead of the current in (2.14), the diffraction coefficients of PO becomes equivalent to GTD diffraction coefficients. Hence, the diffraction mechanism can be modeled by PO without any significant modifications in the classical PO formulation.

It can be observed from equation (2.48) that the normal vector $\hat{n}_i$ may have different signs within the reflection region. In fact this sign change is the trickiest part of applying modified PO to electromagnetic scattering problems. Since the angles that are variables of the diffraction coefficients given in Figure 2-3 are defined locally from the illuminated surface of the scatterer [24], such a sign

change is necessary in order to work in a fixed coordinate system. To distinguish this necessity, a simple two dimensional scattering problem may be investigated.

2.4.3 A Two Dimensional Example

Consider a 2D scattering problem from a strip which is illuminated by a soft polarized incident field as illustrated in Figure 2-5.
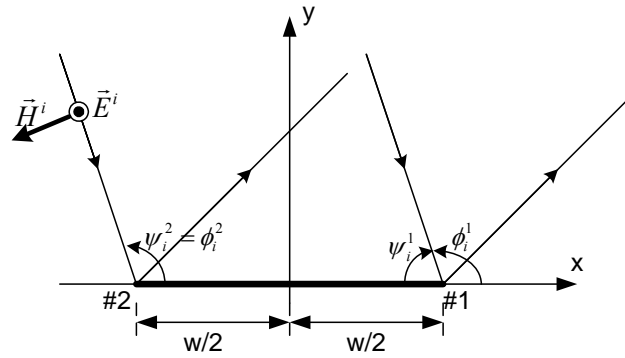
Figure 2-5: 2D Scattering Problem

The incident field is given as

$$\overline{E}^i = \hat{a}_z E_0 e^{jk(x'\cos\phi_i + y'\sin\phi_i)} \tag{2.51}$$

$$\overline{H}^i = (-\sin\phi_i \hat{a}_x + \cos\phi_i \hat{a}_y) \frac{E_0}{\eta} e^{jk(x'\cos\phi_i + y'\sin\phi_i)} \tag{2.52}$$

and the image of the magnetic field with respect to the PEC strip is

$$\overline{H}^{im} = (\sin\phi_i \hat{a}_x + \cos\phi_i \hat{a}_y) \frac{E_0}{\eta} e^{jk(x'\cos\phi_i - y'\sin\phi_i)} \tag{2.53}$$

If we assume that the strip extends to infinity in z direction, then the 3D radiation integral for this problem may be written as

27

$$\overline{H}^s = \frac{-jk}{4\pi}\hat{k}_s \times \int\limits_{-\infty}^{+\infty}\int\limits_{-w/2}^{w/2} \overline{J}_S \frac{e^{-jkR}}{R} dx'dz' \qquad (2.54)$$

where $R = \sqrt{(x-x')^2 + (y-y')^2 + (z-z')^2}$.

If   we   define $|\rho - \rho'|^2 = (x-x')^2 + (y-y')^2$ then   we   have

$R = \sqrt{|\rho - \rho'|^2 + (z-z')^2}$. Substituting this relation into equation (2.54) we obtain

$$\overline{H}^s = \frac{-jk}{4\pi}\hat{k}_s \times \int\limits_{-w/2}^{w/2} \overline{J}_S \int\limits_{-\infty}^{+\infty} \frac{e^{-jk\sqrt{|\rho-\rho'|^2+(z-z')^2}}}{\sqrt{|\rho-\rho'|^2+(z-z')^2}} dz'dx' \qquad (2.55)$$

Knowing the relation given in equation (2.56)

$$\int\limits_{-\infty}^{+\infty} \frac{e^{-ja\sqrt{x^2+t^2}}}{\sqrt{x^2+t^2}} dt = -j\pi H_0^{(2)}(ax) \qquad (2.56)$$

one may obtain the following relation for the scattered magnetic field.

$$\overline{H}^s = \frac{-k}{4}\hat{k}_s \times \int\limits_{-w/2}^{w/2} \overline{J}_S H_0^{(2)}(k|\rho-\rho'|)dx' \qquad (2.57)$$

In the far field we may assume that $\rho \gg \rho'$. Then the Hankel function of the 2$^{\text{nd}}$ kind can be approximated as

$$H_0^{(2)}(k|\rho-\rho'|) \approx \sqrt{\frac{2j}{\pi k}}\frac{e^{-jk\rho}}{\sqrt{\rho}}e^{jkx'\cos\phi_s} \qquad (2.58)$$

28

If this approximation is substituted into (2.57), the expression in (2.59) is found for the scattered magnetic field.

$$\overline{H}^s = \frac{-ke^{j\pi/4}}{2\sqrt{2\pi k}} \frac{e^{-jk\rho}}{\sqrt{\rho}} \hat{k}_s \times \int_{-w/2}^{w/2} \overline{J}_S e^{jkx'\cos\phi_s} dx' \qquad (2.59)$$

Using the definitions of the modified surface normal vectors given in (2.48) one may attain the expressions for these vectors. The geometry for these vectors is illustrated in Figure 2-6.

$$\hat{n}_i = \mp(\cos(\frac{\phi_s - \phi_i}{2})\hat{a}_x + \sin(\frac{\phi_s - \phi_i}{2})\hat{a}_y) \qquad (2.60)$$

$$\hat{n}_r = \cos(\frac{\phi_s + \phi_i}{2})\hat{a}_x + \sin(\frac{\phi_s + \phi_i}{2})\hat{a}_y \qquad (2.61)$$
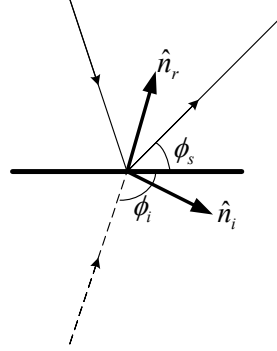

Figure 2-6: The Modified Surface Normal Vectors for 2D Scattering Problem

The surface current generated by the image field may be found by using the expression given for $\hat{n}_i$.

$$\overline{J}_{Sim} = 2\hat{n}_i \times \overline{H}_{im} = \mp \hat{a}_z 2\cos(\frac{\phi_s + \phi_i}{2}) \frac{E_0}{\eta} e^{jkx'\cos\phi_i} \qquad (2.62)$$

If we substitute the surface current expression into (2.59) and employ "+" sign for the upper limit and "-" sign for the lower limit of the integral, the scattered field generated by the image of the incident field is obtained as

$$\overline{H}_{im}^s = \frac{je^{j\pi/4}}{\sqrt{2\pi k}} \frac{E_0}{\eta} \frac{e^{-jk\rho}}{\sqrt{\rho}} \frac{1}{\cos(\frac{\phi_s - \phi_i}{2})} \cos(k\frac{w}{2}(\cos\phi_i + \cos\phi_s))(\hat{k}_s \times \hat{a}_z) \quad (2.63)$$

Since the relation $\phi_i = \phi_s = \phi$ is valid for backscattering, the expressions for the backscattered magnetic and electric fields are found to be

$$\overline{H}_{im}^s = \frac{je^{j\pi/4}}{\sqrt{2\pi k}} \frac{E_0}{\eta} \frac{e^{-jk\rho}}{\sqrt{\rho}} \cos(kw\cos\phi)(\hat{k}_s \times \hat{a}_z) \quad (2.64)$$

$$\overline{E}_{im}^s = -\eta\hat{k}_s \times \overline{H}_{im}^s = \frac{-je^{j\pi/4}}{\sqrt{2\pi k}} E_0 \frac{e^{-jk\rho}}{\sqrt{\rho}} \cos(kw\cos\phi)(\hat{k}_s \times \hat{k}_s \times \hat{a}_z) \quad (2.65)$$

$$\overline{E}_{im}^s = \hat{a}_z \frac{-e^{-j\pi/4}}{\sqrt{2\pi k}} E_0 \cos(kw\cos(\phi)) \frac{e^{-jk\rho}}{\sqrt{\rho}} \quad (2.66)$$

If we follow the procedure given above, the backscattered electric field generated by the incident field is obtained as

$$\overline{E}_r^s = \hat{a}_z \frac{-je^{-j\pi/4}}{\sqrt{2\pi k}} E_0 \frac{1}{\cos\phi} \sin(kw\cos\phi) \frac{e^{-jk\rho}}{\sqrt{\rho}} \quad (2.67)$$

Since the total scattered field is equal to the sum of the scattered fields generated by the incident field and its image, the expression for the total scattered field in the backscattering direction is attained as given in equation (2.68).

$$\overline{E}^s = -\hat{a}_z E_0 \frac{e^{-j\pi/4}}{\sqrt{2\pi k}} \left(\cos(kw\cos\phi) + kw\frac{j\sin(kw\cos\phi)}{kw\cos\phi} \right) \frac{e^{-jk\rho}}{\sqrt{\rho}} \quad (2.68)$$

The same problem is also handled by Balanis and is solved by using the diffraction coefficients of GTD in [25]. In this solution the contributions of the end points to the scattered field are considered separately. Since there is no any stationary phase point on the strip for backscattering, the contribution from it is neglected. The diffracted fields from the edges 1 and 2 are denoted as $\overline{E}_1^d$ and $\overline{E}_2^d$ respectively. The expression for the scattered electric field is given in (2.69)

$$\overline{E}^d = \overline{E}_1^d + \overline{E}_2^d = \overline{E}^i(Q_1) \cdot \overline{\overline{D}}_1^s \frac{e^{-jk\rho_1}}{\sqrt{\rho_1}} + \overline{E}^i(Q_2) \cdot \overline{\overline{D}}_2^s \frac{e^{-jk\rho_2}}{\sqrt{\rho_2}} \tag{2.69}$$

where the diffraction coefficient for soft polarization is given as

$$\overline{\overline{D}}_n^s = \hat{a}_z \hat{a}_z \frac{e^{-j\pi/4}}{\sqrt{2\pi k}} \left(\frac{-1}{\cos(\frac{\psi_n^s - \psi_n^i}{2})} + \frac{1}{\cos(\frac{\psi_n^s + \psi_n^i}{2})} \right) \tag{2.70}$$

Then the contributions from each edge is calculated as

$$\overline{E}_1^d = -\hat{a}_z E_0 \frac{e^{-j\pi/4}}{2\sqrt{2\pi k}} (1 + \frac{1}{\cos\phi}) e^{jkw\cos\phi} \frac{e^{-jk\rho}}{\sqrt{\rho}} \tag{2.71}$$

$$\overline{E}_2^d = -\hat{a}_z E_0 \frac{e^{-j\pi/4}}{2\sqrt{2\pi k}} (1 - \frac{1}{\cos\phi}) e^{-jkw\cos\phi} \frac{e^{-jk\rho}}{\sqrt{\rho}} \tag{2.72}$$

Finally, the expression for the total diffracted field which is equal to the sum of the diffracted fields from two edges is obtained to be identical to expression given in (2.68).

$$\overline{E}^d = -\hat{a}_z E_0 \frac{e^{-j\pi/4}}{\sqrt{2\pi k}} \left(\cos(kw\cos\phi) + kw \frac{j\sin(kw\cos\phi)}{kw\cos\phi} \right) \frac{e^{-jk\rho}}{\sqrt{\rho}} \tag{2.73}$$

31

Therefore we may conclude that the sign change in the modified surface normal vector $\hat{n}_i$ yields the correct result.

If we solve the scattering with the same geometry illustrated in Figure 2-5 but with a hard polarized incident field, then using the diffraction coefficient given in (2.74) the diffracted fields may be obtained.

$$\overline{\overline{D}}_n^h = \hat{a}_z \hat{a}_z \frac{e^{-j\pi/4}}{\sqrt{2\pi k}} \left(\frac{-1}{\cos(\frac{\psi_n^s - \psi_n^i}{2})} - \frac{1}{\cos(\frac{\psi_n^s + \psi_n^i}{2})} \right) \tag{2.74}$$

The expressions for the diffracted fields are given in the equations (2.75)-(2.77).

$$\overline{E}_1^d = -\hat{a}_z E_0 \frac{e^{-j\pi/4}}{2\sqrt{2\pi k}} (-1 + \frac{1}{\cos\phi}) e^{jkw\cos\phi} \frac{e^{-jk\rho}}{\sqrt{\rho}} \tag{2.75}$$

$$\overline{E}_2^d = -\hat{a}_z E_0 \frac{e^{-j\pi/4}}{2\sqrt{2\pi k}} (-1 - \frac{1}{\cos\phi}) e^{-jkw\cos\phi} \frac{e^{-jk\rho}}{\sqrt{\rho}} \tag{2.76}$$

$$\overline{E}^d = \overline{E}_1^d + \overline{E}_2^d = -\hat{a}_z E_0 \frac{e^{-j\pi/4}}{\sqrt{2\pi k}} \left(\cos(kw\cos\phi) - kw \frac{j\sin(kw\cos\phi)}{kw\cos\phi} \right) \tag{2.77}$$

If the expressions attained in (2.73) and (2.77) are investigated in detail, a very remarkable consequence arises that both fields generate the same RCS even though they are created by differently polarized incident fields. This concern will be discussed in the subsequent sections in detail.

2.5 *Numerical Results*

In this section, the RCS of some simple targets are computed by Levin's integration method and its accuracy is tested by comparing the results with other computation techniques. Moreover, the performance of Modified PO is also

checked on simple geometries. In these experiments both Levin's method and Modified PO are proved to give satisfactorily accurate results.

2.5.1 Results of Levin's Method

The first experiment was conducted on a perfect electric conductor (PEC) flat plate as illustrated in Figure 2-7. In this experiment both monostatic and bistatic RCS of a square PEC plate with side length of 100λ was computed and compared with other methods.

For monostatic case, the plate was illuminated from $\phi = 90°$ and its RCS was computed with respect to θ at 10GHz. The result of the Levin's method was compared with the analytical solution of the physical optics integral of this problem and with the result of Ludwig's method in Figure 2-8. The result of Ludwig's algorithm was obtained by the code POFACETS 3.01 written by David C. Jenn from Naval Postgraduate School California. (For the rest of the thesis the results obtained by Ludwig's method will be denoted as POFACETS 3.01.)
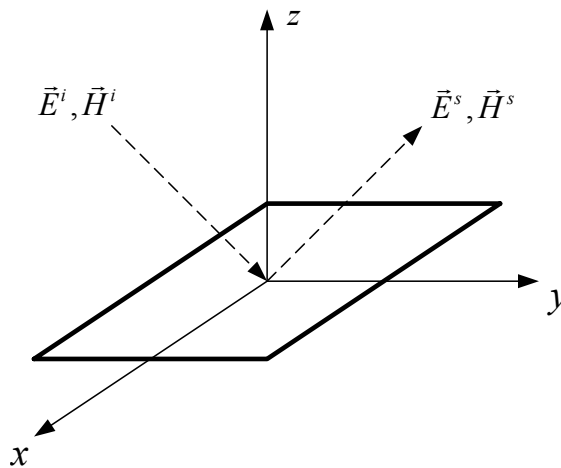
Figure 2-7: Simulation Setup for PEC Plate
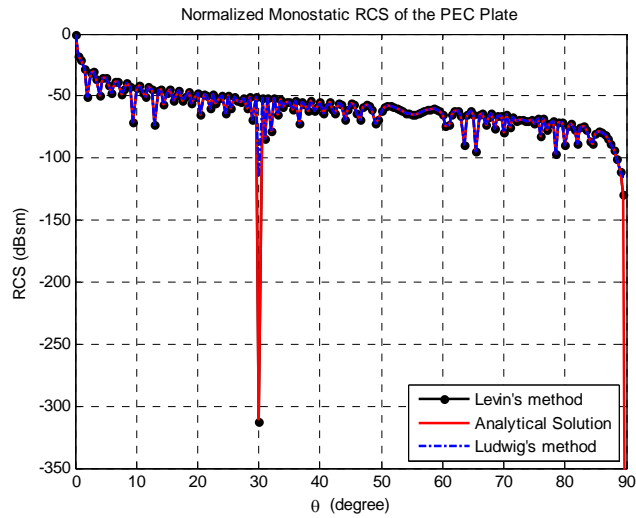
Figure 2-8: Monostatic RCS of a PEC Plate

It can be observed from the figure that, the results obtained by both Levin's method and Ludwig's method perfectly match with the analytical solution. On the other hand, while the plate is modeled with 2 triangular facets in Ludwig's method; only a single patch is used in Levin's method. Hence, Levin's method seems to be more advantageous in the perspective of computational efficiency.

For bistatic case, the plate was normally illuminated and its RCS was computed with respect to θ on the plane $\phi = 90°$. The results of this experiment are shown in Figure 2-9. It can be seen that the results of the Levin's method are very accurate as in the monostatic case.
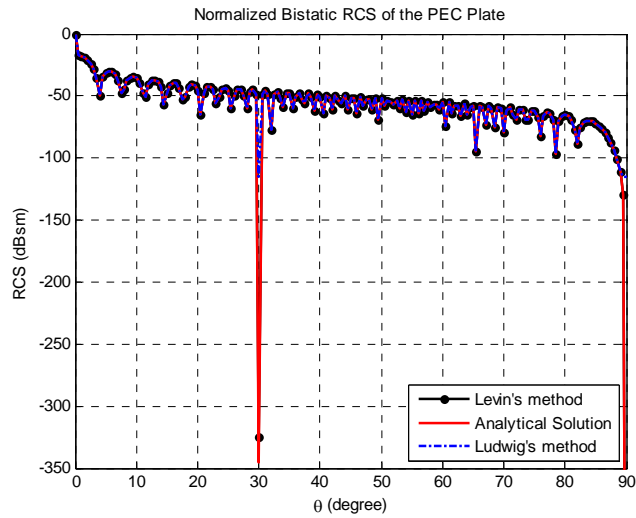
Figure 2-9: Bistatic RCS of a PEC Plate

The performance of Levin's method was proved to be accurate for flat plates. However, in the previous sections it was mentioned that Levin's method is applicable to any surface modeled as a quadrilateral. Indeed, one of the most important advantages of Levin's method is this property. Therefore, for a complete performance check of this novel technique, further experiments are needed to be conducted on curved surfaces.

The second experiment was computation of RCS of a singly curved PEC screen. In this experiment a $5°$ sector of a cylindrical shell was used as curved screen which is shown in Figure 2-10. The radius of the cylinder is equal to 1m and its length is equal to 100λ at 10GHz frequency. The screen was illuminated from $\theta = 0°$ and its bistatic RCS was computed with respect to θ on the plane $\phi = 90°$.
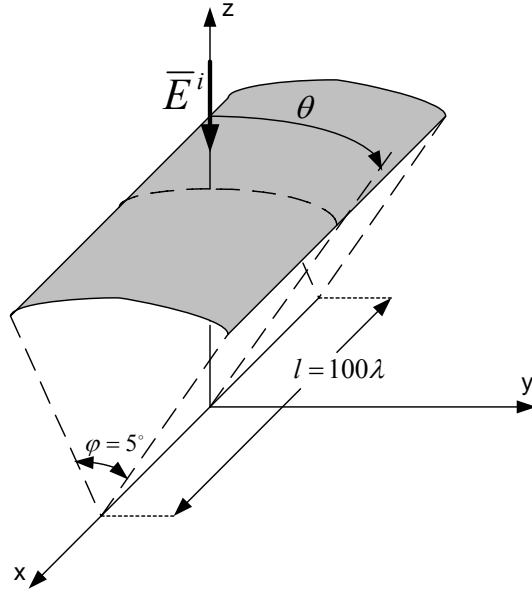
Figure 2-10: Simulation Setup for Singly Curved Screen

The results of the second experiment are shown in Figure 2-11 where the Levin's method solution is compared with the brute force integration solution. It can be observed from the figure that the results are very close to each other. It should also be noted that the cylindrical shell was modeled by a single quadrilateral which makes the computation very efficient.

In order to test the performance of the Levin's method on doubly curved screens, a third experiment was conducted on a spherical PEC shell as shown in Figure 2-12. In this experiment a $6°$ sector (in both curvature directions) of a spherical shell with a radius of 1m was used. The screen was illuminated from $\theta = 90°$, $\phi = 0°$ and its bistatic RCS was computed with respect to ϕ on the cone $\theta = 90°$.
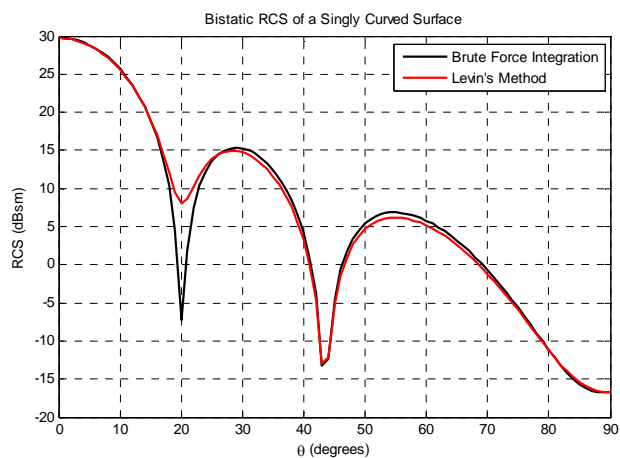
Figure 2-11: Bistatic RCS of a Singly Curved PEC Screen
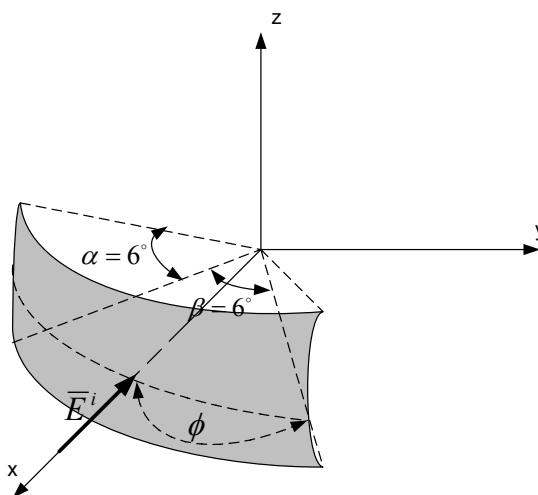
Figure 2-12: Simulation Setup for Doubly Curved Screen

In Figure 2-13, the Levin's method results for doubly curved screen are compared with the results of brute force integration. From the graph, it may be claimed that the results are in a good agreement. Similar to the previous experiment, the screen was modeled with only one quadrilateral.

These experiments confirmed that Levin's method is an effective and efficient technique for the computation of the PO fields even on curved surfaces. In addition to these experiments, one extra experiment was conducted to verify the efficiency and advantage of this method when compared with the methods which are using planar facets to model the integration domain.
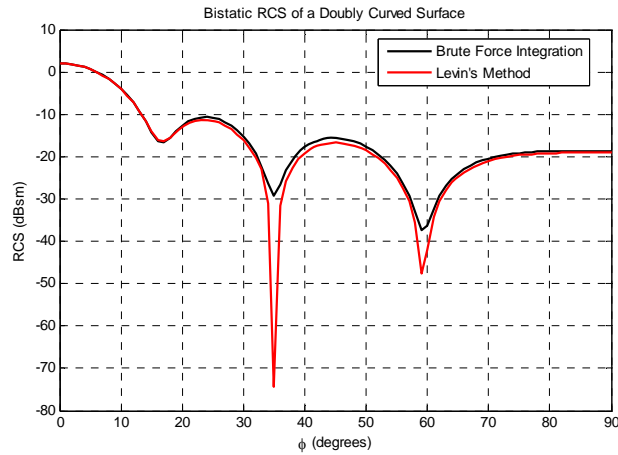
Figure 2-13: Bistatic RCS of a Doubly Curved PEC Screen

The last experiment was conducted on a half cylinder with a radius of 1m and length of 100λ which was illuminated from $\theta = 0°$ as shown in Figure 2-14. In the experiment, the half cylinder was modeled by singly curved screens and planar facets separately. Then the bistatic RCS of the half cylinder was computed on the plane $\phi = 0°$ at 10 GHz and the results belonging to different types of modeling were compared.
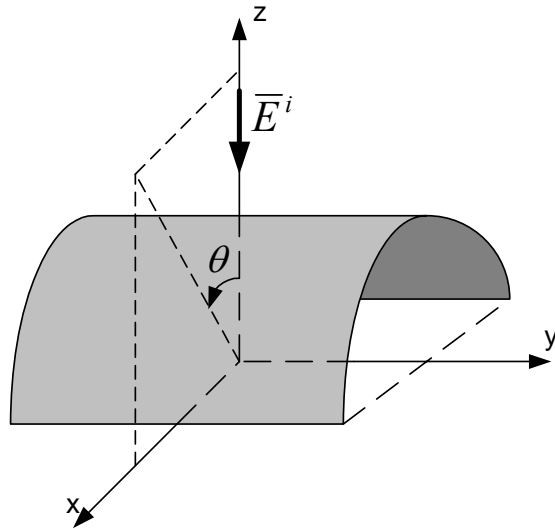
Figure 2-14: Simulation Setup for Half Cylinder

In the last experiment the half cylinder was modeled with singly curved screens and planar facets separately and their performances were compared. In Figure 2-15 the results of this experiment are illustrated. It can be observed that, when compared with the model with 180 flat facets, the results obtained for the model with 360 flat facets are closer to the results of the model with curved facets. Thus the accuracy of the solution increases with the increasing number of facets. However, as a trade off the computation time increases too. This is due to increasing number of integrations as well as the increasing computation time for each facet. (This subject will be discussed in the subsequent paragraphs.). On the other hand accurate results may be obtained when the half cylinder is modeled with 60 curved facets. Therefore, using curved facets instead of flat facets decreases the computation time at least 6 times for the half cylinder. In fact, this consequence is one of the most significant advantages of techniques using curved patches against the techniques using planar patches as mentioned before.
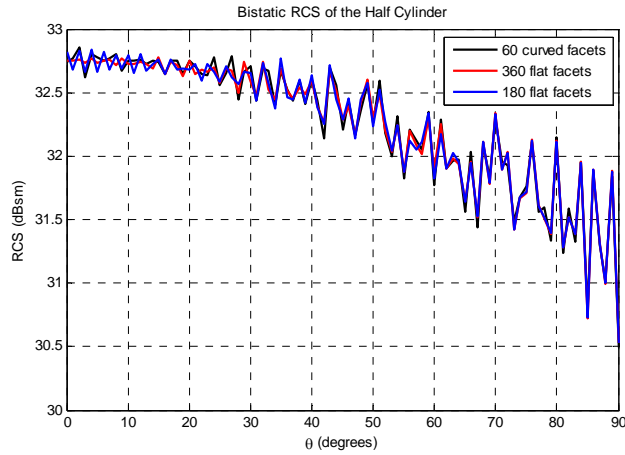
Figure 2-15: The Comparison of the Bistatic RCS of the Half Cylinder Modeled with Different types of Patches

In the previous paragraph it is stated that the computation time for each facet increases with the increasing number of facets. Indeed, this point is the greatest weakness of the Levin's integration method. Since the sizes of the facets decrease with the increasing number of facets, the phase variation within a facet decreases. (This is analogous to decreasing the operating frequency.) Hence, the oscillatory behavior of the PO integral starts to diminish which makes Levin's method inapplicable for small sized facets. As a result, the computation time for each facet increases if the phase of the integrand does not satisfy the conditions given in (2.44).

In addition to the aforementioned drawback of the Levin's method, another weakness of it arises around the forward scattering direction due to the same reasons. In the forward scattering direction the incidence and scattering directions will be the same ($\hat{k}_s = \hat{k}_i$). Since the phase of the integrand of the PO integral is of the form $k(\hat{k}_s - \hat{k}_i) \cdot \bar{r}'$, the phase of the integrand vanishes around forward scattering direction. Thus, Levin's method is not applicable around these regions.

Although Levin's method has some deficiencies, it is still a powerful technique to compute the PO integrals as stated in this section. Additional experimental results of this method for complex targets will be discussed in Chapter-5.

2.5.2 Results of Modified PO

In the previous sections it was declared that PO is unsuccessful in predicting the diffraction effects in scattering problems. To overcome this drawback, modified PO was proposed to improve the performance of PO for diffracted fields. In order to observe the improvement in the performance of PO, some experiments were conducted on simple geometries and the results were compared with the results obtained by a more reliable method like FEM. In these experiments, the same simulation geometry which is illustrated in Figure 2-7 was used

In the first experiment, the monostatic RCS of a PEC square plate, with a side length of 10λ, was computed with respect to θ by both PO and modified PO for different polarizations at 10 GHz. In Figure 2-16 and Figure 2-17 the results obtained in this experiment are compared with FEM results. In this experiment the computations are done at every $5°$.

It may be seen from the figures that, for both polarizations, the modified PO gives enhanced results in comparison with PO. Although the results for $\phi\phi$ polarization are close to the FEM results, modified PO is not successful for $\theta\theta$ polarization. It may also be observed that PO and modified PO give identical solutions for both polarizations as mentioned in the previous section because, to encounter for the polarization effects multiple diffractions should be considered. Moreover for $\theta\theta$ polarization, the fields associated with double diffractions are greater than corresponding $\phi\phi$ polarization [17]. On the other hand, modified PO accounts for only single diffraction effects. Therefore, modified PO cannot give accurate results for $\theta\theta$ polarization.
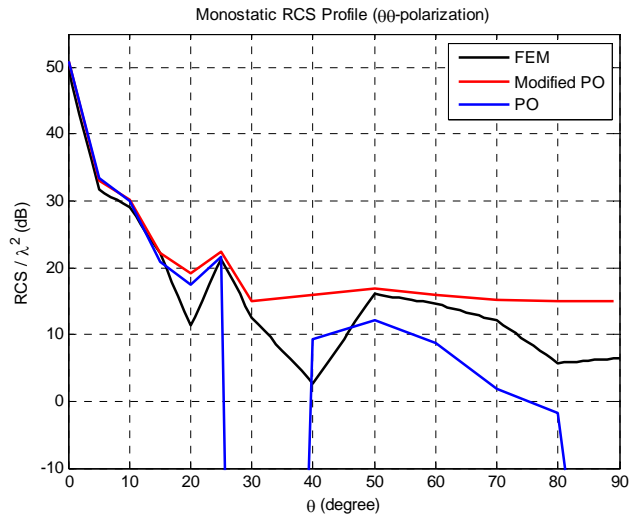
Figure 2-16: Comparison of PO and Modified PO for $\theta\theta$ Polarized Monostatic RCS of a PEC Square Plate
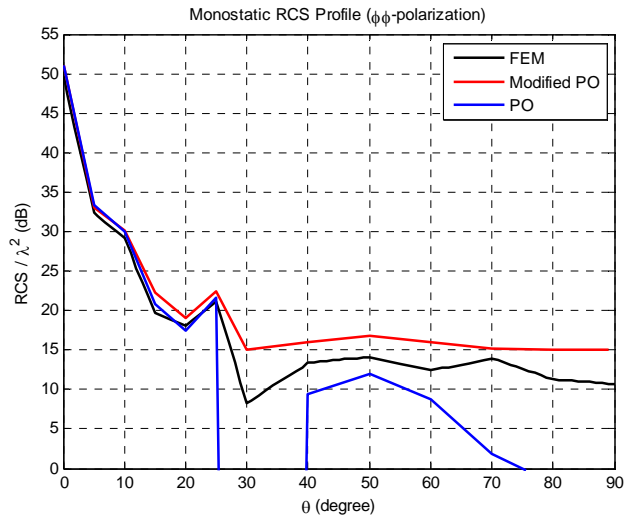
Figure 2-17: Comparison of PO and Modified PO for $\phi\phi$ Polarized Bistatic RCS of a PEC Square Plate

For the bistatic case, the same square PEC plate was used which was illuminated from normal direction and the RCS of the plate was computed with respect to θ on the plane $\phi = 90°$. Similar to the monostatic case, the modified PO was found

to be more thriving than PO. The results of this experiment are illustrated in Figure 2-18 and Figure 2-19.
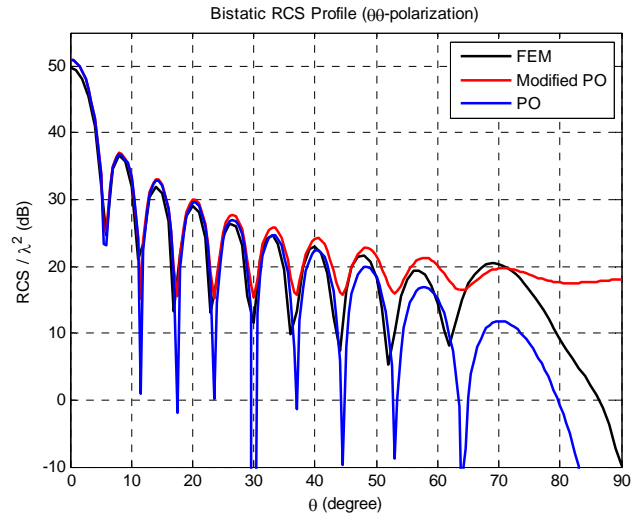

Figure 2-18: Comparison of PO and Modified PO for $\theta\theta$ Polarized Bistatic RCS of a PEC Square Plate
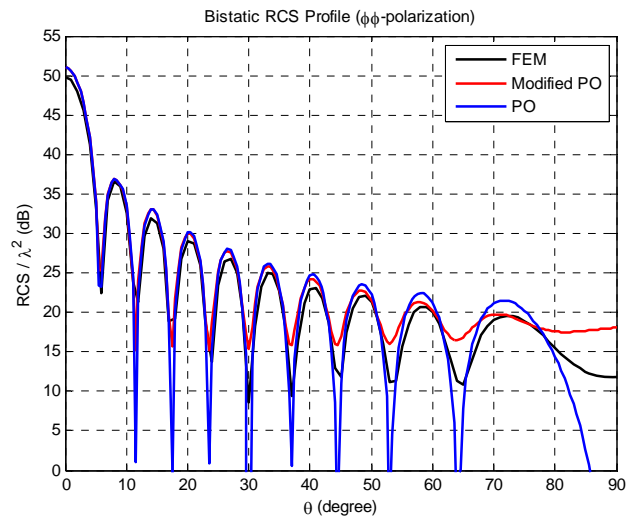
**Figure 2-19: Comparison of PO and Modified PO for $\phi\phi$ Polarized Monostatic RCS of a PEC Square Plate**

43

These figures show that modified PO solutions are closer to FEM solutions. Although the results of modified PO are not in a perfect agreement with the FEM results, PO with modified surface normal vectors can be an effective method to model the diffraction mechanism. Therefore, we may conclude that modified PO is a computationally efficient technique to improve the performance of PO in accounting for diffraction mechanism.

In the previous section it was mathematically shown that the sign of the modified surface normal vector $\hat{n}_i$ should be changed within the integration domain to obtain precise results. It was also discussed that the reason for this sign alteration is due to the change in the coordinate systems defined locally at the diffraction point. Thus, an appropriate algorithm should be determined for sign changing to apply the modified PO to scattering problems.

In this thesis, the sign of the vector $\hat{n}_i$ is determined via the relation given in equation (2.78). In this equation the positions of the integration point and the mid point of the integration point are denoted by $\bar{r}'$ and $\bar{r}'_c$, respectively.

$$\hat{n}_i = sign(\hat{k}_s \cdot (\bar{r}' - \bar{r}'_c)) \frac{\hat{k}_s - \hat{k}_{im}}{\left|\hat{k}_s - \hat{k}_{im}\right|} \qquad (2.78)$$

In order to observe the accuracy of this algorithm, a consistency check was performed where the square plate used in the previous experiments was modeled with different models. In Model-1 only one facet was used to model the square plate while different numbers of facets were used in Model-2, Model-3 and Model-4. These models are illustrated in Figure 2-20.
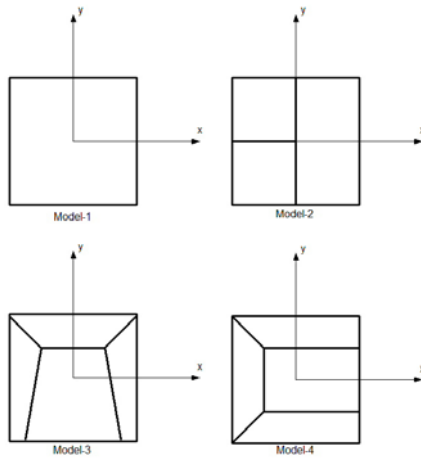
Figure 2-20: Plate Models Used for Consistency Check of Modified PO

Modified PO with the sign change algorithm given in (2.78) was applied to these models separately and it was observed that the results attained by Model-3 was very close to the results obtained by Model-1 and Model-2 which were identical. These results are shown in Figure 2-21. Therefore we may conclude that the algorithm for sign changing gives consistent results independent of facet shape.
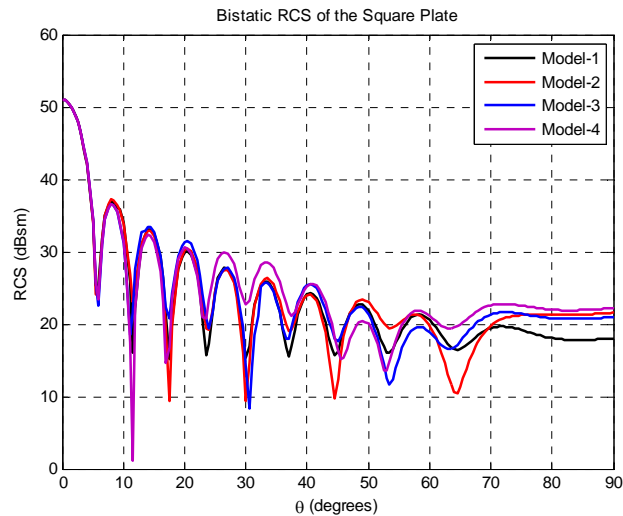
Figure 2-21: Consistency Check Results for Modified PO

CHAPTER 3

APPLICATION OF PHYSICAL OPTICS TO COMPLEX TARGETS

In the previous chapter, the procedure for calculating the scattered field from basic targets such as plates and curved screens was discussed in detail. However, RCS estimation for complex targets needs a special care; more issues should be taken into consideration than discussed in Chapter-2. In fact, calculation of RCS for complex targets involves target modeling and computation of scattered fields due to different scattering mechanisms [26]. Hence for a complete RCS prediction code, all of these subjects should be handled. Since the primary scattering mechanisms were examined in the previous chapter, only target modeling and secondary effects due to geometry of target (such as multiple scattering and shadowing) are going to be discussed in this chapter.

3.1 Target Modeling

In parallel to RCS prediction techniques, lots of target modeling methods have been improved and used for modeling the complex target geometries. Although these techniques may vary in their degree of complexity and modeling time, all share the common limitation of geometric approximation [26].

The first target modeling method seen in the literature was the "body of revolution technique" which was limited to simple targets only. The second technique was the "method of components techniques using primitives". In this method, the complex targets are modeled as a combination of simple shapes such as cone, cylinder, plate and etc. However, this method allows only a coarse modeling of the targets. To avoid these problems, some computer aided design (CAD) tools were started to be used in target modeling [26].

The simplest technique employed by CAD tools was modeling the target surface with triangular facets as in [8] and [27]. Although this method is easy to implement, it suffers from large number of facets and long computation time due to linear approximations of amplitude and phase functions. To overcome this disadvantage, more advanced techniques such as modeling the target surface by quadratic curved patches [28] and biparametric polynomials with restrictions (Bezier surfaces) [29] were developed. Furthermore, in recent years, using nonuniform rational B-splines (NURBS) became very popular in target modeling [30], [31].

Since Levin's method can be applied to curved surfaces by the help of appropriate transformations, it can be applied to targets modeled by curved patches. Nevertheless, for the sake of simplicity, complex targets were modeled by arbitrary shaped large (with respect to wavelength) tetragons instead of quadrilaterals in this thesis study. On the other hand, a mesh generation algorithm for target modeling by quadrilaterals may be handled as a future work to improve the performance of Levin's method.

Surface mesh of a tank model which was used in the experiments is shown in Figure 3-1. In this figure, the tank is modeled by 3276 tetragons of arbitrary size.
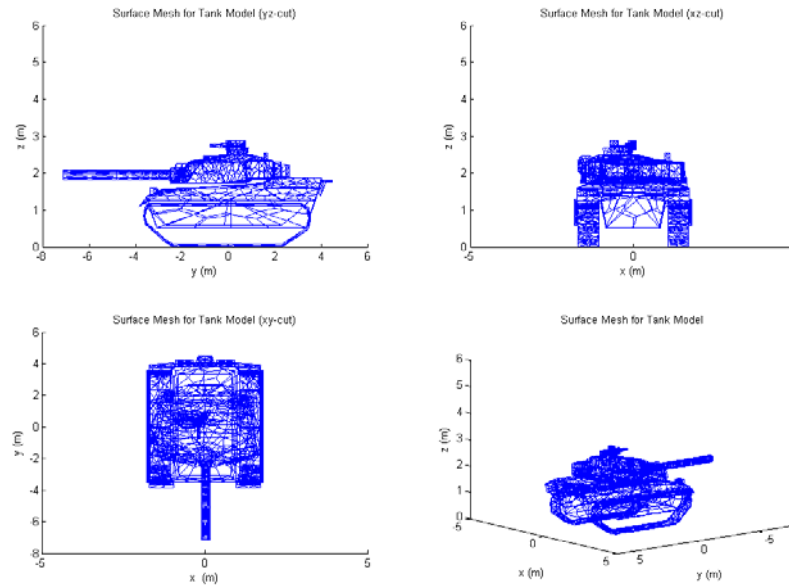
Figure 3-1: Surface Mesh for a Tank Model

3.2 Multiple Scattering

The contribution of multiple interactions between different parts of the target is usually lower than the primary scattering mechanisms namely reflection and diffraction. However for some special geometries such as dihedral or trihedral corner reflectors or cavity like structures, multiple interactions may become dominant. In fact, due to the coupling between neighboring facets, such structures are frequently seen in complex targets (tanks, ships and etc). Therefore for a complete RCS analysis of complex targets, multiple scattering mechanism should also be taken into account.

There are several methods in the literature to handle multiple scattering. The first one of these methods was shooting and bouncing rays method which was proposed by Ling et. al [32]. In this technique, PO is used to calculate the primary scattered fields which are then tracked by ray tracing until they hit to another

facet. When the traced rays hit to another facet, they reradiate to generate the secondary scattered fields. In order to have accurate results with this method, both amplitude and phase changes should be tracked during the ray tracing. Although shooting and bouncing rays technique gives quite accurate results, it needs too much computation time to trace the rays from all of the facets for complex targets.

Another approach, which is used to predict the monostatic RCS of complex targets, employs the image theory to find the contribution of double effects to the scattered field [33]. In this approach, the double effects are separated as facet-facet and facet-edge interactions. For facet-facet interactions, the currents induced on the facets by the incident field are calculated by PO. Then the image source currents through the second facet are obtained by GO. On the other hand, for facet-edge interactions, the equivalent edge currents are obtained from simple diffraction formulas while PO is used for the reflected waves.

In addition to these, current modes can be used for calculating the effects of multiple scattering. In current modes method, the surface currents are approximated by the summation of a finite number of wave functions (exponential functions), with slowly varying amplitude and phase terms, which are called current modes. Then using the fact that a mode is a narrow pass band signal in the spatial frequency domain, the currents on large surfaces can be sampled by a few number of sample points [34].

A fast and very interesting method which was suggested by Boag and Michielssen is based on the observation that the scattering amplitude pattern of a pair of finite scatterers is an essentially bandlimited function of aspect angle and frequency multiplied by common phase factor [35]. In this method, the primary surface currents are obtained from the incident fields by PO. Then these induced surface currents are treated as the new sources of the secondary fields. To reduce the computational complexity, the surface of the scatterer is divided into subdomains by a special domain decomposition formula. Lastly, the scattered field is attained

by the interpolation of the scattering pattern samples at specific angle-frequency points.

Another efficient method which was frequently used in the literature is iterative physical optics (IPO) [36]. At the beginning, IPO was proposed for multiple interactions of surfaces in cavity like structures. However, later investigations have shown that it is also applicable to complex targets. Similar to the approach given in [35], IPO uses the primary induced surface currents as the sources of secondary surface currents and multiple scattering contributions are computed with an iterative treatment.

IPO uses the magnetic field integral equation (MFIE) given in equation (3.1).

$$\bar{J}(\bar{r}) = 2\hat{n} \times \bar{H}^i + 2\hat{n} \times \frac{1}{4\pi} \int_{S'} \bar{J}(\bar{r}') \times \nabla G_0(\bar{r} - \bar{r}') dS' \qquad (3.1)$$

where the gradient of the Green's function is given as

$$\nabla G_0(\bar{r} - \bar{r}') = (\bar{r} - \bar{r}')(jk + \frac{1}{|\bar{r} - \bar{r}'|}) \frac{e^{-jk|\bar{r} - \bar{r}'|}}{|\bar{r} - \bar{r}'|^2} \qquad (3.2)$$

Note that in order to take into account the near field effects in multiple scattering; a far field approximation is not done in the expression (3.2).

The iterative algorithm starts with putting $\bar{J}(\bar{r}') = 0$ on the right hand side of the equation (3.1). This gives us the PO surface current. Then in the next iteration, the PO current obtained in the first iteration is substituted into equation (3.1). Repeating this procedure for N times, the following recursive formula is obtained:

$$\overline{J}_N(\overline{r}) = 2\hat{n} \times \overline{H}^i + 2\hat{n} \times \frac{1}{4\pi} \int_{S'} \overline{J}_{N-1}(\overline{r}') \times \nabla G_0(\overline{r} - \overline{r}') dS' \qquad (3.3)$$

The iterations are truncated at a number N when a stable value for the surface current is obtained. However, for complex targets only one iteration is adequate to estimate the double bounce effects [37].

One disadvantage of this method is that for a rapid convergence, the integration domain should be sampled by at least 4-9 facets per an area of λ^2. Therefore, to speed up the integrations some approximations may be performed. Since the areas of the facets are very small, $\overline{r} - \overline{r}'$ vector can be considered to be constant for all of the points within a facet. If this approximation is combined with the fact that the surface current density is also constant on a facet (Because for flat surfaces $2\hat{n} \times \overline{H}^i$ is constant.), the expression in (3.1) can be rewritten as

$$\overline{J}(\overline{r}) = 2\hat{n} \times \overline{H}^i + 2\hat{n} \times \sum_{i=1}^{M} \overline{J}(\overline{r}_i) \times \overline{R}_i (jk + \frac{1}{R_i}) \frac{e^{-jkR_i}}{4\pi R_i^2} A_i \qquad (3.4)$$

where $\overline{R}_i = \overline{r} - \overline{r}_i'$, $R_i = |\overline{R}_i|$ and the area of the facet is denoted as A_i. In this formulation $\overline{r}_i$ and $\overline{r}$ are the vectors pointing the mid point of each source and illuminated facets. A similar formulation can also be found in [37].

Although the formulation given in (3.4) seems to be very easy to implement, some special care should be taken when combining it with Levin's method. In Chapter-2, it is shown that Levin's method is applicable to large facets and to take the advantage of this, large facets are used for target modeling. However, IPO does not give accurate results for large facets as explained. Thus, a refinement should be done in target model to compute the secondary surface currents. This refinement is achieved by dividing the facets into smaller facets such that the sampling ratio of 4-9 patches per an area of λ^2 is satisfied for most part of the

51

surface. In this procedure, the first step is finding the average facet area of the model. Then each facet is divided into 4 facets until the given sampling condition is attained. An adaptive sampling may also be used to speed up the computation.

After satisfactorily obtaining the secondary surface currents, the scattered field due to these currents is computed by Levin's integration method. If modified PO currents are used in this method, the facet-facet and facet-edge interactions can be approximated by one integration.

An additional important concern about IPO is the shadowing problem. Since these integrations are performed using the principles of PO, shadowing must also be taken into account.

3.3 Shadowing

Shadow region calculation is one of the most essential topics of RCS computation of complex targets. Shadowing is composed of two parts; the self shadowing and the shadowing of one component by another [26]. Self-shadowing is the shadowing of facets that belong to the same object and it depends on the direction of incidence. On the other hand, the shadowing of the facets of one component to the facets of other components is denoted as component/component shadowing.

The self-shadowed facets can be identified by a simple calculation. If the facets do not satisfy the condition (3.5) then they are guaranteed to be in the shadow region. In this expression the incidence direction and the normal of the facet is denoted as $\hat{k}_i$ and $\hat{n}$, respectively. The facets that satisfy the condition (3.5) are signed as candidates to be illuminated. After this point, component/component shadow calculation should be performed.

$$\hat{k}_i \cdot \hat{n} < 0 \tag{3.5}$$

The component/component shadowing problem has been handled by many researchers and several different techniques have been proposed by them. The most popular method in the literature is the ray tracing method. In this method, each candidate facet to be illuminated is tested if it is shadowed by other facets. This is accomplished by special fast algorithms like Möller-Trumbore algorithm. If there exists at least one facet shadowing the other, then each shadowing facet is projected onto the shadowed facet and shadowed portion of the facet is cut out [39]. However, this method is very time consuming. To decrease the computation time of this technique, some accelerated ray tracing algorithms have been proposed in [40] and [41]. In these methods, angle elements called anxels and volume elements called voxels are used to increase the speed of the ray tracing algorithm. In the first method each facet is stored in an anxel which is associated to the spherical coordinates of the normal of the facet. By this way, the facets with negligible contribution to the scattered field can be determined easily. In the second method, the ray-surface intersection test is performed within voxels which are on the direction of incidence.

Although the accelerated ray tracing algorithms seem to be efficient algorithms for shadow region calculation, there is a more efficient way of handling shadowing phenomenon. Since in the forward scattering direction a scattered field that is almost equal and out of phase with the incident wave is produced by the induced surface currents, the sum of incident and scattered fields over the shadowed region almost add up to zero. Thus, keeping the track of multiple scattering can take care of shadowing problem automatically [37]. When keeping the track of multiple scattering an additional condition should be considered together with the condition given in (3.5). For computing the contribution of multiple interactions between the facets (and consequently shadowing), only the points satisfying the following condition should be considered.

$$(\bar{r} - \bar{r}') \cdot \hat{n} < 0 \tag{3.6}$$

3.4 Numerical Results

In order to perceive the accuracy of the IPO method for multiple scattering and shadowing, some experiments are conducted and their results are compared with the results found in the literature.

The first experiment, which is illustrated in Figure 3-2, was the computation of the monostatic RCS of a dihedral corner reflector at 10 GHz frequency. In this experiment, the RCS of a dihedral corner reflector, due to a θ-polarized incident field, with respect to ϕ angle was observed. The dihedral used in this experiment was formed by two square plates of size 12cm.
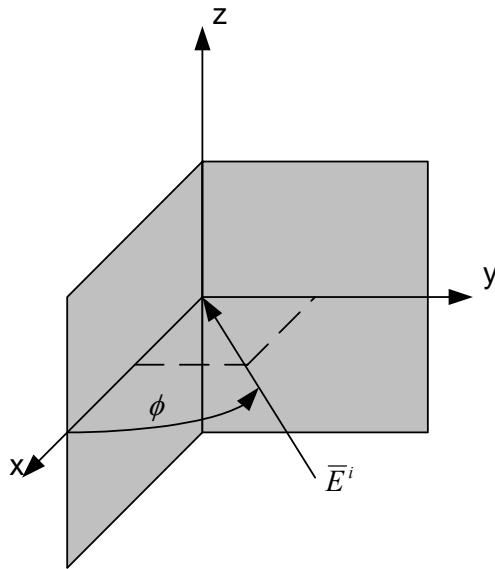
Figure 3-2: Experiment Geometry for Dihedral Corner Reflector

The results of this experiment are given in Figure 3-3. The contribution of multiple scattering can be seen clearly from the figure. Although the results obtained in this experiment do not agree with the results given in [34], they agree well with the results given in [42].
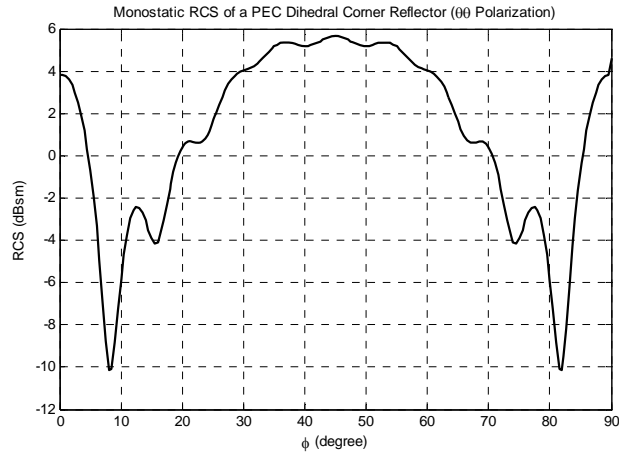
Figure 3-3: The Monostatic RCS of the Dihedral Corner Reflector at 10 GHz
$\theta\theta$ **Polarization**
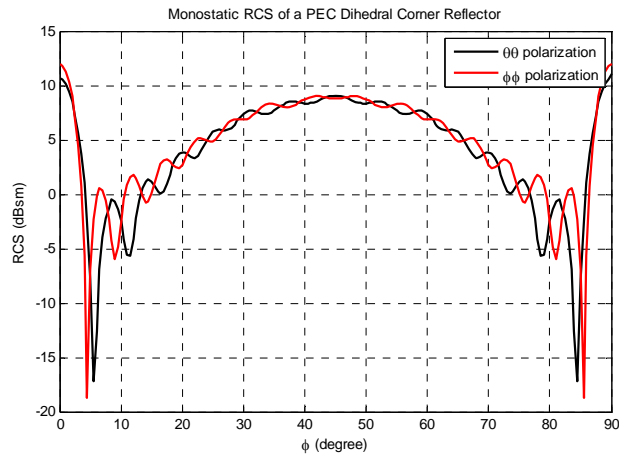
Figure 3-4: The Monostatic RCS of the Dihedral Corner Reflector at 9.4 GHz

To prove the validity of the IPO method implemented in this study, another experiment was conducted with a square dihedral corner reflector of size 5.6088λ at 9.4 GHz. The results of this experiment are shown in Figure 3-4. In the literature, the results related to the same experiment were also given by Griesser et. al. in [43] and there is an excellent match between these results and

55

the ones given here. This experiment proves that IPO method is a powerful tool for the computation of multiple scattering.

Lastly, to show the correctness of our claim about shadowing problem another experiment was done with the simple PEC object shown in Figure 3-5. In this model some of the facets may be fully or partially shadowed by other facets of the target. Therefore, shadowing should be taken into account for an accurate RCS prediction. The results of this experiment are given in Figure 3-6.
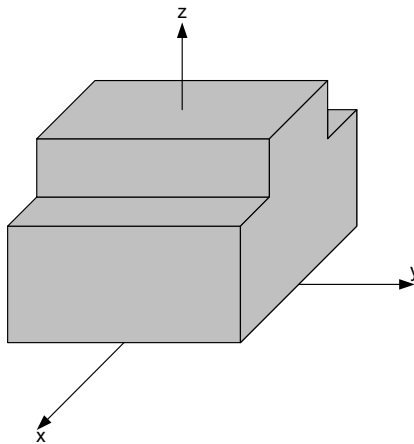

Figure 3-5: Target Model Used for Numerical Multiple Scattering and Shadowing Experiment

It can be observed from Figure 3-6 that the double-bounce scattering and consequently shadowing are satisfactorily modeled by IPO method when compared with RCS computed due to single scattering only. In fact these results are in perfect agreement with the results given in [37]. Hence, it can be concluded that IPO is an efficient and powerful tool to compute the multiple scattering effects together with shadowing for the RCS prediction problems of complex targets.
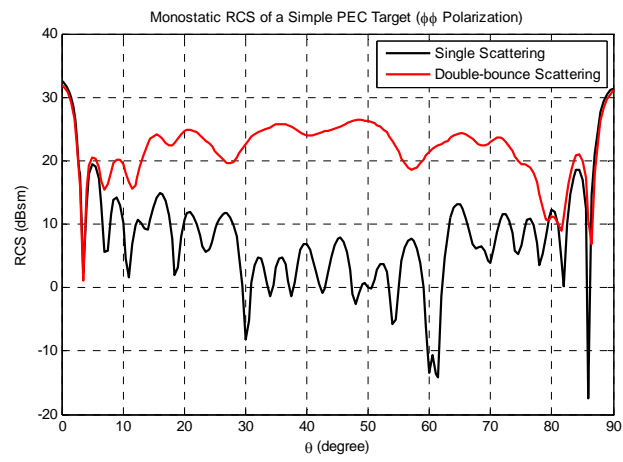
Figure 3-6: Monostatic RCS of the Target Shown in Figure 3-5 at 10 GHz

CHAPTER 4

PHYSICAL OPTICS SOLUTION IN TIME DOMAIN

The steady state scattered field strength can be satisfactorily computed by PO in frequency domain. However, in practice, radar systems have pulsed and modulated (amplitude, frequency and etc.) waveforms where monochromatic source assumption cannot be made. This makes transient analysis of electromagnetic waves necessary especially for large scatterers in which transient effect cannot be neglected [44].

The early methods suggested for transient analysis were based on the idea of transformation of frequency domain solution of the same problem to time domain. Nevertheless, direct time domain solutions were more advantageous than this procedure in terms of convenient handling of nonlinearities, solution efficiency, physical insight and etc. [47]. Hence, the research related to this topic was focused on direct time domain solutions. Foremost solution techniques were the time domain extensions of the exact frequency domain solutions like space-time integral and finite difference time domain (FDTD) methods. Although these methods are very accurate, they suffer from numerical instability, error accumulation with time marching, sample-space truncation error, interpolation error and etc. Moreover, they need extensive computer memory and computation time to solve problems [48].

The paths that PO passed through were similar to ones of formerly mentioned methods. The earliest applications of PO to time domain problems were based on determination of PO impulse response [49], [50]. In [49], a closed form expression is given for the PO impulse response of triangular facets. A similar formulation was also derived by Bölükbaş and Ergin by interpreting the PO integral as a Radon transform [51]. In this paper, the inverse Fourier transform of the frequency domain PO impulse response is interpreted as the Radon transform of the triangular facet, on which the integration is performed; along the direction obtained by the vector addition of observation and the inverse of incidence directions. Likewise, in the formulation given in [50], the time domain expression for the impulse response of a triangular surface is calculated by the inverse Fourier transform of the frequency domain solution. However, the computation is simplified by employing the band limited property of the realistic radar signals; the erroneous low frequency terms and the high frequency terms which do not fall into the bandwidth of the radar signal are not computed.

In the subsequent years, direct time domain PO method was proposed by Sun et. al. which recovered the deficiencies of the exact time domain methods [48]. As a consequence, TDPO became a very popular method for the transient analysis of second order surfaces such as paraboloidal reflector antennas [44]-[46].

4.1 Derivation of the Time Domain PO Integral

For the derivation of TDPO integral, we may start with the time domain Maxwell's equations.

$$\nabla \times \overline{E} = -\frac{\partial \overline{B}}{\partial t} \qquad (4.1)$$

$$\nabla \times \overline{H} = \overline{J} + \frac{\partial \overline{D}}{\partial t} \qquad (4.2)$$

$$\nabla \cdot \overline{D} = \rho_e \qquad (4.3)$$

59

$$\nabla \cdot \overline{B} = 0 \tag{4.4}$$

Since the divergence of $\overline{B}$ is equal to zero, it can be written as a curl of some function called the vector potential.

$$\overline{B} = \nabla \times \overline{A} \tag{4.5}$$

If equation (4.5) is substituted into equation (4.1), the expression for the scalar potential is obtained.

$$\nabla \times \overline{E} = -\frac{\partial}{\partial t}(\nabla \times \overline{A}) \Rightarrow \nabla \times (\overline{E} + \frac{\partial \overline{A}}{\partial t}) = 0$$

$$\Rightarrow \nabla V = -\overline{E} - \frac{\partial \overline{A}}{\partial t} \tag{4.6}$$

Now, substituting equations (4.5) and (4.6) into equation (4.2), one obtains

$$\frac{1}{\mu} \nabla \times \nabla \times \overline{A} = \overline{J} + \varepsilon \frac{\partial}{\partial t}(-\nabla V - \frac{\partial \overline{A}}{\partial t})$$

$$\Rightarrow \nabla(\nabla \cdot \overline{A}) - \nabla^2 \overline{A} = \mu \overline{J} + \mu\varepsilon(-\frac{\partial(\nabla V)}{\partial t} - \frac{\partial^2 \overline{A}}{\partial t^2})$$

$$\Rightarrow \nabla^2 \overline{A} - \mu\varepsilon \frac{\partial^2 \overline{A}}{\partial t^2} = \nabla(\nabla \cdot \overline{A} + \mu\varepsilon \frac{\partial V}{\partial t}) - \mu \overline{J} \tag{4.7}$$

Then by making use of the Lorentz Gauge, the wave equation for the vector potential can be derived from equation (4.7).

$$\text{Lorentz Gauge: } \nabla \cdot \overline{A} + \mu\varepsilon \frac{\partial V}{\partial t} = 0 \tag{4.8}$$

$$\nabla^2 \overline{A} - \mu\varepsilon \frac{\partial^2 \overline{A}}{\partial t^2} = -\mu \overline{J} \tag{4.9}$$

Under the far field conditions, the solution of this wave equation may be approximated as:

$$\bar{A} \approx \frac{\mu}{4\pi} \int_{S'} \frac{\bar{J}(\bar{r}',\tau)}{|\bar{r}-\bar{r}'|} dS' \tag{4.10}$$

where $\tau = \dfrac{|\bar{r}-\bar{r}'|}{c}$ is the time retardation between the source and observation points.

The expression given in (4.10) is denoted as the retarded vector potential. If equation (4.10) is substituted into (4.6), the electric field intensity can be attained.

$$\bar{E} \approx -\nabla V - \frac{\mu}{4\pi} \int_{S'} \frac{\partial \bar{J}(\bar{r}',\tau)}{\partial \tau} dS' \tag{4.11}$$

If there are no free surface charges on the integration surface, then the scalar potential will be equal to zero. Thus, the expression for the electric field intensity will be

$$\bar{E} \approx \frac{-\mu}{4\pi} \int_{S'} \frac{\partial \bar{J}(\bar{r}',\tau)}{\partial \tau} dS' \tag{4.12}$$

For plane waves, the relation between the magnetic and electric field intensities may be written as

$$\bar{H} = \frac{1}{\eta} \hat{a}_R \times \bar{E} \tag{4.13}$$

Then, by using equations (4.12) and (4.13), the time domain expression for the magnetic field intensity at the far field may be obtained.

$$\overline{H}(\overline{r},t) \approx \frac{-1}{4\pi r c} \hat{a}_R \times \int_{S'} \frac{\partial \overline{J}(\overline{r}',\tau)}{\partial \tau} dS' \qquad (4.14)$$

where $\overline{R} = \overline{r} - \overline{r}'$ and $\hat{a}_R$ is the unit vector in the direction of $\overline{R}$.

Equation (4.14) is denoted as the TDPO integral for magnetic field intensity. If this integral is numerically computed by trapezoidal rule, the following formulation may be used.

$$\overline{H}(\overline{r},t) \approx \frac{-1}{4\pi r c} \hat{a}_R \times \sum_{k} \frac{\partial \overline{J}(\overline{r}_k,\tau)}{\partial \tau} \Delta S_k \qquad (4.15)$$

where $\tau = \frac{|\overline{r} - \overline{r}_k|}{c} = \frac{R_k}{c}$.

By this formulation, since the mutual coupling between the points on the surface is ignored, the numerical limitations, such as interpolation error, numerical dispersion error and etc., of the other time domain techniques are avoided. Besides, when compared with the exact time domain techniques, the computation time can be reduced drastically by TDPO [48].

Figure 4-1 illustrates a sample discretization of a rectangular integration domain for TDPO according to the formula given in (4.15). In this problem, in order to calculate the scattered field strength at a point $\overline{R}$ at an arbitrary time, the time retardation due to propagation of the wave should be taken into account. Furthermore, in order to find the transient waveform in a certain interval, the time interval should be divided into smaller subintervals in which the strength of the scattered field is calculated separately. For adequate sampling of the scattered field at high frequencies, very small time steps should be selected which results in long computation times. Additionally, for different observation points, due to the finite time sampling space, some interpolation techniques are required to evaluate

the retarded surface currents [48]. Since any special integration technique is not applied to TDPO during this study, the direct TDPO method is also time consuming although it is more advantageous than the exact time domain methods.
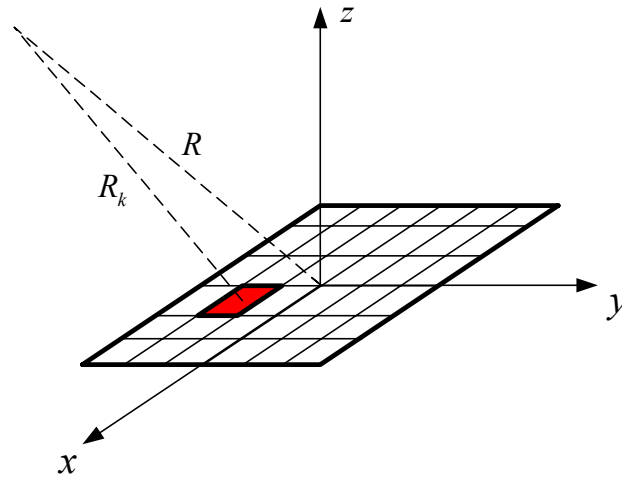

Figure 4-1: Discretization of the Integration Domain for TDPO

Because of the computational drawbacks of TDPO formulation mentioned above, another technique which has already been proposed in the literature was used in this thesis. In this technique, the response of the scatterer is computed via a fast integration method like Levin's method in the frequency domain and the domain response is attained by taking the inverse Fourier transform of the frequency domain response. Although this method has some previously discussed weaknesses, when compared with direct time domain techniques, the Fourier domain solution has been preferred for the sake of shorter CPU time. On the other hand if the speed of TDPO is increased by special integration method, it will be more convenient to employ TDPO for transient response analysis.

4.2 Fourier Domain Solution of TDPO

The Fourier domain solution is the earliest method suggested for time domain scattering problems. As stated by Houshmand et. al. [52], the inverse Fourier transform of the frequency domain response of a scatter is equivalent to the time domain response of the same scatter obtained by direct time domain methods. Due to simplicity and computational efficiency of this method, it has been widely used for time domain analysis of several targets such as reflector antennas and missiles [52] and [53].

Although this method may be seen as an efficient method at the first glance, the scene is more different at high frequencies, especially when dealing with long pulses. It is a known fact that to reconstruct a time domain signal from its samples, it should be sampled at least at its Nyquist rate. Moreover, for sinusoidal signals, a convenient sampling rate is higher than the Nyquist rate; approximately 20 samples within a period. Hence, for long pulses a very long sequence of samples is needed in the discrete time domain. As a consequence, the fast Fourier transform (FFT) occupies a considerable percentage of the computation time. From this discussion it is clear that, some modifications are necessary for transient analysis of target responses via Fourier domain solutions.

In the modified version of Fourier domain solution, the envelope of the signal is sampled instead of full signal. Since the envelope of the signal is composed of only the low frequency terms, the Nyquist rate of the envelope will be decreased dramatically with respect to the one of the real signal. After the envelope detection, the spectrum of the envelope is attained via FFT. The relation between the time domain and frequency domain expressions of the real signal and its envelope is given in equations (4.16) - (4.18). In these equations, the input signal and its envelope are denoted by $x(t)$ and $x_{LP}(t)$ respectively.

$$x(t) = x_{LP}(t)e^{jw_c t} \tag{4.16}$$

$$X_{LP}(w) = FT\{x_{LP}(t)\} \tag{4.17}$$

$$X(w) = X_{LP}(w - w_c) \tag{4.18}$$

Then, the frequency domain target response is computed for each frequency component of the envelope. Even though, this procedure seems to be very straightforward, one should be very careful at this step. Indeed, this is the most tricky and critical point of the modified Fourier domain solution. Since PO is valid only at high frequencies, every frequency component of the envelope should be carried back to high frequency region by multiplying it with the carrier signal. After the modulation of the envelope, the frequency response of the scatterer is computed by FDPO for each associated frequency component of the modulated envelope signal. At the end of this step, the frequency domain output of the system is obtained. Nevertheless, there is still some work to do before passing to the time domain. The frequency domain output should be demodulated by the carrier signal and carried to the base band. Now, if the inverse FFT (IFFT) algorithm is applied to this base band signal, the time domain expression for the output signal is attained. Similar to the input signal, the expressions for the time domain and frequency domain output signals may be written.

$$Y(w) = Y_{LP}(w - w_c) \tag{4.19}$$

$$y_{LP}(t) = IFT\{Y_{LP}(w)\} \tag{4.20}$$

Figure 4-2 illustrates the block diagram of the modified Fourier domain solution (MFDS) discussed in detail.

65
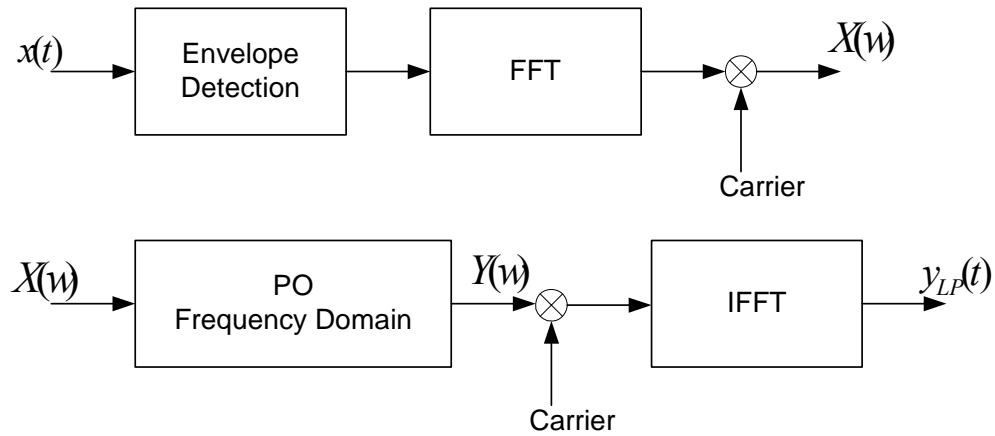
Figure 4-2: Block Diagram of the Modified Fourier Domain Solution

For frequency modulated signals, MFDS may be improved further by introducing auxiliary approximations to decrease the computation time. In these approximations, the signal may be thought as a linear combination of shorter pulses with constant frequencies. Assume that we have a chirp signal as expressed in equation (4.21). The envelope of this incident signal is also illustrated in Figure 4-3.

$$x(t) = A(t)e^{j2\pi f_c t}e^{j\pi\beta t^2} \tag{4.21}$$
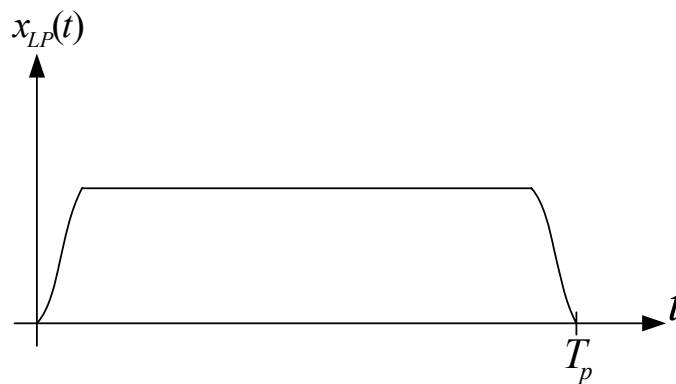
Figure 4-3: The Envelope of the Incident Pulse

If the envelope of the incident pulse is written as a linear combination of shorter pulses with constant frequencies then, the following mathematical relation may be obtained.

$$x_{LP}(t) = \sum_{k=1}^{N} s(t - kt_d) e^{jk\Delta wt} \tag{4.22}$$

where $\Delta w = \dfrac{\beta T_p}{N}$. Figure 4-4 shows the model for the envelope of the chirp signal which is mathematically expressed in equation (4.22).
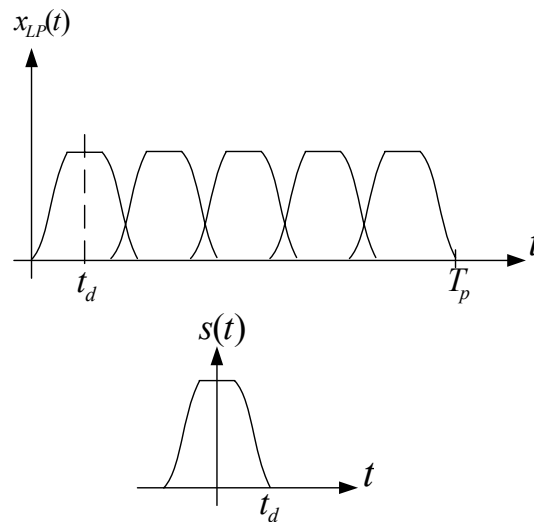
Figure 4-4: The Mathematical Modeling of the Chirp Signal

After approximating the envelope of the incident pulse by following this procedure, the transient response of a scatterer can be obtained by employing MFDS. In fact, there are two ways for the application of MFDS after this point which are computationally almost equivalent to each other.

The first method handles each short pulse $s(t - kt_d)$ separately and then combines the solutions for these short pulses by taking into account of the time delay between the pulses. During these operations an M_k point FFT and IFFT are done for N times. (M_k's are determined by considering the Nyquist rate of each short pulse) Since the short pulse has a constant frequency, the beam width of the short pulse is narrower than the whole incident pulse. Therefore, in each iteration, the frequency domain solutions are computed for a less number of frequency components.

On the other hand in the second method, the envelope of the incident pulse is treated in only one iteration. In this case, the Nyquist rate is chosen as the greatest Nyquist rate of the short pulses. Therefore an $N \max\{M_k\}$ point FFT and IFFT are performed and the corresponding frequency domain problem is solved for only once.

In this study, the second approach was preferred because of its slight advantages against the first method.

4.3 Numerical Results

In this part of the thesis, the waveform analysis of the scattered fields was accomplished on very simple targets like plates and corner reflectors and the scattered waveforms were discussed in terms of high frequency scattering mechanisms. For this purpose, two different incident waveforms were used to illuminate the objects. The first one was a short pulse of width 5ns and the second one was a frequency modulated chirp signal with a pulse width of 1μs.

In the first time domain experiment a $100\lambda \times 5\lambda$ PEC plate was used with the same geometry given in the frequency domain experiments. Figure 4-5 the experiment geometry is illustrated in which the longer dimension of the plate is in

the *x* direction. This plate was illuminated by an incident wave with a carrier frequency of 10 GHz. The envelope of the incident pulse and its Fourier transform are also shown in Figure 4-6.
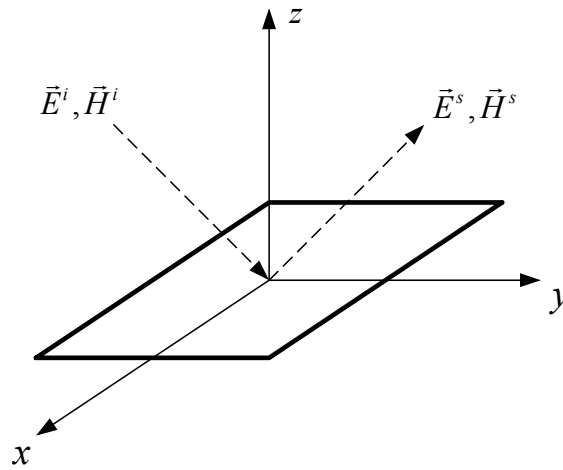

**Figure 4-5: Simulation Geometry for PEC Plate**
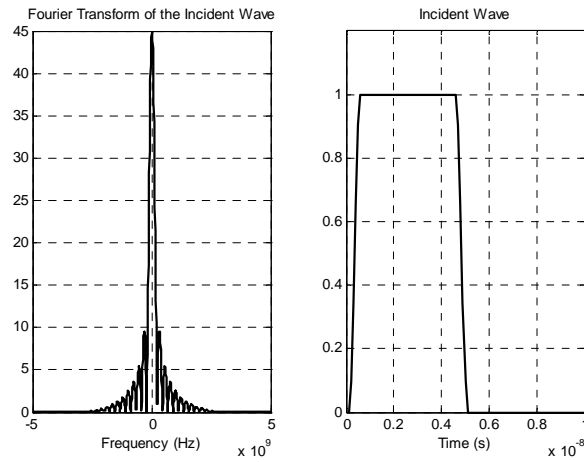
Figure 4-6: Envelope of the Incident Waveform

This plate was normally illuminated from the normal direction ($\theta_i = 0°$) and the backscattered waveform at a distance of *500m* from the plate was observed. In

Figure 4-7 the envelope scattered waveform and its Fourier transform obtained by PO are shown. As it can be seen from this figure, the amplitude of the scattered wave is smaller than the incident wave as expected. On the other the waveforms of these pulses are identical. Indeed, this observation is an obvious consequence of the high frequency scattering mechanisms. Since the specular reflection and backscattering directions coincide for normal incidence, specular reflection mechanism dominates the scattered wave. Hence, its waveform does not change in comparison with the incident pulse.
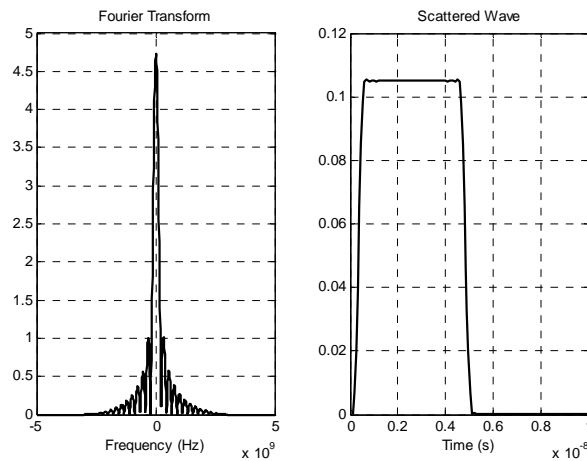
Figure 4-7: Envelope of the Scattered Waveform Computed by PO (Normal Incidence)

Then the angle of incidence was changed to $\theta_i = 30°$ and the plate was illuminated from the plane $\phi_i = 0°$. In this case, the waveform of the scattered signal differs from the incident signal. There exist two pulses as it can be seen from Figure 4-8. Again by taking the scattering mechanisms into account, a logical statement can be made. Since for oblique incidence the specular reflection and backscattering directions are different, in the backscattering direction "end region scattering" mechanism becomes dominant. Therefore, the scattered fields from the two edges of the plate are seen as two distinct pulses.

In addition to the explanations stated above, one may also observe that the amplitudes of the pulses are very small when compared with amplitude of the scattered wave obtained for normal incidence. In Section 2.4.1 it was stated that the end region scattering contributes to the side lobes of the scattering pattern. However, main lobe is generated by specular reflection. Thus, it is very usual to expect a weaker scattering for oblique incidence than for normal incidence. It does also worth to mention that, the duration of the pulses are same with the incident pulse due to the fact that the whole phase front hits to edge at the same time.
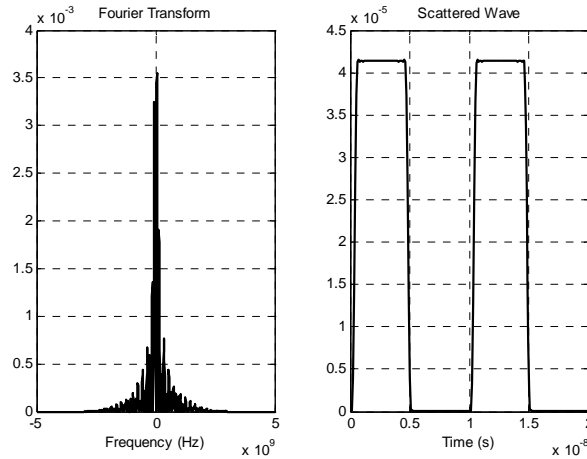
Figure 4-8: Envelope of the Scattered Waveform Computed by PO ($\theta_i = 30°$ and $\phi_i = 0°$)

The time retardation between the pulses scattered from the edges of the plate can be calculated by making the use of the effective length illustrated in Figure 4-9. The effective length between the two edges of the plate, which is given in the equation (4.23), is equal to the projected length of the plate in the direction of incidence.

$$w_{eff} = w\sin\theta_i \qquad\qquad (4.23)$$

After the incident pulse is scattered from the leading edge of the plate, it travels along the plate and is scattered from the trailing edge. Since the pulse scattered from trailing edge travels along the plate twice (before and after scattering), the retardation or delay time between these pulses can be obtained by using equation (4.24) in which the speed of light is denoted by c.

$$t_{ret} = \frac{2w_{eff}}{c} = \frac{2w\sin\theta_i}{c} \qquad (4.24)$$

In our case, the length of the plate along the x direction is equal to 100λ and the plate is illuminated from $\theta_i = 30°$. Therefore, the effective length is found to be 50λ. Since the wavelength at 10 GHz is equal to 0.03m, the retardation time is calculated as 10ns which agrees with the results illustrated in Figure 4-8.
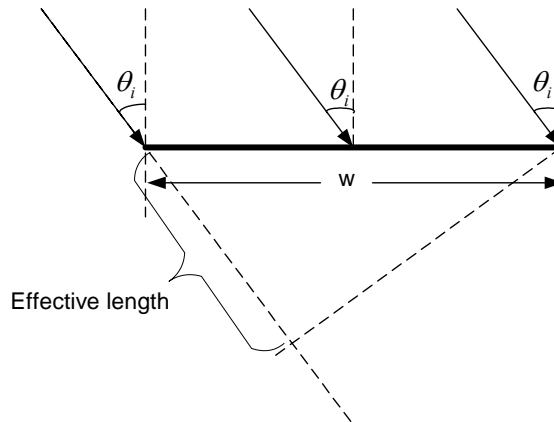
Figure 4-9: Illustration of the Effective Length

If the incidence angle is increased to $\theta_i = 60°$, due to the increase in the effective length of the plate, the retardation time between the pulses scattered from the edges increases. In fact, the results shown in Figure 4-10 agree with this inference. If we further increase the incidence angle to $\theta_i = 90°$, the retardation

time is expected to have its maximum value. Figure 4-11 illustrates the results related to this case. It is also essential to note that the amplitude of the scattered wave is inversely proportional with the incidence angle as it can be observed from the figures.
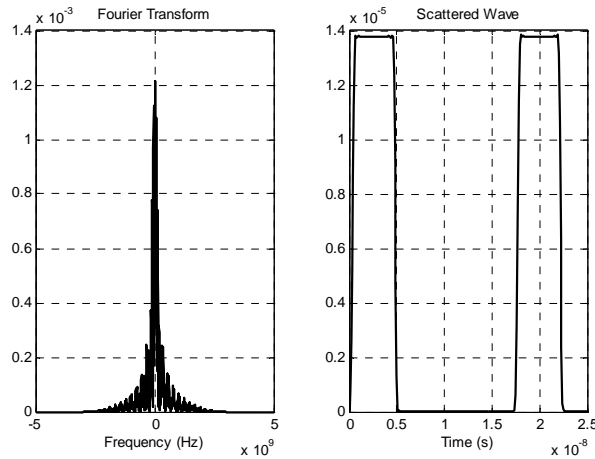
Figure 4-10: Envelope of the Scattered Waveform Computed by PO ($\theta_i = 60°$ **and** $\phi_i = 0°$)
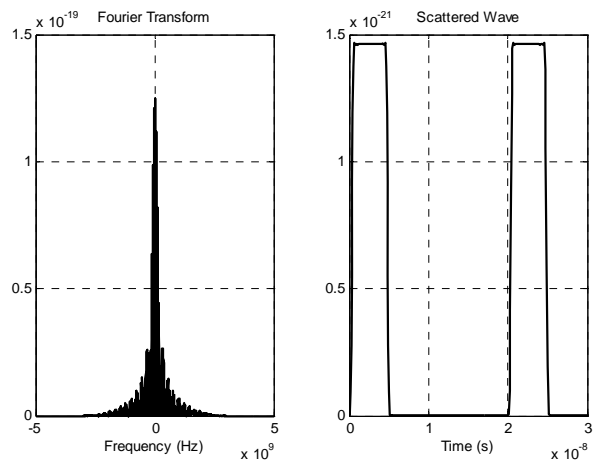

Figure 4-11: Envelope of the Scattered Waveform Computed by PO ($\theta_i = 90°$ **and** $\phi_i = 0°$)

If we change the incidence direction from $\phi_i = 0°$ to $\phi_i = 90°$, the effective length of the plate decreases below to a critical value such that the pulses cannot be distinguished from each other. The two pulses overlap and form a new waveform with a different envelope and duration. This situation is similar to the range resolution concern in RADAR systems. Figure 4-12 shows the waveform obtained for this case.
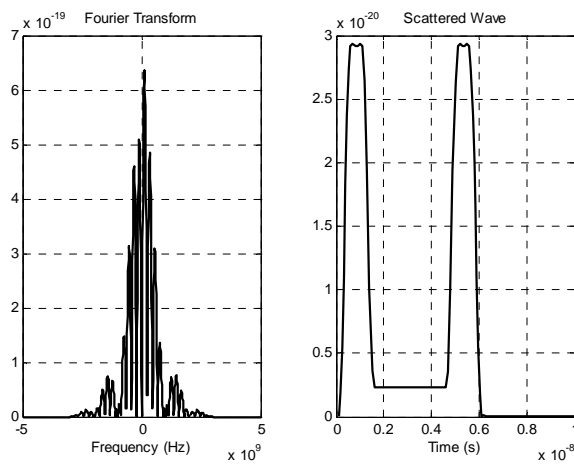
Figure 4-12: Envelope of the Scattered Waveform Computed by PO
($\theta_i = 90°$ **and** $\phi_i = 90°$)

Figure 4-13 illustrates the envelope of the scattered wave and its Fourier transform for the case $\theta_i = 30°$ and $\phi_i = 45°$. Since the plate is illuminated from $\phi_i = 45°$, the whole phase front of the incident pulse does not hit to the edge of the plate at the same time for this case. The pulse firstly hits to the corner at one point, the rest of the phase front gradually hits to the plate as the pulse penetrates along it. Therefore, for this incidence direction, the transient effects may be seen more clearly. In fact, the duration of the pulses shown in Figure 4-13 is greater than 5ns.

74

Throughout the experiments conducted by employing PO, the effects of the specular reflection and end region scattering mechanisms on the scattered waveform were observed properly. In addition to these scattering mechanisms, in order to see the effects of diffraction, modified PO was employed for the same problem given above. The results obtained in this case slightly differed from the results obtained by PO. All of the discrepancies observed in these experiments were explained via diffraction phenomena.
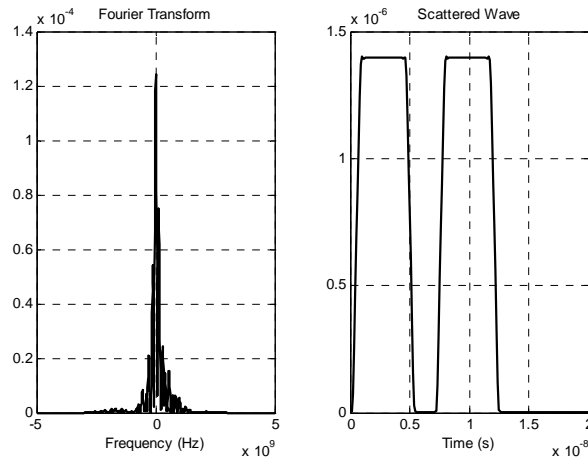

Figure 4-13: Envelope of the Scattered Waveform Computed by PO
($\theta_i = 30°$ **and** $\phi_i = 45°$)

In the first experiment conducted by modified PO, the plate was illuminated normally. Since specular reflection is dominant in the backscattering direction for normal incidence the results obtained in this experiment were the same with the results obtained by PO. Figure 4-14 and Figure 4-15 show the results of this experiment for different polarizations.
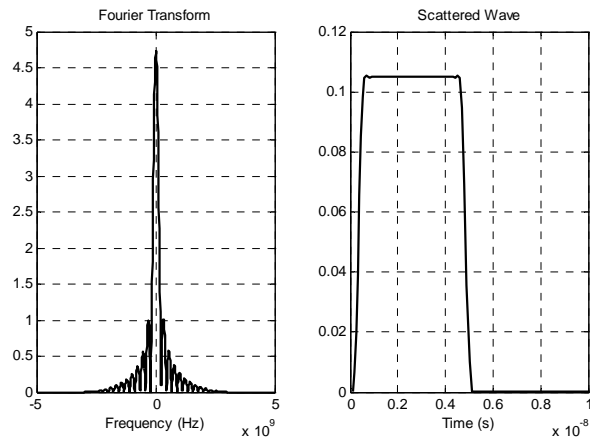
Figure 4-14: Envelope of the Scattered Waveform Computed by Modified PO
(Normal Incidence $\phi\phi$ Polarization)
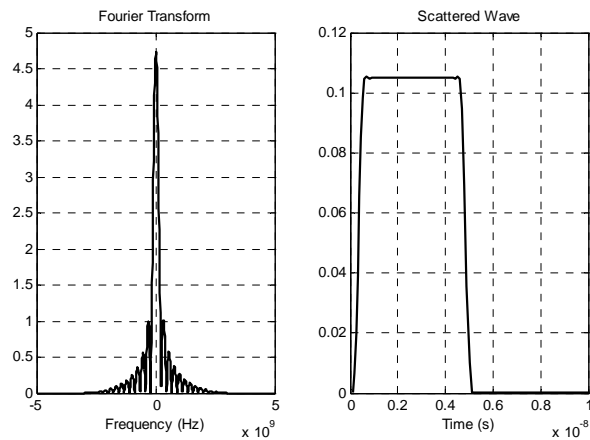
Figure 4-15: Envelope of the Scattered Waveform Computed by Modified PO
(Normal Incidence $\theta\theta$ Polarization)

Then the angle of incidence was increased from $\theta_i = 0°$ to $\theta_i = 30°$ and it was observed that the responses of the edges were different for different polarizations. The scattered waveforms obtained in this experiment are illustrated in Figure 4-16 and Figure 4-17.
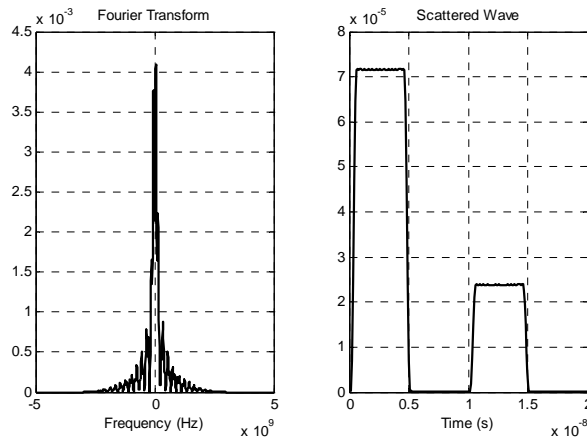
Figure 4-16: Envelope of the Scattered Waveform Computed by Modified PO
($\theta_i = 30°$ **and** $\phi_i = 0°$ $\phi\phi$ **Polarization**)
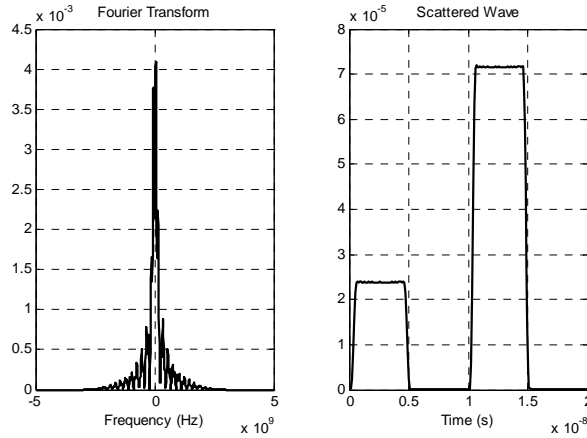
Figure 4-17: Envelope of the Scattered Waveform Computed by Modified PO
($\theta_i = 30°$ **and** $\phi_i = 0°$ $\theta\theta$ **Polarization**)

These results can be explained mathematically by using the consequences of the two dimensional scattering problem from a strip solved in Section 2.4.3. In the GTD solution of that problem, the contributions from the edges of the plate are given by the equations (2.71) and (2.72) for a soft polarized incident wave. (In our case $\phi\phi$ polarization corresponds to soft polarization.) From these equations, the ratio of the magnitudes of the fields scattered from the edges may be attained as

$$\frac{\left|\overline{E}_2^d\right|}{\left|\overline{E}_1^d\right|} = \frac{\left|1 - \dfrac{1}{\cos\varphi}\right|}{\left|1 + \dfrac{1}{\cos\varphi}\right|} \tag{4.25}$$

where the angle between the incident wave and the plane on which the plate lies is denoted by φ. Since in the geometry of the problem the leading edge is numbered as the 2nd edge, the contributions from the leading and trailing edges of the plate are also denoted by $\overline{E}_2^d$ and $\overline{E}_1^d$ respectively.

When the incidence angle is equal to $\theta_i = 30°$, then the angle from the plane of the plate will be equal to $\varphi = 120°$. Hence the ratio of the magnitudes of the fields scattered from the leading and trailing edges is calculated to be equal to 3 from equation (4.25). If this result is compared with the ratio of the amplitudes of pulses read from Figure 4-16, the consistency of the results can be seen effortlessly. From the figure, this ratio is attained to be equal to $\frac{\left|\overline{E}_2^d\right|}{\left|\overline{E}_1^d\right|} = \frac{7.16 \times 10^{-5}}{2.39 \times 10^{-5}} = 2.996$.

For the hard polarization ($\theta\theta$ Polarization) case, due to the change in the diffraction coefficients, the roles of the leading and trailing edges toggle. As it can be seen from the equations (2.75) and (2.76), the contribution of the trailing edge becomes more dominant.

A further discussion about the physics of this problem is done in [54]. It is stated that for soft polarization, the dominant current mode generated on the surface of the plate is due to diffraction from the leading edge; the trailing edge has a low level contribution. On the other hand, for hard polarization trailing edge becomes dominant and surface travelling waves are generated in addition to diffracted

78

field. In view of the fact that our approach cannot model the surface travelling waves, their contribution to the total scattered field are not observed.

Similar results are obtained for other incidence directions which are illustrated from Figure 4-18 to Figure 4-23. Here it is interesting to note that when the incidence angle becomes $\theta_i = 90^\circ$, the contributions of the trailing edge and leading edge vanish for soft and hard polarizations, respectively.
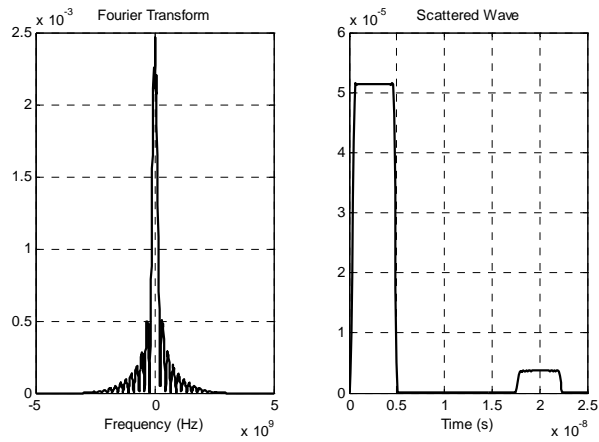
Figure 4-18: Envelope of the Scattered Waveform Computed by Modified PO
($\theta_i = 60°$ **and** $\phi_i = 0°$ $\phi\phi$ **Polarization**)
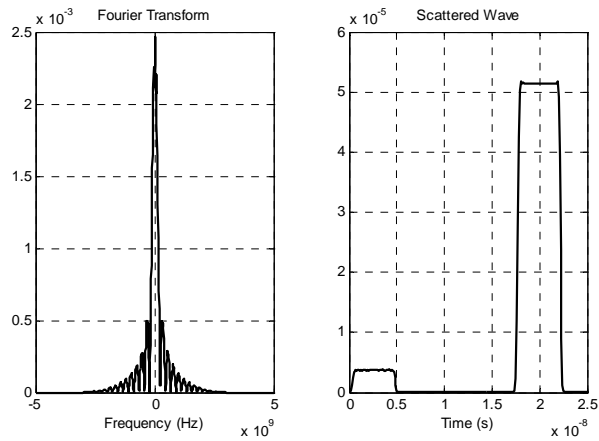
Figure 4-19: Envelope of the Scattered Waveform Computed by Modified PO
($\theta_i = 60°$ **and** $\phi_i = 0°$ $\theta\theta$ **Polarization**)
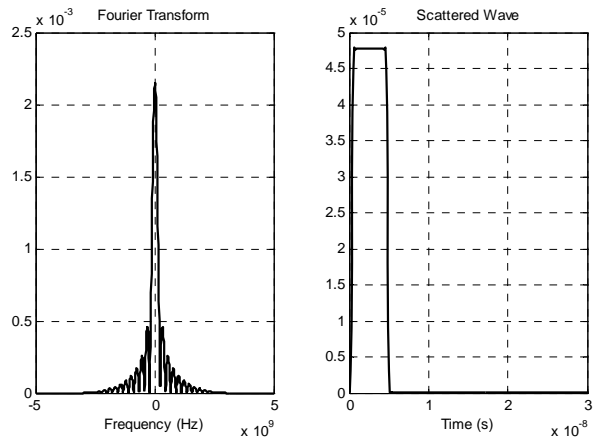
Figure 4-20: Envelope of the Scattered Waveform Computed by Modified PO
($\theta_i = 90°$ **and** $\phi_i = 0°$ $\phi\phi$ **Polarization**)
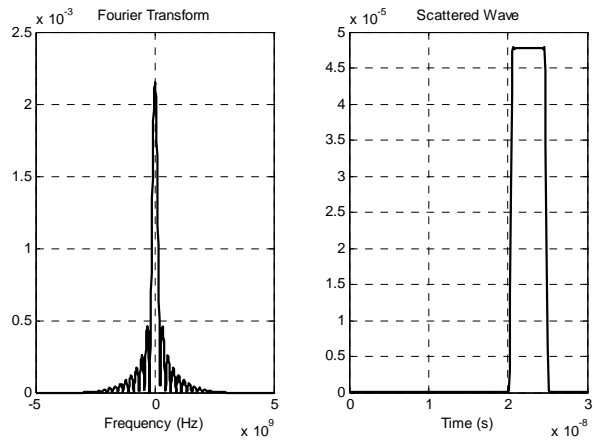
Figure 4-21: Envelope of the Scattered Waveform Computed by Modified PO
($\theta_i = 90°$ **and** $\phi_i = 0°$ $\theta\theta$ **Polarization**)
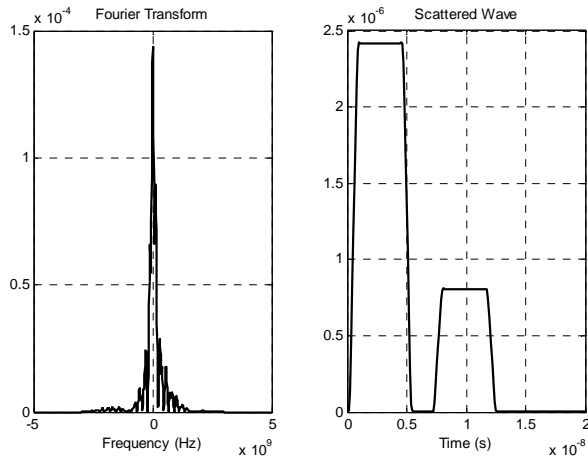
Figure 4-22: Envelope of the Scattered Waveform Computed by Modified PO
($\theta_i = 30°$ **and** $\phi_i = 45°$ $\phi\phi$ **Polarization**)
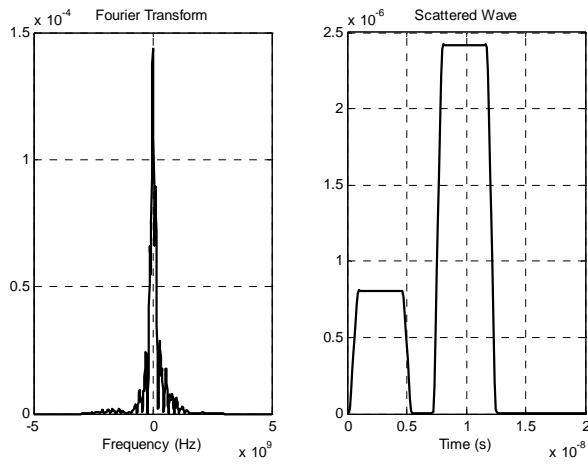
Figure 4-23: Envelope of the Scattered Waveform Computed by Modified PO
($\theta_i = 30°$ **and** $\phi_i = 45°$ $\theta\theta$ **Polarization**)

The effects of different scattering mechanisms can be observed easily under illumination by a short pulse. However, the pulse width of the short pulse used in the previous experiments is very small when compared with the usual RADAR pulses. Therefore, in order to see the validity of the Fourier domain approach for feasible RADAR pulses, the same experiments were repeated with a longer pulse.

According to Skolnik, for a pulse Doppler RADAR operating in the X-band (8-12 GHz) and with a medium pulse repetition frequency, the most common pulse repetition frequencies are between 10-30 kHz with a duty cycle around 0.05 [55]. Thus, a long pulse with a pulse width of 1μs is an appropriate choice for the experiments. Moreover, this long pulse is chosen to be a frequency modulated chirp signal with a chirp rate of 100 MHz which is also a feasible value for RADAR systems. Figure 4-24 shows the envelope of the incident pulse and its Fourier transform, which is modeled by a combination of 5 shorter pulses with constant frequencies according to the procedure stated in the previous section.
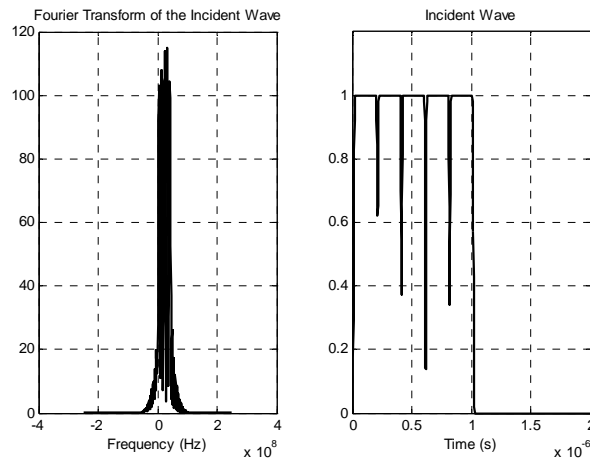

Figure 4-24: Envelope of the Incident Long Pulse and its Fourier Transform

The experimental results obtained for the long pulse are shown from Figure 4-25 to Figure 4-34. Since the pulse width of the incident signal is greater than the time

interval necessary to travel a distance equal to two times the length of the plate, the effects of end region scattering and diffraction mechanisms cannot be noticed.
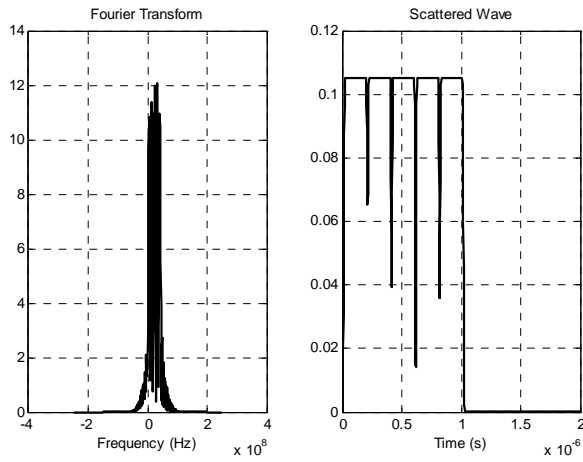

Figure 4-25: Envelope of the Scattered Waveform Computed by Modified PO (Normal Incidence $\phi\phi$ Polarization)
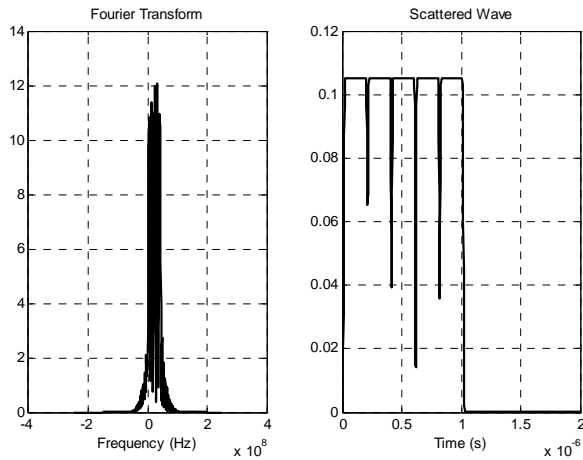

Figure 4-26: Envelope of the Scattered Waveform Computed by Modified PO (Normal Incidence $\theta\theta$ Polarization)
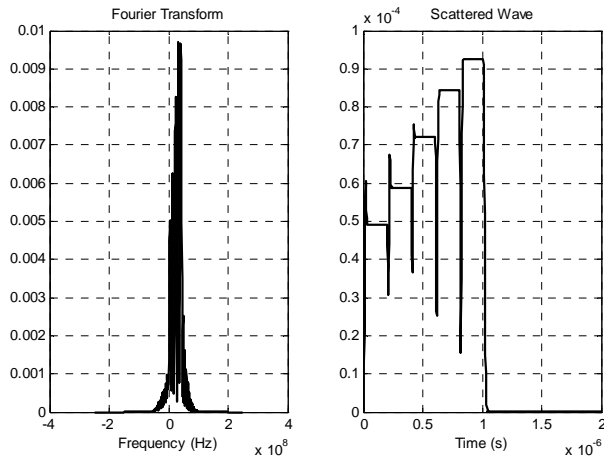
Figure 4-27: Envelope of the Scattered Waveform Computed by Modified PO
($\theta_i = 30°$ **and** $\phi_i = 0°$ $\phi\phi$ **Polarization**)
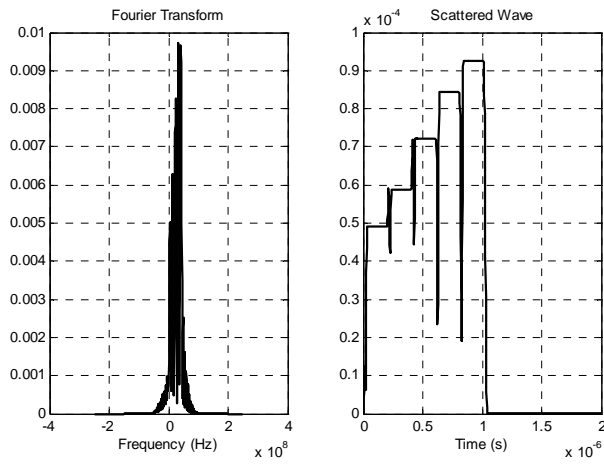
Figure 4-28: Envelope of the Scattered Waveform Computed by Modified PO
($\theta_i = 30°$ **and** $\phi_i = 0°$ $\theta\theta$ **Polarization**)
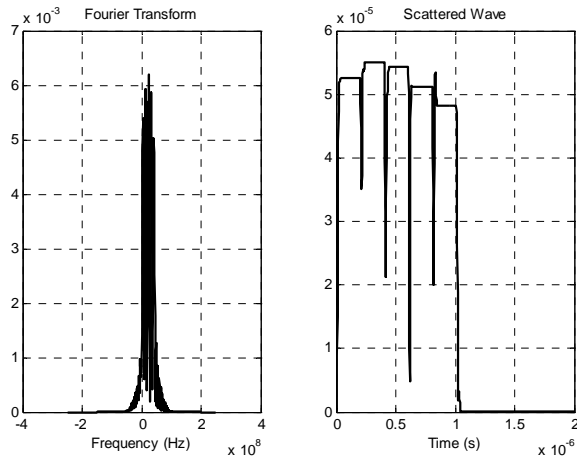
Figure 4-29: Envelope of the Scattered Waveform Computed by Modified PO
($\theta_i = 60°$ **and** $\phi_i = 0°$ $\phi\phi$ **Polarization)**
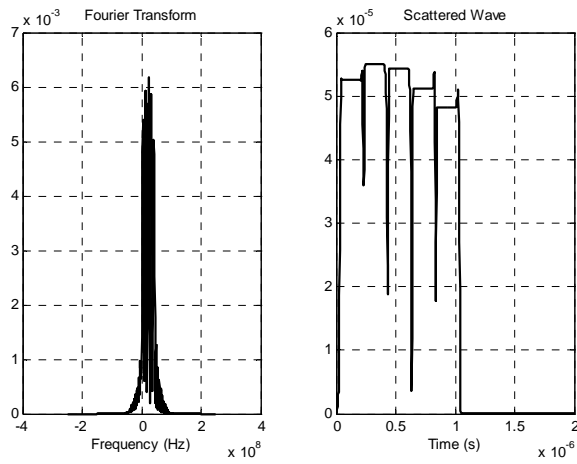
Figure 4-30: Envelope of the Scattered Waveform Computed by Modified PO
($\theta_i = 60°$ **and** $\phi_i = 0°$ $\theta\theta$ **Polarization)**
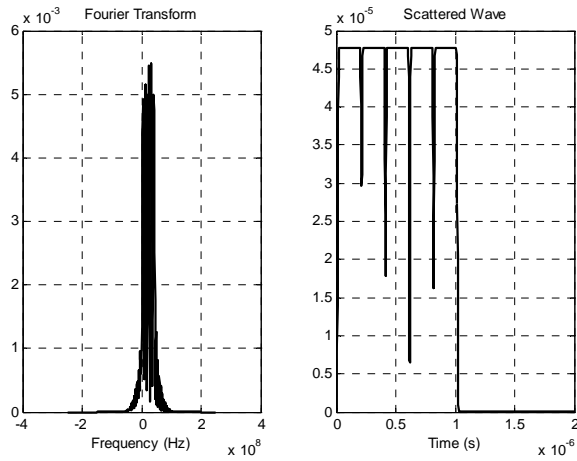
Figure 4-31: Envelope of the Scattered Waveform Computed by Modified PO
($\theta_i = 90°$ **and** $\phi_i = 0°$ $\phi\phi$ **Polarization**)
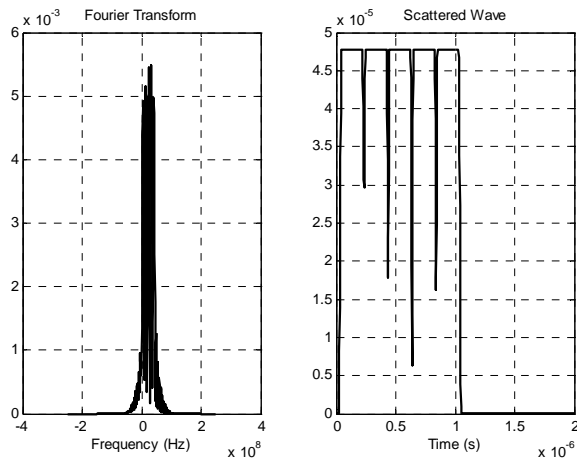
Figure 4-32: Envelope of the Scattered Waveform Computed by Modified PO
($\theta_i = 90°$ **and** $\phi_i = 0°$ $\theta\theta$ **Polarization**)

87
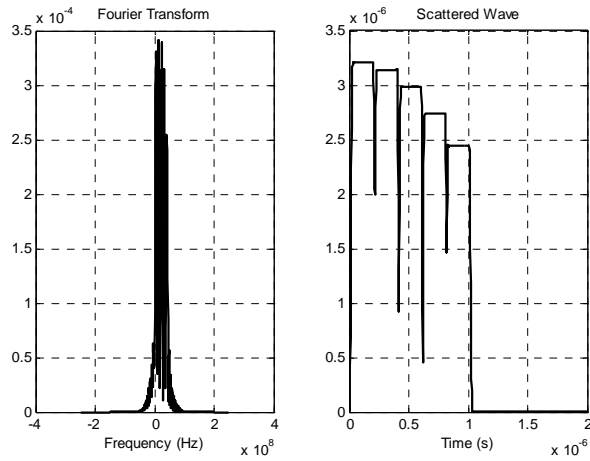
Figure 4-33: Envelope of the Scattered Waveform Computed by Modified PO
($\theta_i = 30°$ **and** $\phi_i = 45°$ $\phi\phi$ **Polarization**)
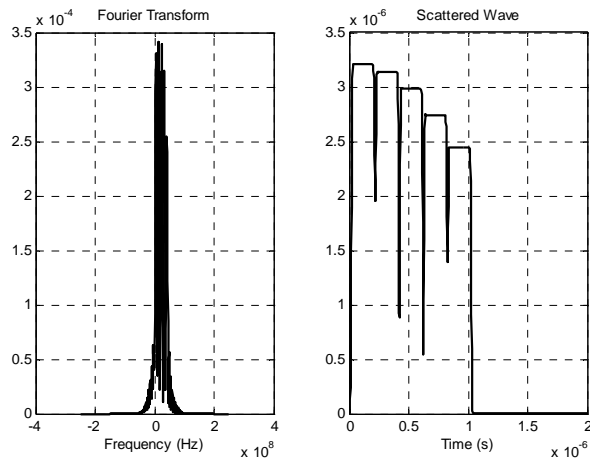
Figure 4-34: Envelope of the Scattered Waveform Computed by Modified PO
($\theta_i = 30°$ **and** $\phi_i = 45°$ $\theta\theta$ **Polarization**)

For the case where $\theta_i = 90°$ the scattered wave attained for hard polarization is slightly retarded in comparison with the scattered wave attained for soft polarization. This is because of the fact that the incident wave does not recognize the leading edge for hard polarization and the entire scattered field is generated by the trailing edge as explained in the discussions made for short pulse examples. Since in this case the pulse width is very large, the duration for the field to travel the way between the two edges is negligible. Hence, the retardation cannot be observed clearly.

It is also interesting to note that for oblique incidence cases, the strength of the pulse is not constant because, the frequency response of the plate is different for different frequencies and this difference becomes significant for oblique incidence where specular reflection mechanism loses its effect in the backscattering direction.

The last experiment conducted for time domain waveform analysis was performed on a corner reflector shown in Figure 4-35 to see the effect of specular reflection mechanism in scattering problems. The corner reflector used in the experiment is composed of two plates which have the same dimensions with the plate used in the previous experiments. One of these plates is located on *z=0* plane and the other is attached to it with an obtuse angle. Thus, when the corner reflector is illuminated normally, specular reflection takes place in the first plate while end region scattering and diffraction occurs in the other plate for backscattering direction. Since the total scattered field is the combination of the fields scattered from the plates, we may examine the effects of these scattering mechanisms by comparing with the results attained in plate experiments.
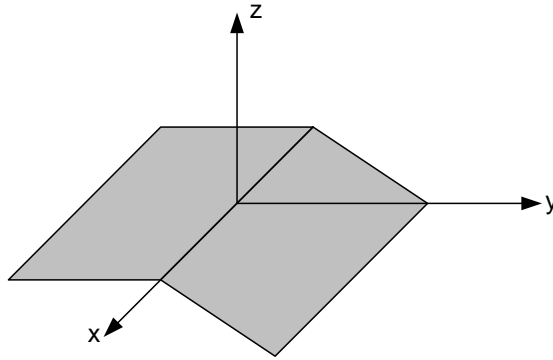
Figure 4-35: Corner Reflector

Figure 4-36 and Figure 4-37 illustrates the envelope of the scattered wave from the corner reflector when it is illuminated by short and long pulses respectively. For both case, the amplitudes of the scattered waves are almost equal to the amplitude of the wave scattered from the plate under normal incidence. Furthermore, since the projected distance between the edges of the second plate in y direction is very small, the pulse scattered from the trailing edge of the second plate overlaps the pulse scattered from the leading edge and cannot be observed. Hence, we may conclude that, if there exist a specular reflection contribution in the observation direction, it dominates the scattered field.
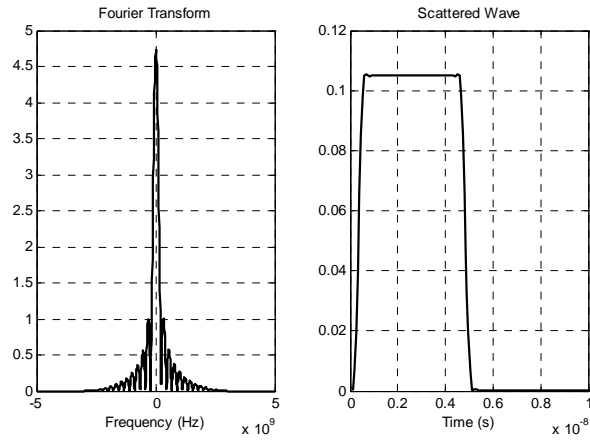
Figure 4-36: Envelope of the Scattered Waveform from Corner Reflector Computed by Modified PO (Normal Incidence $\phi\phi$ Polarization) For Short Pulse
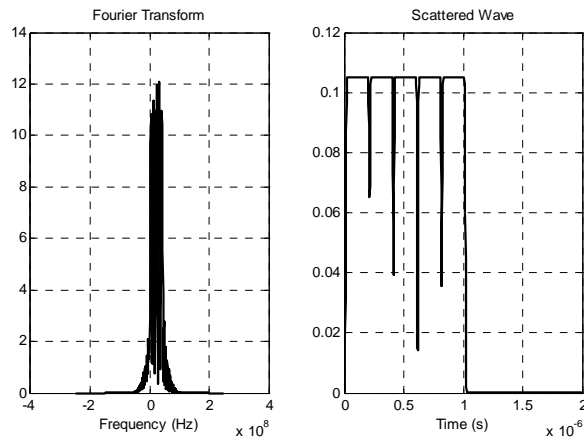

Figure 4-37: Envelope of the Scattered Waveform from Corner Reflector Computed by Modified PO (Normal Incidence $\theta\theta$ Polarization) For Long Pulse

CHAPTER 5

NUMERICAL RESULTS AND DISCUSSIONS

5.1 Frequency Domain Experiments

The RCS results of very primitive targets like plates, curved screens and dihedral corner reflectors were given in the previous chapters but the performance of the developed approach was not tested for other objects. Therefore, RCS results related to additional targets will be presented in this section. In the first part, the experimental results obtained for simple shapes by Levin's method will be compared by POFACETS 3.01 results. Then, the RCS of a tank whose surface mesh model is illustrated in Figure 3-1 will be given for different aspect angles and polarizations. Finally, a statistical analysis of the scattered fields from the tank model will be conducted in the last part.

5.1.1 Simple Targets

In this part, the RCS results of a cube, a rectangular prism, a cylinder and a sphere were computed by Levin's method by employing both PO and Modified PO methods. It was observed that the results were in good agreement with the results of POFACETS 3.01 code which uses Ludwig's integration algorithm. Furthermore, Levin's method was seen to have significant advantages in terms of computational aspects. For the sake of being consistent with the previous chapters, the experiments were performed at 10 GHz.

The first experiment was performed on a cube which is shown in Figure 5-1. The monostatic RCS of the cube was computed with respect to θ in the planes $\phi = 45°$ and $\phi = 90°$. The results are illustrated in Figure 5-2 and Figure 5-3.
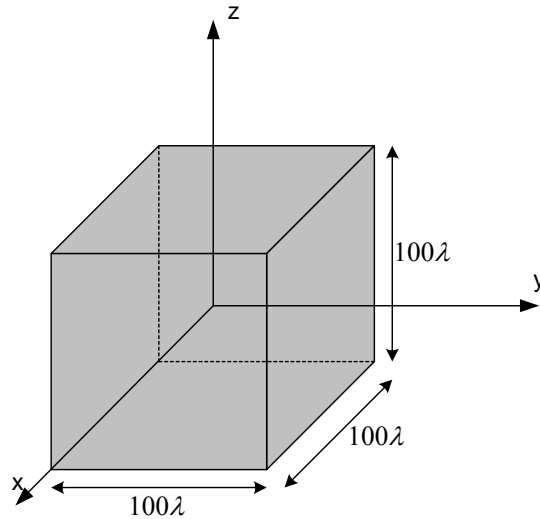

Figure 5-1: Cube Model

In this experiment, the cube was modeled by 6 square facets for Levin's approach. On the other hand POFACETS 3.01 uses 12 triangular facets for the same model. It can be observe from the figures that PO results attained by Levin's method are in good agreement with POFACETS 3.01 results. Therefore, if we take the number of facets (i.e. number of computation) into account, Levin's method seems to be more efficient. Furthermore, for the directions where the specular reflection region coincides with the backscattering region, the Modified PO results are close to results of other two. However, for the angles where diffraction becomes significant, Modified PO gives enhanced RCS values.
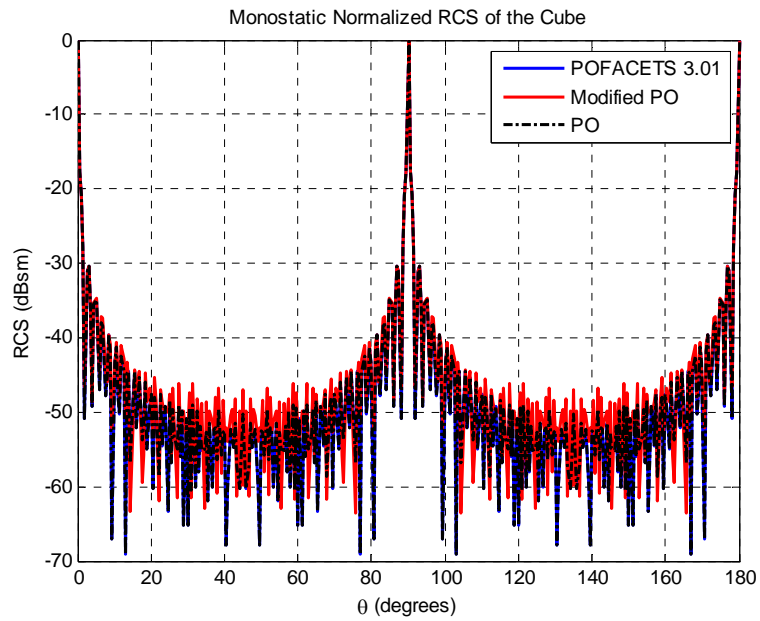
**Figure 5-2: Monostatic Normalized RCS of the Cube ($\phi = 90^\circ$)**
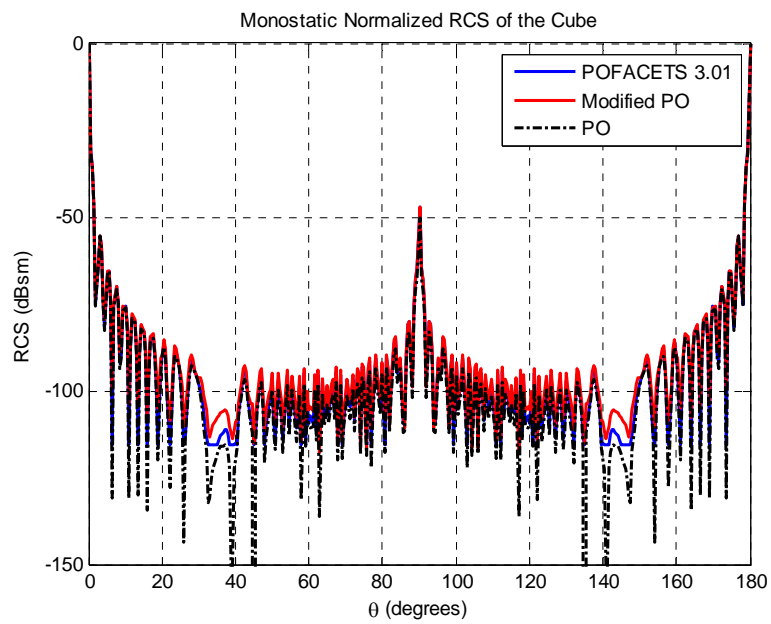
Figure 5-3: Monostatic Normalized RCS of the Cube ($\phi = 45^\circ$)

Figure 5-4 shows the model of rectangular prism used in the second experiment. Similar to the first experiment, the monostatic RCS of the model was computed on the planes $\phi = 45°$ and $\phi = 90°$ which are illustrated in Figure 5-5 and Figure 5-6. From these figures one may conclude the same results discussed in the previous experiment. Moreover, as in the first experiment, the prism was modeled by 6 facets for Levin's method while 12 triangular facets were used for Ludwig's method.
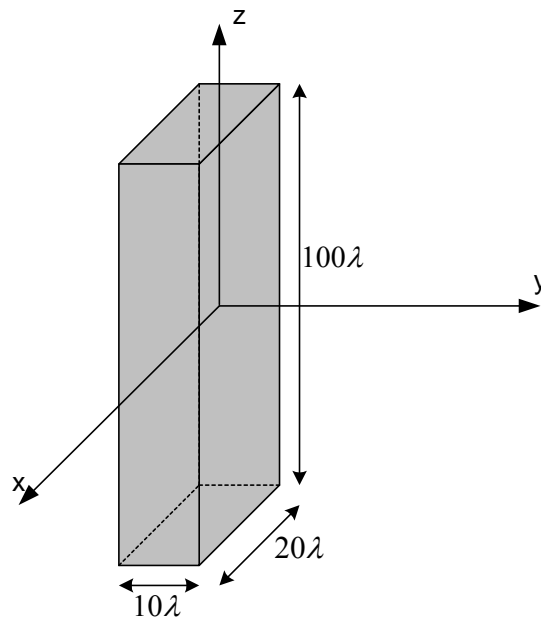

Figure 5-4: Rectangular Prism Model
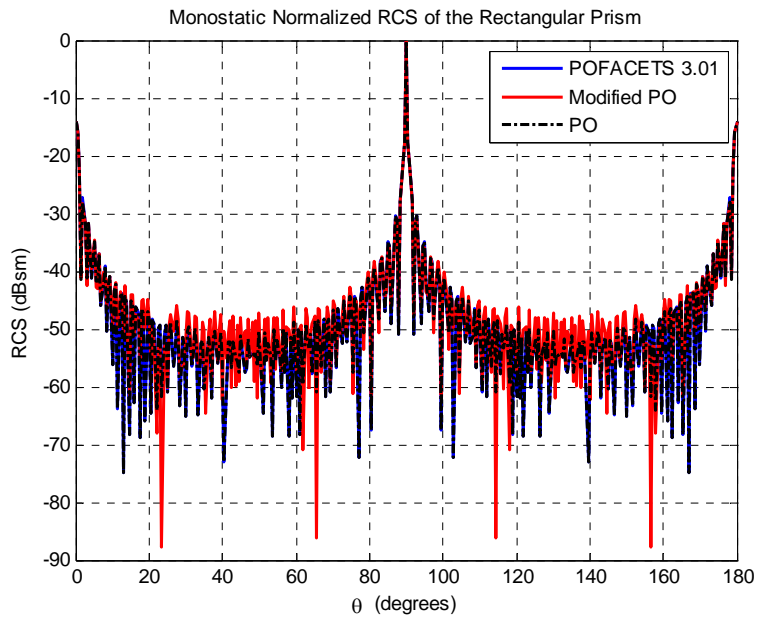
**Figure 5-5: Monostatic Normalized RCS of the Rectangular Prism ($\phi = 90°$)**
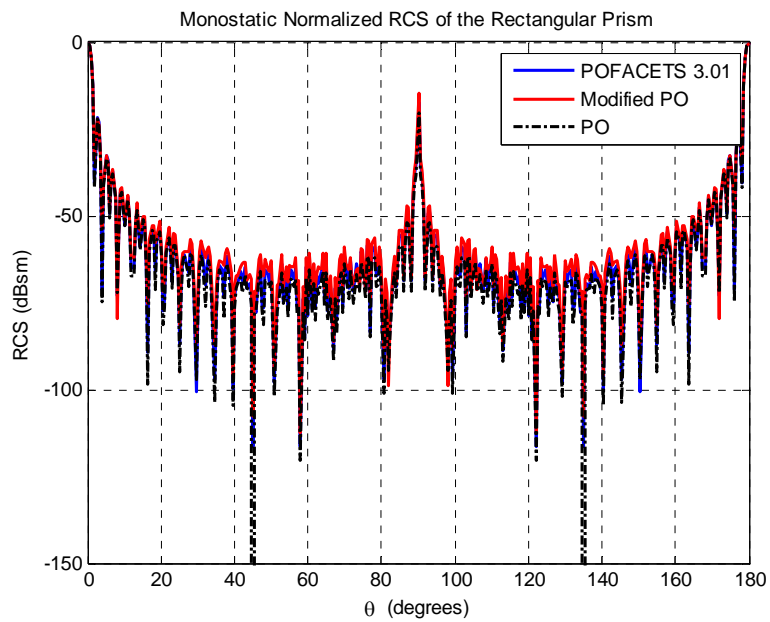
Figure 5-6: Monostatic Normalized RCS of the Rectangular Prism ($\phi = 45°$)

The next model used in these experiments, which is shown in Figure 5-7, was a circular cylinder. Since cylinder is symmetric with respect to ϕ the monostatic RCS of the cylinder was computed for only one angle. The results of this experiment are illustrated in Figure 5-8.
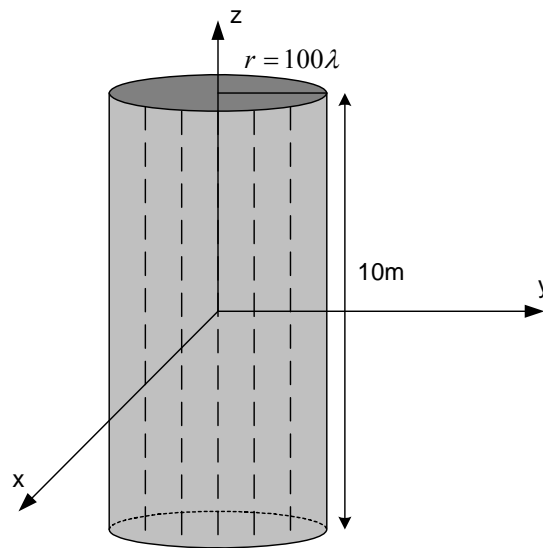

Figure 5-7: Cylinder Model

Apart from the previous ones, this experiment has an important place in terms of demonstrating the computational efficiency of the Levin's method in comparison with the Ludwig's method. Even though the curved surface of the cylinder is modeled by 600 triangular facets in POFACETS 3.01, only 90 curved patches were used in Levin's method. Hence, the number of computation was decreased approximately on the order of 1/6 in comparison with Ludwig's method.

Another important consequence of this experiment comes from the results of Modified PO. Since the upper and lower sides of the cylinder were not modeled in this experiment (It can be considered as a pipe.), the PO approaches give nearly zero field for incidence angles of $\theta = 0°$ and $\theta = 180°$ for both Levin's and

97

Ludwig's methods. However, Modified PO approach results in a considerable amount of scattered field in the neighborhood of these regions due to the fact that it accounts for the diffraction effects. On the other hand around $\theta = 90°$, PO, Modified PO and POFACETS 3.01 give almost the same results.
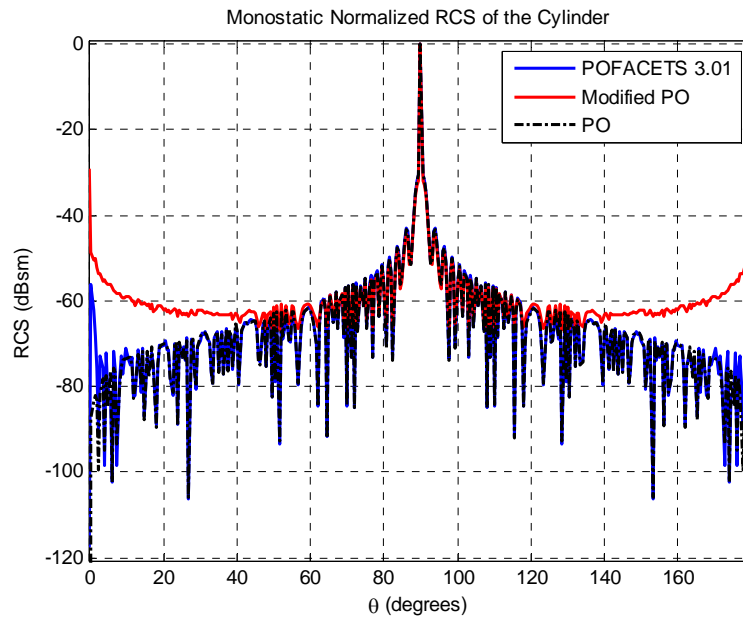
Figure 5-8: Monostatic Normalized RCS of the Cylinder

The last simple target was a sphere with a radius of 1m. The monostatic RCS of this sphere was computed by Levin's method and its variation with respect to frequency was tried to be observed. Figure 5-9 shows the results of this experiment where the sphere was modeled by 7204 curved and 16204 flat patches separately. It can be observed that both models give close results that converge to πr^2 as frequency increases. Nevertheless, the results belonging to flat patch model start to deviate from the correct results for high frequencies. This outcome also proves the computational efficiency of Levin's method in terms of its applicability to curved surfaces.
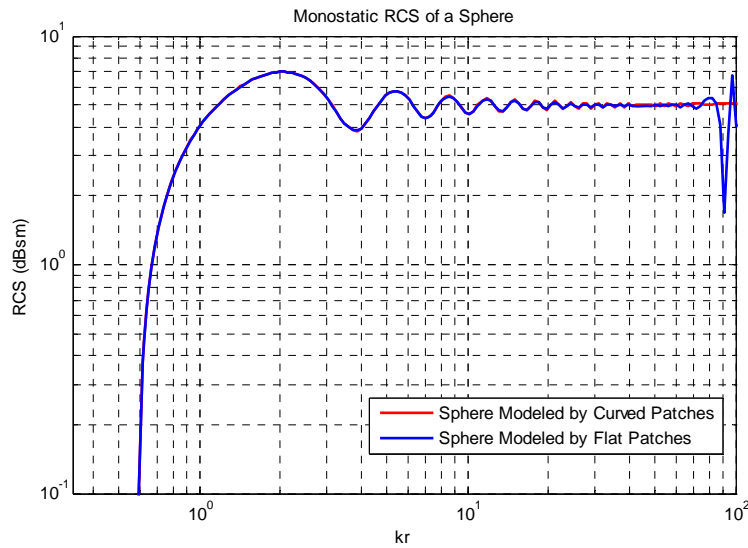
**Figure 5-9: Monostatic RCS of the Sphere with Respect to Frequency**

5.1.2 Complex Targets

After the experiments conducted on simple objects, to see the performance of Levin's method on complex targets, more realistic models were simulated. For this purpose, the RCS of a tank model illustrated in Figure 3-1 was computed for different polarizations and aspect angles. Three aspect angles were used through out the experiments, which were $\theta = 85°$, $\theta = 80°$ and $\theta = 75°$ corresponding to elevation angles of $5°$, $10°$ and $15°$ respectively. In fact, these angle values are very feasible in terms of military concerns. The RCS of the tank was computed with respect to ϕ and the results for both co-polarization and cross-polarization cases were observed. First, the RCS computations were performed by PO approach. Then, the same experiments were repeated by Modified PO in order to see the contribution of the diffracted fields to the results. Figure 5-10 - Figure 5-12 and Figure 5-13 - Figure 5-15 illustrates the co-polarized monostatic RCS of the tank model.
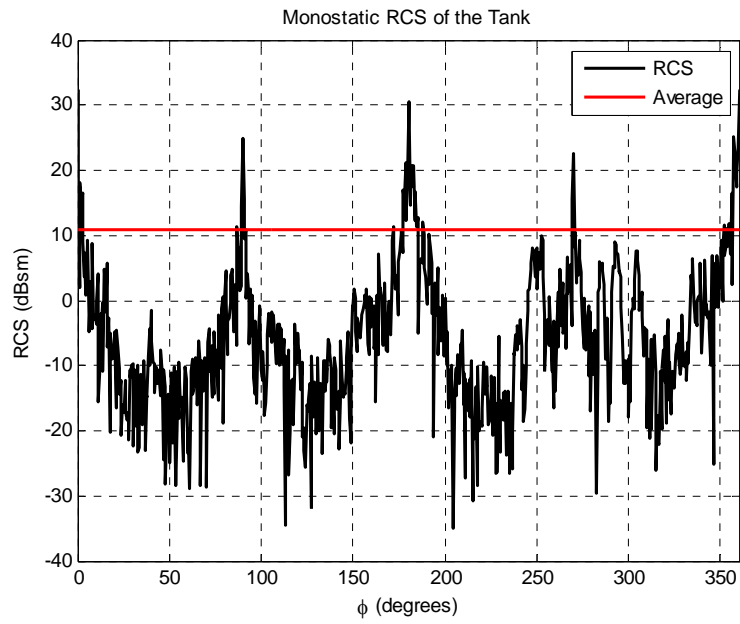
Figure 5-10: Monostatic RCS of the Tank Computed by PO ($\theta = 85°$)
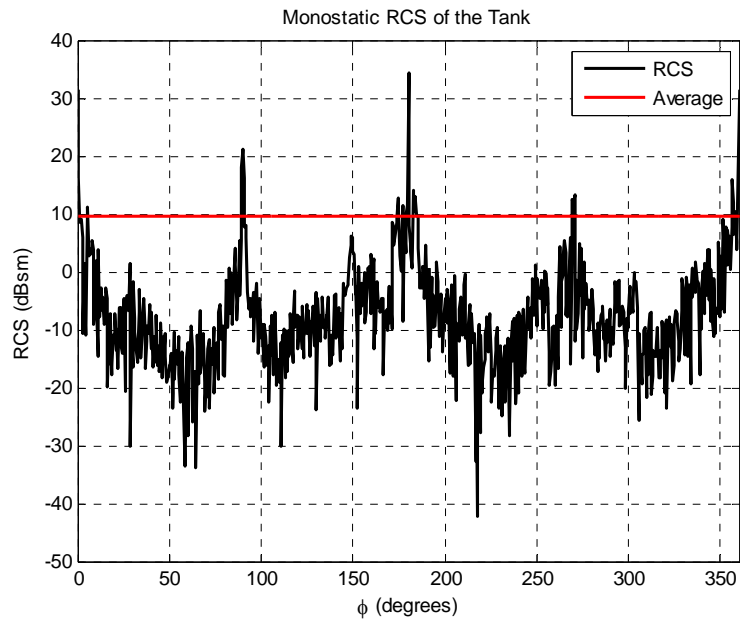
Figure 5-11: Monostatic RCS of the Tank Computed by PO ($\theta = 80°$)

100
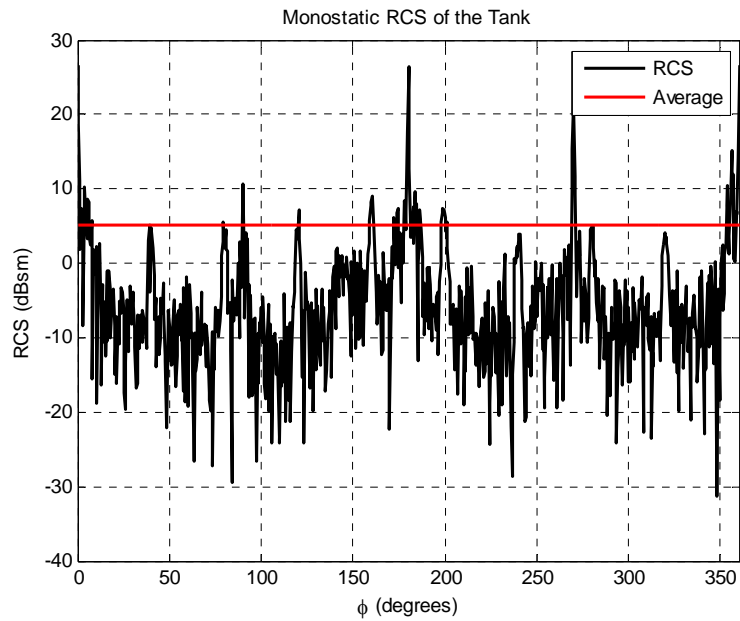
Figure 5-12: Monostatic RCS of the Tank Computed by PO ($\theta = 75°$)
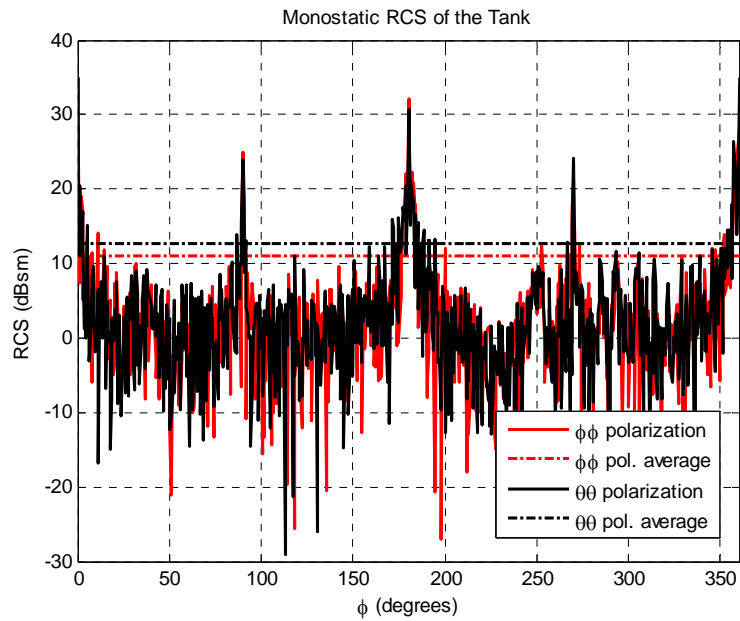
Figure 5-13: Monostatic RCS of the Tank Computed by Modified PO ($\theta = 85°$)

101
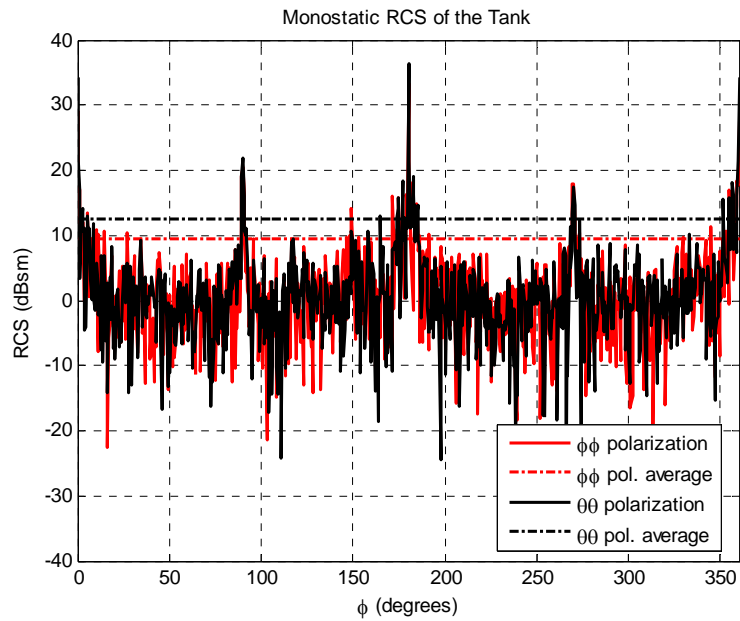
Figure 5-14: Monostatic RCS of the Tank Computed by Modified PO ($\theta = 80^\circ$)
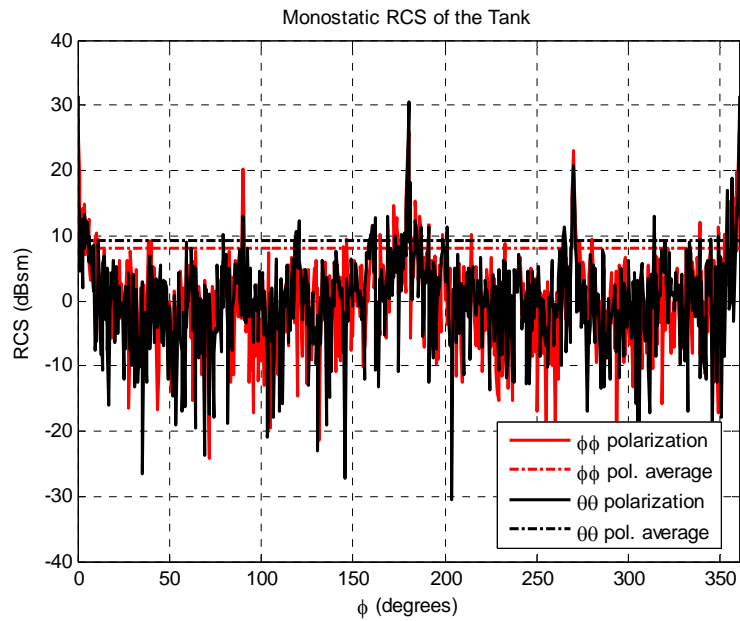

Figure 5-15: Monostatic RCS of the Tank Computed by Modified PO ($\theta = 75^\circ$)

From the figures given above, it may be observed that the RCS values obtained by Modified PO are slightly higher than the values obtained by PO due to the contribution of the diffracted fields. A comparison of the average RCS values attained by these methods is shown in Table 2.

Table 2: Comparison of Average RCS Values Computed by PO and Modified PO

θ	PO	Modified PO	
		$\theta\theta$	$\phi\phi$
85°	12.2 m^2	18.6 m^2	12.6 m^2
80°	9.0 m^2	17.5 m^2	8.9 m^2
75°	3.3 m^2	8.4 m^2	6.4 m^2

It may be concluded from the results given in Table 2 that, the Modified PO solutions for different polarizations are also close to each other. This observation is mainly due to the fact that polarization sensitivity of the targets can only be observed if multiple diffraction mechanisms are included into the electromagnetic solver. Nonetheless, only the first order diffractions can be modeled via Modified PO. Furthermore, it may also be observed that PO and Modified PO results do not differ significantly. Since the tank is modeled by a considerable amount of facets, for each incidence direction there may exist some facets which cause specular reflection. Due to the fact that specular reflection is the most dominant scattering mechanism and is independent of polarization, PO and Modified PO solutions are obtained to be close to each other.

In addition to co-polarized RCS, cross-polarized RCS values of the tank was also computed. Figure 5-16 - Figure 5-18 and Figure 5-19 - Figure 5-24 shows cross-polarized RCS of the tank computed by PO and Modified PO respectively. Since PO is independent of polarization, PO results are given for only one polarization.
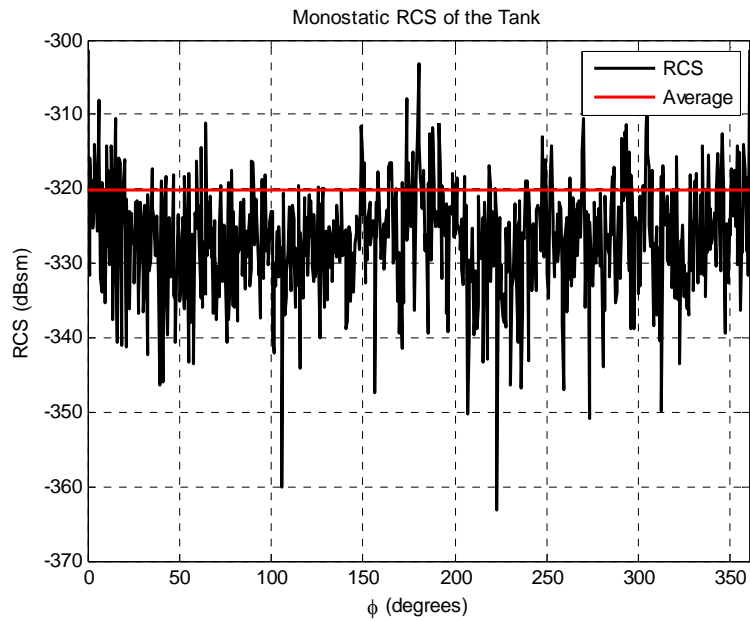
Figure 5-16: Cross Polarized Monostatic RCS of the Tank Computed by PO ($\theta = 85°$)
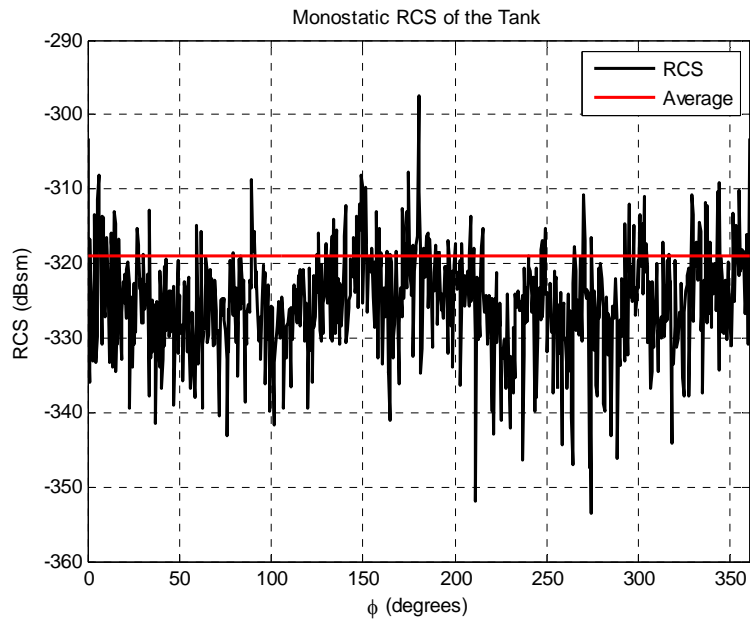
Figure 5-17: Cross Polarized Monostatic RCS of the Tank Computed by PO ($\theta = 80°$)
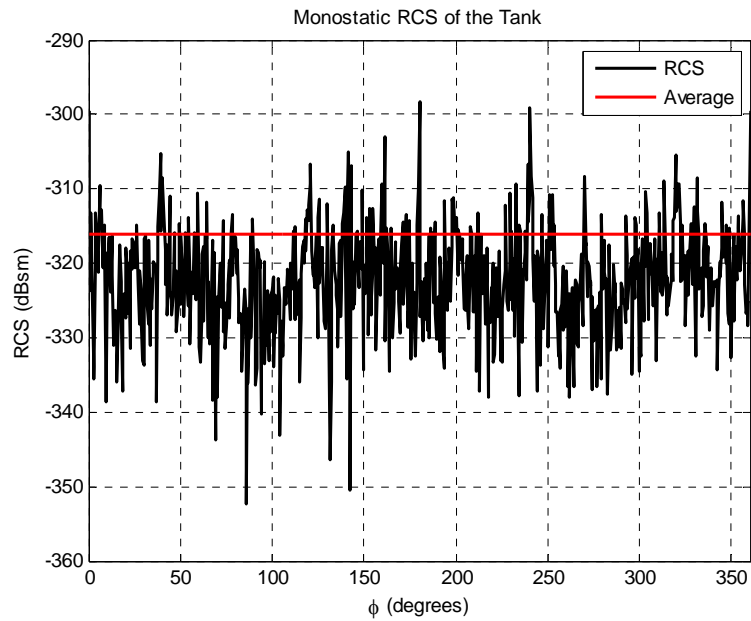
Figure 5-18: Cross Polarized Monostatic RCS of the Tank Computed by PO ($\theta = 75°$)
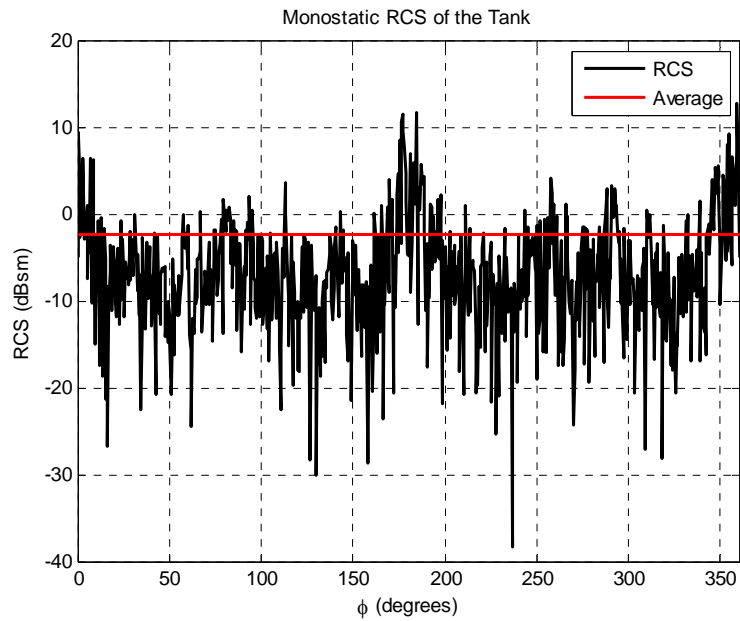
Figure 5-19: Cross Polarized ($\theta\phi$) Monostatic RCS of the Tank Computed by Modified PO

$(\theta = 85°)$
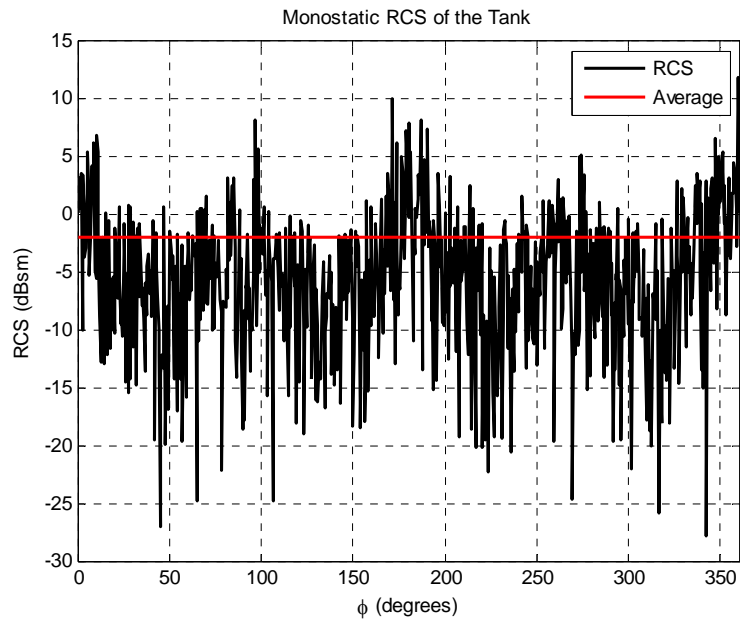
Figure 5-20: Cross Polarized ($\theta\phi$) Monostatic RCS of the Tank Computed by Modified PO

($\theta = 80°$)
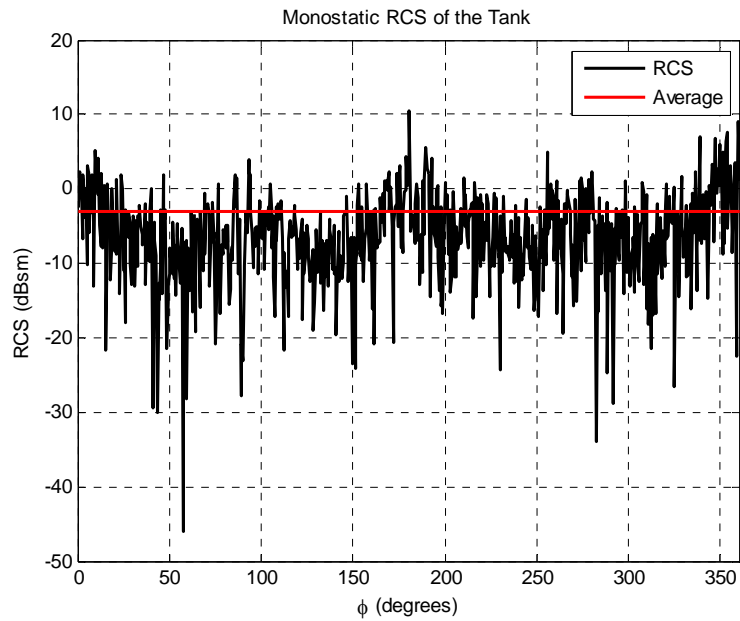
Figure 5-21: Cross Polarized ($\theta\phi$) Monostatic RCS of the Tank Computed by Modified PO

($\theta = 75°$)
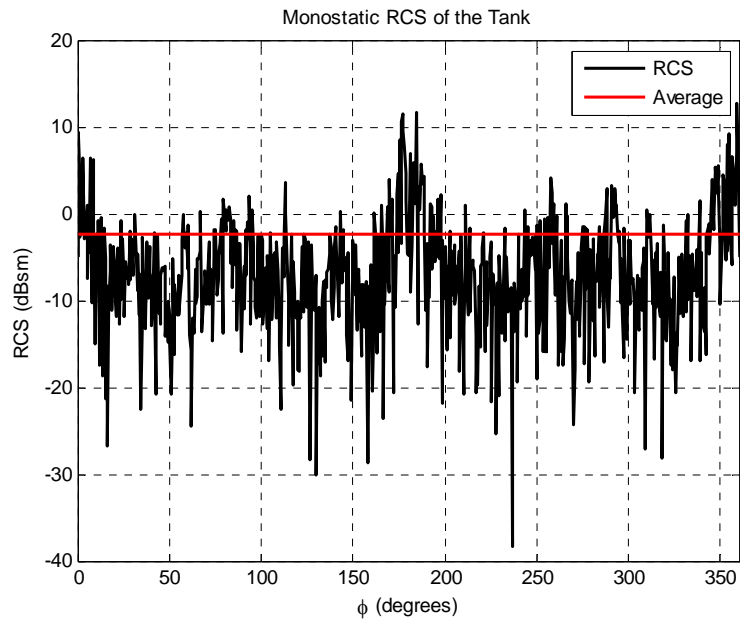
Figure 5-22: Cross Polarized ($\phi\theta$) Monostatic RCS of the Tank Computed by Modified PO
($\theta = 85°$)
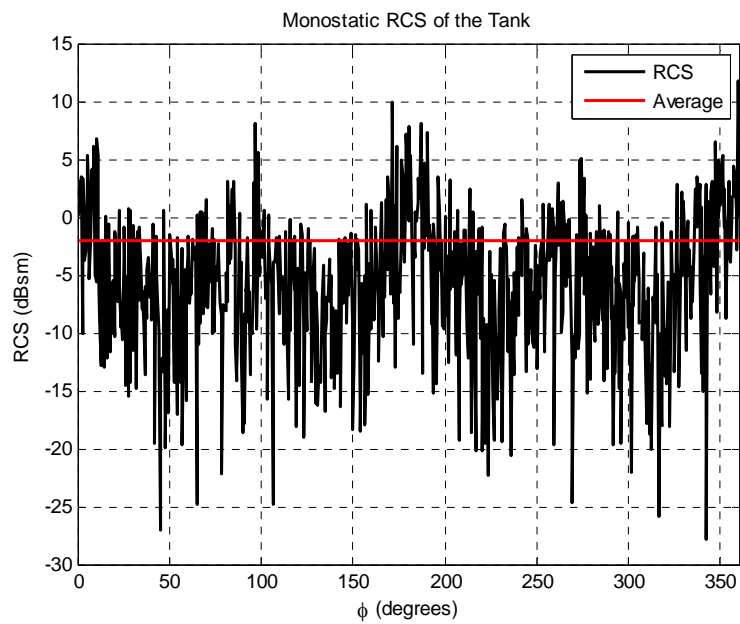
**Figure 5-23: Cross Polarized ($\phi\theta$) Monostatic RCS of the Tank Computed by Modified PO**
($\theta = 80°$)
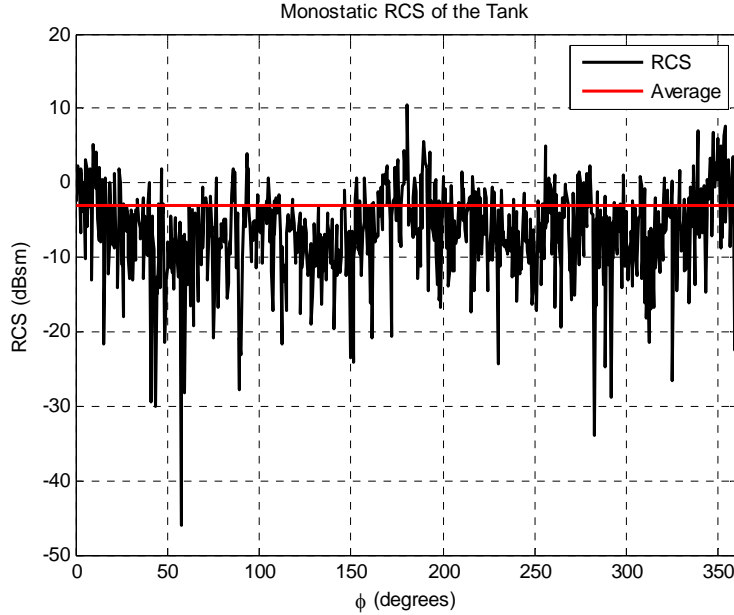
Figure 5-24: Cross Polarized ($\phi\theta$) Monostatic RCS of the Tank Computed by Modified PO
($\theta = 75°$)

In contrast to the co-polarized case, PO and Modified PO results are not close to each other for cross-polarization. In view of the fact that the cross-polarization fields are introduced by diffraction mechanism, PO approach gives almost zero fields. On the other hand, Modified PO approach results in nonzero but relatively small RCS values in comparison with the co-polarized ones. Expectedly, Modified PO results for $\theta\phi$ and $\phi\theta$ polarizations are very close (almost equal) to each other due to not considering multiple diffractions. Also, the difference between these values becomes very insignificant since the strength of the scattered field is low. Table 3 summarizes the statements discussed in this paragraph.

Table 3: Comparison of Average Cross Polarized RCS Values Computed by PO and Modified PO

θ	PO	Modified PO	
		$\theta\phi$	$\phi\theta$
85°	9.6×10^{-33} m^2	0.6 m^2	0.6 m^2
80°	1.3×10^{-32} m^2	0.6 m^2	0.6 m^2
75°	2.4×10^{-32} m^2	0.5 m^2	0.5 m^2

5.1.3 Statistical Analysis

The results given in the previous section show that the RCS values of both simple and complex targets fluctuate in a very dynamic range. In fact, even in the case of two scatterers with the same cross sections, the total RCS fluctuates in a dynamic range too. Moreover, these fluctuations increase with the increasing number of scatterers. This behavior of RCS leads to some statistical studies which result in remarkable outcomes.

If a statistical analysis is conducted on the electromagnetic field scattered by N randomly distributed scatterers with equal cross sections, it can be observed that the real and imaginary parts of the scattered field have "Normal" distributions with same variance. Hence the distributions of magnitude of the field and square of magnitude of the field (or RCS) fit to "Rayleigh" and "Exponential" distributions respectively. In addition to these, the phase of the field has a uniform distribution. (See Appendix B for the proof.) If there are dominant scatterers contributing to the field, then the distribution of the RCS may be modeled by "Chi-square", "Rice", "Weibull" or "Log-normal" distributions [56].

Remember that the RCS computations of the tank were accomplished for 720 different aspect angles. Indeed, changing the aspect angle for RCS computation, corresponds to changing the distribution of the scatterers inside a volume.

Therefore, the histogram of the RCS of the tank computed for different aspect angles gives the distribution of the RCS for randomly distributed scatterers within a volume.

In our case, the tank is modeled by flat facets with individual RCS close to each other so, they may be considered as almost equally weighted scatterers distributed into the volume occupied by the tank. Thus, a normal distribution is expected from the real and imaginary parts of the field scattered by the tank model. However, in order to obtain reliable information about the distribution, the RCS of the tank should be computed for many aspect angles (more than 10000). Since our experiments were conducted for 720 angles, the results attained here cannot give thorough distribution but only an idea about it. Figure 5-25 - Figure 5-27 shows the histograms of the real part, imaginary part, phase, magnitude and magnitude square of the scattered field computed by PO and Modified PO for co-polarized case.
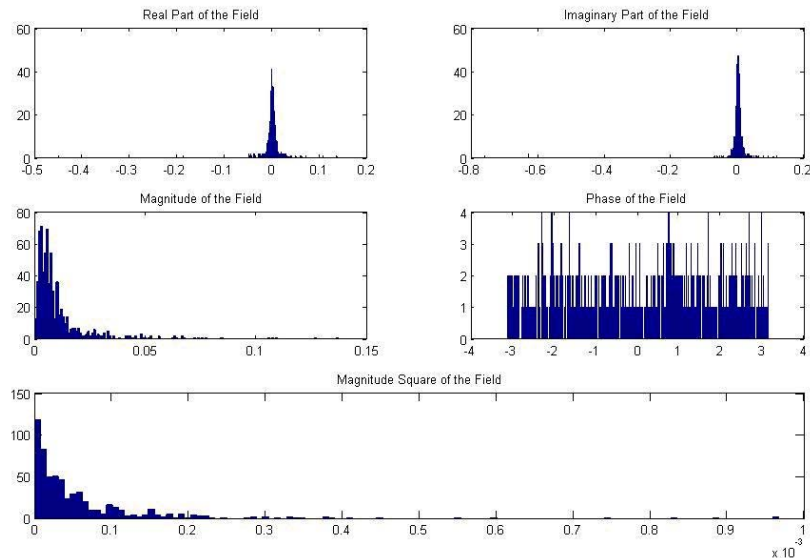
Figure 5-25: Statistical Analysis of the Scattered Field from the Tank Computed by PO
($\theta = 80°$)
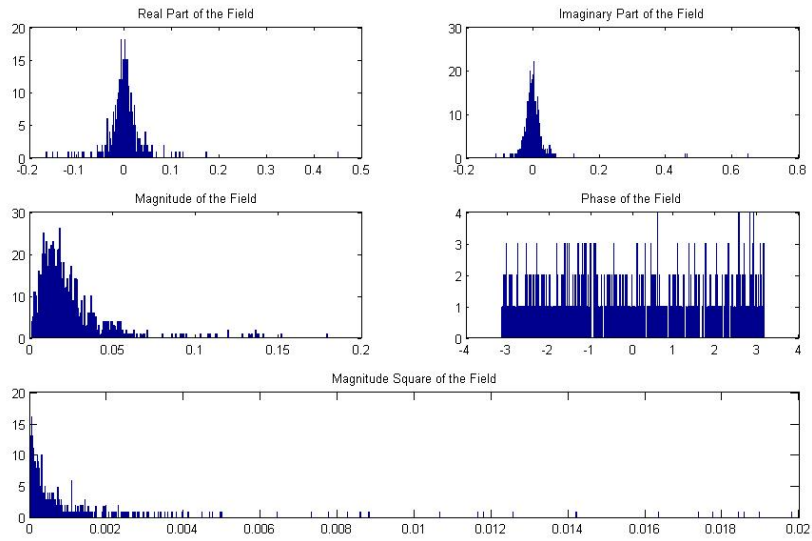
Figure 5-26: Statistical Analysis of the Scattered Field from the Tank Computed by Modified PO ($\theta = 80°$, $\phi\phi$ Polarization)
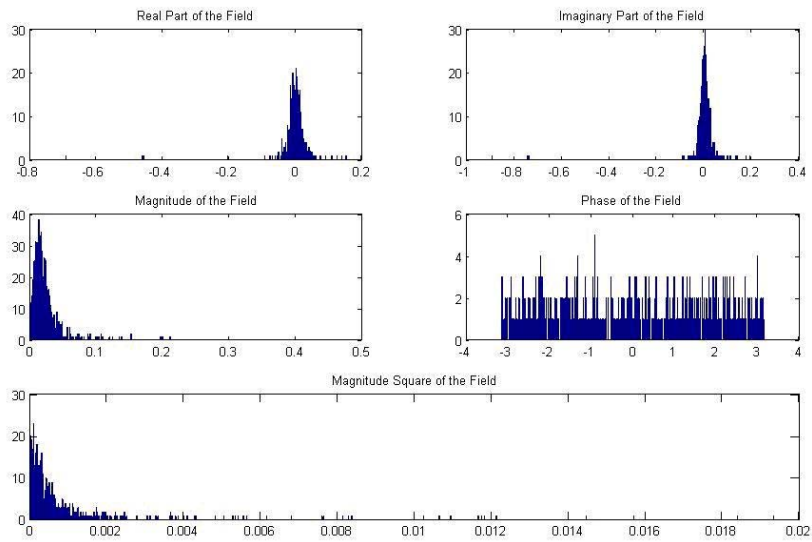
Figure 5-27: Statistical Analysis of the Scattered Field from the Tank Computed by Modified PO ($\theta = 80°$, $\theta\theta$ Polarization)

It can be observed that the results are very close to expected ones. The deviations from the ideal results may be due to facets with very high or very low RCS in comparison with the other facets. On the other hand, the results obtained for cross-polarized case are closer to ideal ones. In the view of the fact that even the large (in terms of RCS) facets generate weak cross-polarized scattered fields, "equally weighted scatterers" model fits to this case better than co-polarized case. The histograms of cross-polarized fields are illustrated in Figure 5-28 - Figure 5-30.
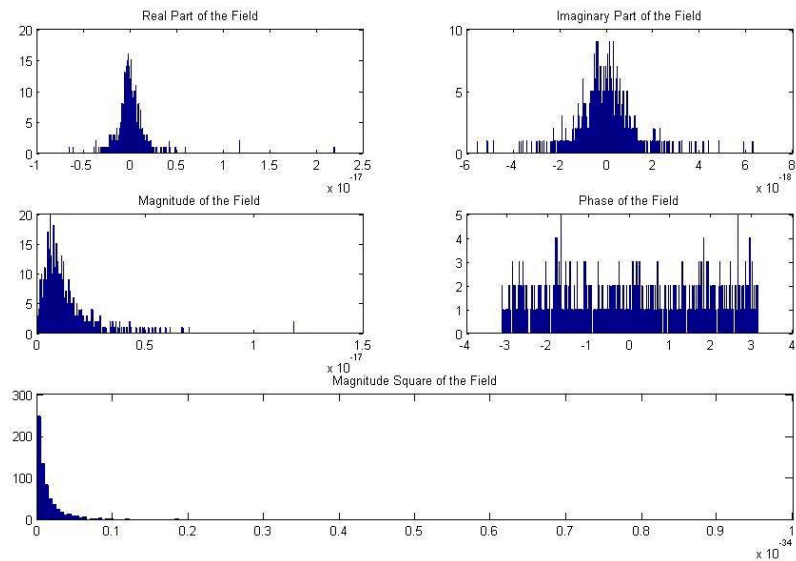
Figure 5-28: Statistical Analysis of the Cross Polarized Scattered Field from the Tank Computed by PO ($\theta = 80°$)
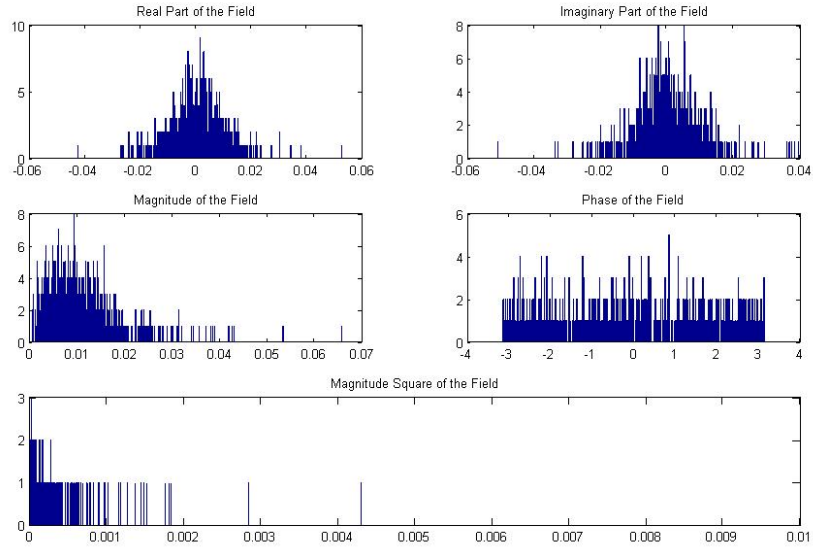
Figure 5-29: Statistical Analysis of the Cross Polarized Scattered Field from the Tank Computed by Modified PO ($\theta = 80°$, $\phi\theta$ Polarization)
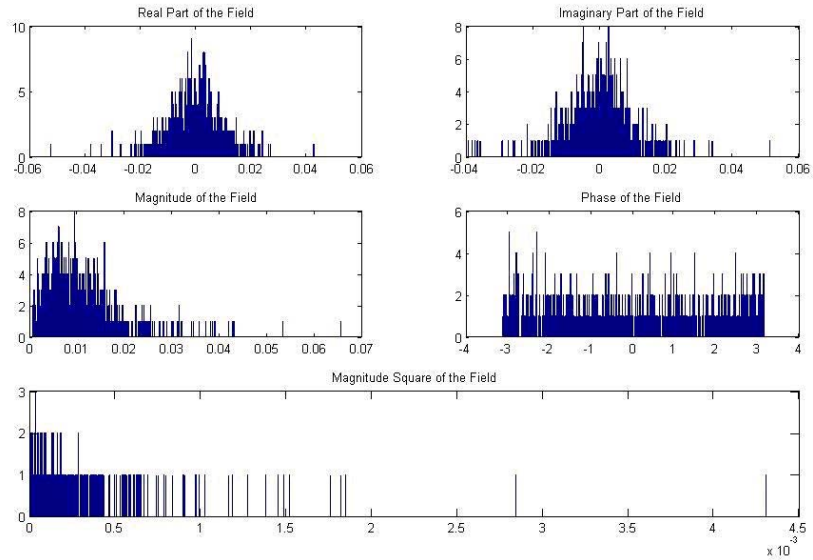
Figure 5-30: Statistical Analysis of the Cross Polarized Scattered Field from the Tank Computed by Modified PO ($\theta = 80°$, $\theta\phi$ Polarization)

113

5.2   Time Domain Experiments

In the time domain experiments, the waveforms scattered from the simple shaped objects used in frequency domain experiments were observed. It was seen that the results are in agreement with discussions given in Chapter-4.

The first experiment was conducted on the cube which is illustrated in Figure 5-1. The cube was illuminated from $\theta = \phi = 45°$ in order to light 3 faces of the cube simultaneously. Figure 5-31 and Figure 5-32 show the scattered waveform for $\theta\theta$ and $\phi\phi$ polarizations respectively. Since there are more than 2 scattering centers in a cube, the number of pulses observed is more than 2.
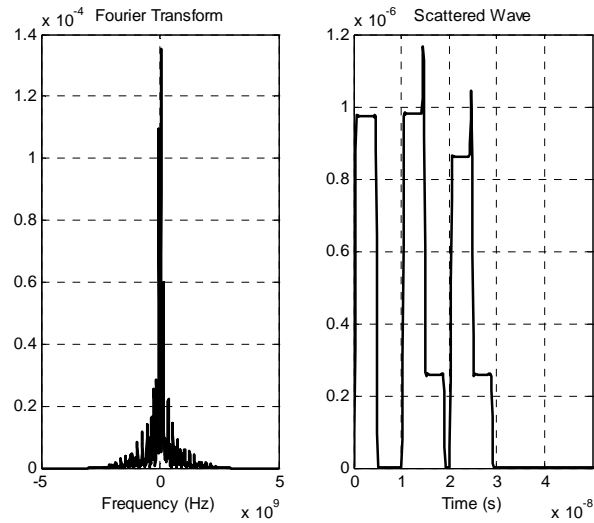
Figure 5-31: Scattered waveform from the Cube ($\theta\theta$ Polarization)
$\theta = 45°$ **and** $\phi = 45°$
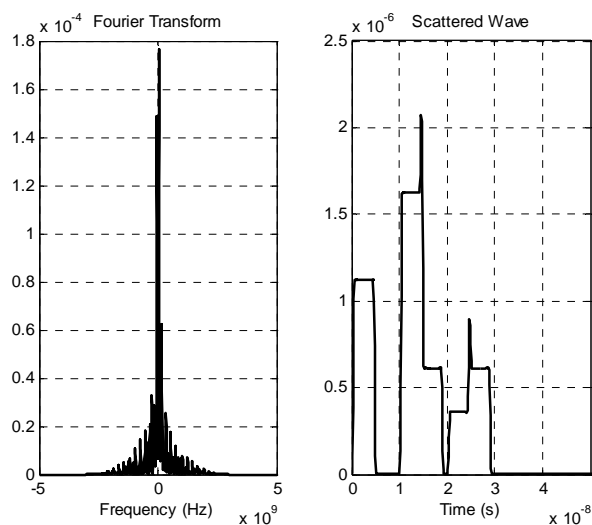
Figure 5-32: Scattered waveform from the Cube ($\phi\phi$ Polarization)

$\theta = 45°$ **and** $\phi = 45°$

For the case of the rectangular prism shown in Figure 5-4, we obtain similar results as they can be seen from Figure 5-33 and Figure 5-34.
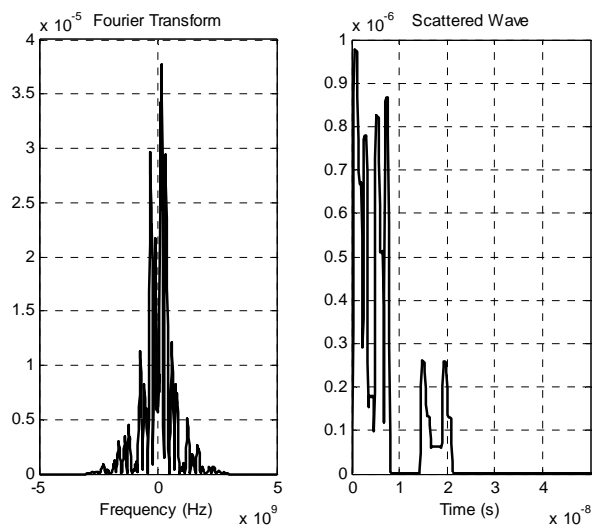
Figure 5-33: Scattered waveform from the Rectangular Prism ($\theta\theta$ Polarization)

$\theta = 45°$ **and** $\phi = 45°$

115
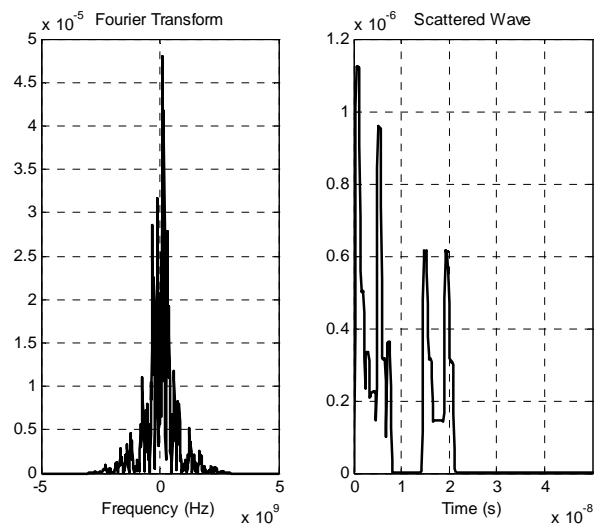
Figure 5-34: Scattered waveform from the Rectangular Prism ($\phi\phi$ Polarization)
$\theta = 45°$ **and** $\phi = 45°$

The main difference between the waveforms scattered from the cube and rectangular prism is the overlapping of the pulses. Since the side lengths of the rectangular prism are not equal to each other, the retardation between the pulses differs from each other resulting in interesting waveforms.

If the cylinder is illuminated from $\theta = 90°$ and $\phi = 90°$, due to the curvature of the surface, the transient effects may be seen clearly. However, for the case of the cylinder shown in Figure 5-7 the transient part of scattered wave is very short when compared with the whole pulse. Since the radius of the cylinder is large (100λ) with respect to the wave length (curvature is small), the cylinder behaves like a flat plate. The results of this experiment are illustrated in Figure 5-35.
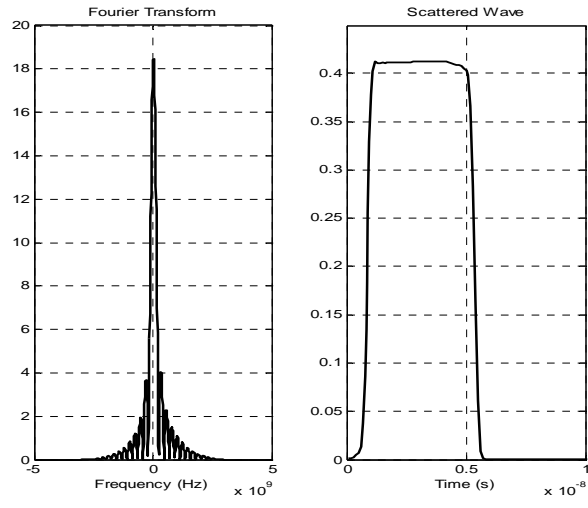
Figure 5-35: Scattered waveform from the Cylinder ($\theta\theta$ Polarization)
$\theta = 90°$ **and** $\phi = 90°$

If the same experiments are repeated with the long pulse used in Chapter-4, similar results are obtained. Nonetheless, the retardation between the pulses scattered from different scattering centers of the targets cannot be observed because of long duration of the incident pulse. The results related to these experiments are illustrated in Figure 5-36 - Figure 5-40.
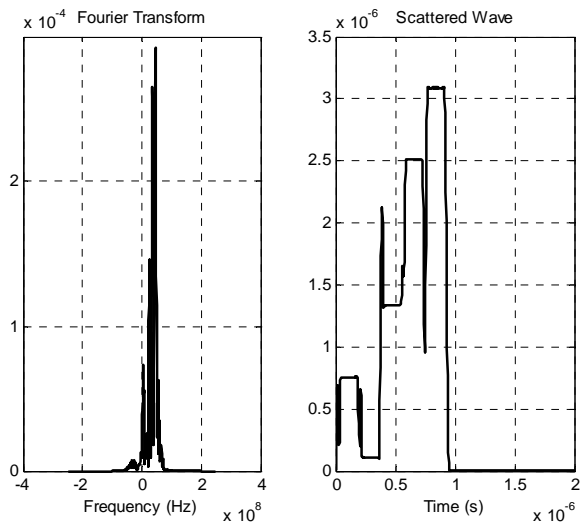
Figure 5-36: Scattered waveform from the Cube ($\theta\theta$ Polarization)
$\theta = 45° $ **and** $\phi = 45°$
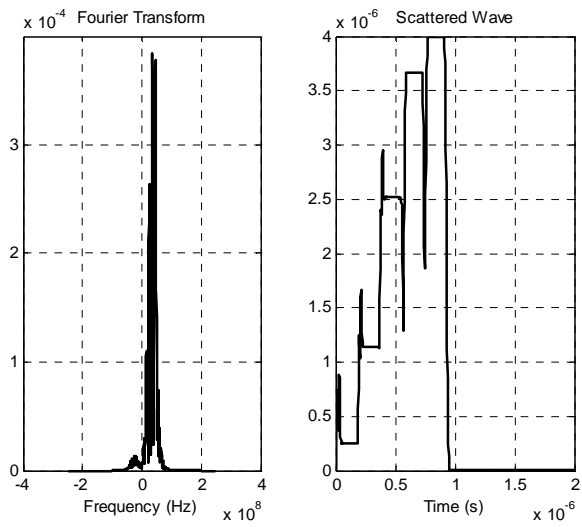
Figure 5-37: Scattered waveform from the Cube ($\phi\phi$ Polarization)
$\theta = 45° $ **and** $\phi = 45°$
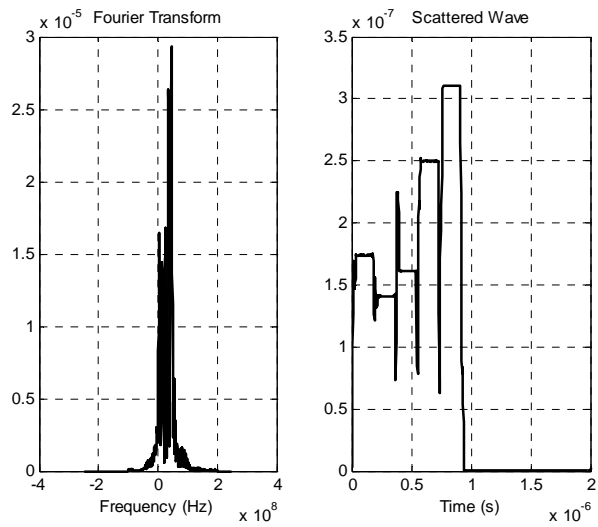
Figure 5-38: Scattered waveform from the Rectangular Prism ($\theta\theta$ Polarization)
$\theta = 45°$ **and** $\phi = 45°$
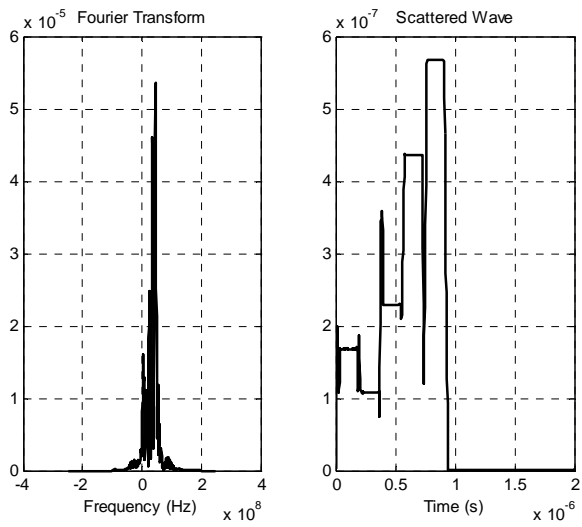
Figure 5-39: Scattered waveform from the Rectangular Prism ($\phi\phi$ Polarization)
$\theta = 45°$ **and** $\phi = 45°$
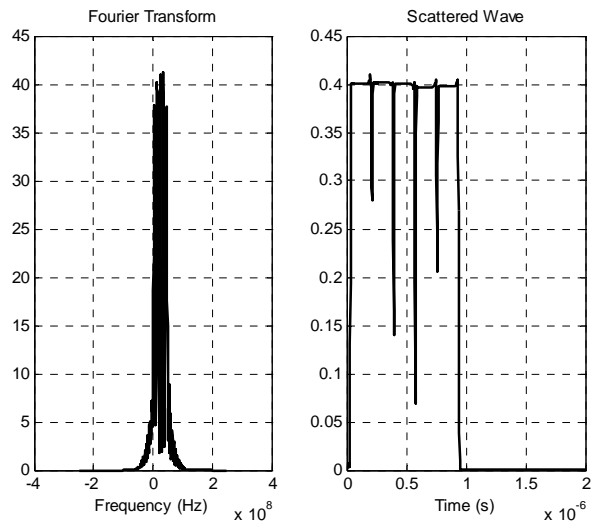
Figure 5-40: Scattered waveform from the Cylinder ($\theta\theta$ Polarization)
$\theta = 90°$ **and** $\phi = 90°$

120

CHAPTER 6

CONCLUSIONS

6.1 Summary of the Thesis

In this thesis a MATLAB® code for RCS computation of complex targets by PO and Modified PO methods is developed.

The most intricate part of RCS computation by PO/Modified PO is the integration part. Since PO is valid at high frequencies, the complex exponential term in the integrand of the PO integral becomes very oscillatory at high frequencies. Hence, too many sampling points are needed with the classical quadrature methods. To increase the computational efficiency of the code, a novel fast integration technique, which is called Levin's integration method, is applied to electromagnetic scattering problems. In this method, an accurate solution can be attained for an integral on a rectangular domain by making use of only a few collocation points. The integrand is approximated by some basis functions (monomials in this study) and the integration is concerted to solving a differential equation with the help of a genius operator. Then a nonoscillatory particular solution of this differential equation is obtained. In order to apply this model to arbitrary shaped objects, the surfaces of the objects are modeled by 8-noded quadrilaterals. Then, with the help of some shape functions, the integration domain is mapped to a rectangular domain where Levin's method is easily applicable.

PO gives accurate results for high frequency scattering problems near specular reflection region. Nonetheless, its performance is not so good for grazing angles. The main reason of this situation is the fact that PO cannot account for diffraction effects that become significant for grazing angles. Thus to improve the performance of PO, a modified version of it is used which also accounts for the primary diffraction effects. In this method, diffraction is modeled by defining new surface normal vectors that generate fictitious surface currents that are functions of incidence and observation directions. By this method, the performance of PO is improved to the level of GTD with a minor modification in the PO integral.

An algorithm which accounts for multiple scattering and shadowing problems is also included into the code. IPO algorithm is used to account for multiple scattering effects. This method is more efficient in comparison with Shooting and Bouncing Rays method. In this technique, PO surface currents are reradiated to calculate the secondary fields scattered by the object. If higher order scattering effects are desired to be observed, then the surface currents should be reradiated iteratively until it converges. A useful consequence of this method is that, it solves shadowing problem automatically by making use of a slight modification in the shadowing conditions of the IPO. However, a considerable amount of facets are needed to obtain accurate results with this method which makes it computationally expensive. Therefore, this method is more appropriate for parallel computing.

In addition to frequency domain solutions, to see the transient effects on the scattered waveforms, a time domain analysis is also accomplished. For this purpose, a Fourier domain approach is employed instead of a direct time domain technique because of lack of a fast direct time domain solver. To increase the computational efficiency of the method, sampling rate is decreased by investigating the envelopes of the waveforms only. By this way, the high frequency signals are carried to low frequency level where the Nyquist rate is dramatically lower than the rate in the high frequency region.

Finally, the implemented methods are applied to some simple and complex targets in both frequency and time domains and the results are compared with other techniques. In addition to these, a statistical analysis of the scattered fields from the tank model is included into the thesis.

6.2 Advantages and Disadvantages of the Levin's Method

Levin's method is an efficient and fast way to compute the integrals with rapid oscillations. Since it can be applied to curved surfaces, the number of patches used for target modeling can be decreased drastically. Hence, computational efficiency of Levin's method is higher than the methods using planar patches to model the targets. Moreover, the complexity of the algorithm is almost of order zero with respect to frequency. That is the number of computations and CPU time does not change with frequency. Therefore, very large facets (such as facets with a surface area of $10000\lambda^2$) may be used for target modeling. This makes Levin's method appropriate for large targets like ships, planes and tanks.

Despite the advantages of Levin's method, there are some drawbacks restricting the usage of it. Due to the possible singularities stated in the thesis, Levin's method cannot be applied to PO integrals at low frequencies. Since a rapid phase variation within a facet is also necessary for the application of the method, small facets are not appropriate for this technique. Thus, for some case the geometry of a target may not be modeled precisely. Furthermore, Levin's method is not applicable to compute the scattered fields in the neighborhood of forward scattering region because of the same reason.

6.3 Advantages and Disadvantages of Modified PO

Modified PO is a simple method to model the diffraction effects without making use of any diffraction coefficients or edge currents. The diffraction effects can be accounted by computing the same number of integrals as in the PO method.

Therefore, CPU time needed is not increased significantly in comparison with PO. However, multiple diffraction effects are not modeled by Modified PO. In the view of the fact that the polarization dependency of RCS is introduced by multiple diffraction mechanism, Modified PO should be improved further for the investigation of the polarization sensitivity of targets.

Modified PO is mathematically proven to be an accurate method to improve the performance of PO for diffraction up to the level of GTD for 2D problems. Nevertheless, a more rigorous formulation should be developed to apply this method to arbitrarily shaped 3D objects.

6.4   Future Work

The performance of Levin's method is satisfactory in terms of computational aspects. However, the computation time of the code can be decreased further by accomplishing a code optimization. Moreover, a parallel computing algorithm may be developed for this program. In fact, there is no need for superfluous communication between the computers since the total scattered field is computed by the superposition of the fields scattered from each facet. Thus, the parallelization of the algorithm may be done effortlessly and improves the performance of the code dramatically.

For the sake of simplicity, planar facets are used to model complex targets in this study. Therefore, a special mesh generation algorithm that models the targets by curved patches may be developed. By this way a complete software package for RCS prediction at high frequencies will be obtained.

In this thesis, monomials are used as basis functions in the integration part. The use of other basis functions may be investigated and a comparison of the performance of the Levin's method for different basis functions may be done.

Indeed, there is a strong intuition that if Bernstein polynomials are used as basis functions, Levin's method may be applied to surfaces modeled by NURBS.

Finally, Levin's method may be applied to direct time domain integrals to decrease the computation time and memory requirements of TDPO. If the time retardation is rewritten as a function of spatial coordinates of the integration surface, then TDPO integral may be computed by storing the field values at the collocation points only. By this way time needed for interpolations can also be decreased.

REFERENCES

[1]   Knott E.F., "A Progression of High-Frequency RCS Prediction Techniques", *Proceedings of IEEE, Vol.73 No.2, February 1985*

[2]   Bhattacharyya A.K., Sengupta D.L., "Radar Cross Section Analysis and Control", *Artech House Boston London 1991, p:108*

[3]   Jenn D.C., "Radar and Laser Cross Section Engineering", *AIAA Education Series Washington DC 1995, p:11*

[4]   Knott E.F., Shaeffer J.F., Tuley M.T., "Radar Cross Section" *Artech House Boston London 1993, p:124*

[5]   Plonus M.A., Williams R., Wang S.C.H., "Radar Cross Section of Curved Plates Using Geometrical and Physical Diffraction Techniques", *IEEE Transactions on Antennas and Propagation, Vol. AP-26 No.3, May 1978*

[6]   Medgyesi-Mitschang L.N., Wang D., "Hybrid Methods for Analysis of Complex Scatterers", *Proceedings of IEEE, Vol.77 No.5, May 1989*

[7]   Allen C.C., "Numerical Integration Methods for Antenna Pattern Calculations", *IRE Transactions on Antennas and Propagation, Vol. 9 Issue.4,December 1959*

[8]   Burkholder R.J., Lee T., "Adaptive Sampling for Fast Physical Optics Numerical Integration", *IEEE Transactions on Antennas and Propagation, Vol.53 No.5, May 2005*

[9] Moreira F.J.S., Prata A., "A Self-Checking Predictor-Corrector Algorithm for Efficient Evaluation of Reflector Antenna Radiation Integrals", *IEEE Transactions on Antennas and Propagation, Vol.42 No.2, January 1994*

[10] Kobayashi H., Hongo K., Tanaka I., "Expressions of Physical Optics Integral for Smooth Conducting Scatterers Approximated by Quadratic Surfaces", *Electronics and Communication in Japan, Part 1, Vol.83, No.7, 2000*

[11] Flinn E.A., "A Modification of Filon's Method of Numerical Integration", *Journal of the ACM, Vol.7, Issue 2, April 1960*

[12] Crabtree G.D., "A Numerical Quadrature Technique for Physical Optics Scattering Analysis", *IEEE Transactions on Magnetics, Vol.27, No.5, September 1991*

[13] Vico F., Ferrando M., Baquero M., Antonino E., "A New 3D Fast Physical Optics Method" *IEEE Antennas and Propagation Society International Symposium 2006, 9-14 July 2006, pp:1849-1852*

[14] Levin D., "Procedures for Computing One and Two Dimensional Integrals of Fumctions With Rapid Irregular Oscillations", *American Mathematical Society, April 1982 pp:531-538.*

[15] Kuzuoğlu M., "Solution of Electromagnetic Boundary Value Problems by the Plane Wave Enriched FEM Approach", *IEEE APS-URSI International Symposium, 2003.*

[16] Taylor C., Hughes T.G., "Finite Element Programming of the Navier-Stokes Equations", *Pineridge Press, 1981*

[17] Ross R.A., "Radar Cross Section of Rectangular Flat Plates as a Function of Aspect Angle", *IEEE Transactions on Antennas and Propagation, Vol.AP-14 No.3, May 1966*

[18] Knott E.F., Shaeffer J.F., Tuley M.T., "Radar Cross Section" *Artech House Boston London 1993, pp:89-90*

[19]   Gordon W.B., "High Frequency Approximations to the Physical Optics Scattering Integral", *IEEE Transactions on Antennas and Propagation, Vol.42 No.3, March 1994*

[20]   Shijo T., Rodriguez L., Ando M., "Accuracy Demonstration of Physical Optics with Modified Surface Normal Vectors", *Antennas and Propagation Society International Symposium 2006, 9-14 July 2006, pp:1873-1876*

[21]   Oodo M., Murasaki T., Ando M., "Uniform Diffraction Coefficients of Physical Optics for Impedance Surfaces", *Antennas and Propagation Society International Symposium 1993, 28 June-2 July 1993, pp:1730-1733, Vol.3*

[22]   Umul Y.Z., "Modified Theory of Physical Optics", *Optics Express, Vol.12 No.20, October 2004*

[23]   Omaki N., Rodriguez L., Shijo T., Ando M., "Accuracy Check of the PO with Modified Surface Normal Vectors for Radar Cross Section Analyses", *International URSI Commission B Electromagnetic Theory Symposium 2007, 26-28 July 2007*

[24]   Ufimtsev P.Y., "Fundamentals of Physical Theory of Diffraction", *John Wiley & Sons New Jersey 2007, p:84*

[25]   Balanis C.A., "Advanced Engineering Electromagnetics", *John Wiley & Sons USA 1989, pp:803-805*

[26]   Youssef N.N., "Radar Cross Section of Complex Targets", *Proceedings of the IEEE, Vol.77 No.5, May 1989*

[27]   Dos Santos M.L.X., Rabelo N.R., "On the Ludwig Integration Algorithm for Triangular Subregions", *Proceedings of the IEEE, Vol.74 No.10, October 1986*

[28]   Tanaka I., Kobayashi H., Mori Y., Moriyama T., Hongo K., Ishikawa S., "RCS Code for Large Obstacles Using PTD-TC", *Microwave Conference 2001 Asia-Pacific, 3-6 December 2001, pp:573-576, Vol.2*

[29]   Molinet F., George T., Brun J.M., Untersteller L.P., "Description of a General Computer Program for RCS Computation of Complex Shapes Described by a CAD System, Founded on GTD/UTD", *Antennas and Propagation Society International Symposium 1992, 18-25 July 1992, pp:1462-1465, Vol.3*

[30]   Perez J., Catedra M.F., "RCS of Electrically Large Targets Modeled with NURBS Surfaces", *Electronic Letters, Vol.28 No.12, June 1992*

[31]   Sefi S., Oppelstrup J., "Physical Optics and NURBS for RCS Calculations", *Technical Report of the project General Electromagnetic Solvers at Parallel and Scientific Computing Institute Royal Institute of Technology Sweden*

[32]   Ling H., Chou R., Lee S., "Shooting and Bouncing Rays: Calculating the RCS of an Arbitrarily Shaped Cavity", *IEEE Transactions on Antennas and Propagation, Vol.37 No.2, February 1989*

[33]   Saez de Adana F., Diego I.G., Blanco O.G., Lozano P., Catedra M.F., "Method Based on Physical Optics for the Computation of the Radar Cross Section Including Diffraction and Double Effcets of Metallic and Absorbing Bodies Modeled With Parametric Surfaces", *IEEE Transactions on Antennas and Propagation, Vol.52 No.12, December 2004*

[34]   Catedra M.F., Delgado C., Luceri S., Blanco O.G., Saez de Adana F., "Physical Optics Analysis of Multiple Interactions in Large Scatters Using Current Modes", *IEEE Transactions on Antennas and Propagation, Vol.54 No.3, March 2006*

[35]   Boag A., Michielssen E., "A Fast Physical Optics Algorithm for Double-Bounce Scattering", *IEEE Transactions on Antennas and Propagation, Vol.52 No.1, January 2004*

[36] Obelleiro-Basteiro F., Rodriguez J.L., Burkholder R.J., "An Iterative Physical Optics Approach for Analyzing the Electromagnetic Scattering by Large Open-Ended Cavities", *IEEE Transactions on Antennas and Propagation, Vol.43 No.4, April 1995*

[37] Dehmollaian M., Sarabandi K., "Electromagnetic Scattering From Foliage Camouflaged Complex Targets", *IEEE Transactions on Geoscience and Remote Sensing, Vol.44 No.10,October 2006*

[38] Grana M., Arias M., Rubinos O., Garcia-Pino A., Martinez-Lorenzo J.A., "Iterative Physical Optics Solution for MFIE on Dual Reflector Antennas", *International URSI Commission B Electromagnetic Theory Symposium 2007, 26-28 July 2007*

[39] Albayrak N.A., "RCS Computations With PO/PTD for Conducting and Impedance Objects Modeled as Large Flat Plates", *MS Thesis Bilkent University Ankara, July 2005*

[40] Lozano L., Hernandez M.I., Romera C., Gonzalez I., Saez de Adana F., Catedra M.F., "Ray Tracing Acceleration Techniques to Compute RCS of Complex Targets", *Antennas and Propagation Society International Symposium 2004, 20-25 June 2004, pp:4495-4498, Vol.4*

[41] Turner S.D., "RESPECT: Rapid Electromagnetic Scattering Predictor for Extremely Complex Targets", *IEE Proceedings, Vol.137 Pt. F. No.4, August 1990*

[42] Andrade L.A., Nohara E.L., Peixoto G.G., Rezende M.C., Martin I.M., "Backscattering Analysis of Flat Plate and Dihedral Corner Reflectors Using PO and Comparison With RCS Measurements in Anechoic Chamber", *Microwave and Optoelectronics Conference 2003, Proceedings of the 2003 SBMO/IEEE MTT-S International, 20-23 September 2003, pp:719-724, Vol.2*

[43] Griesser T., Balanis C.A., "Backscatter Analysis of Dihedral Corner Reflectors Using Physical Optics and the Physical Theory of Diffraction", *IEEE Transactions on Antennas and Propagation, Vol. AP-35 No.10, October 1987*

[44]   Sun E.Y., "Transient Analysis of Large Paraboloidal Reflector Antennas", *IEEE Transactions on Antennas and Propagation, Vol.43 No.12, December 1995*

[45]   Chou H.T., Tuan S.C., "Analytic Analysis of Transient Scattering From a Finite Second-Order Surface Illuminated by an Incident Plane Wave", *IEEE Transactions on Antennas and Propagation, Vol.54 No.9, September 2006*

[46]   Oliveira R., Helier M., "Closed Form Expressions of the Avial Step and Impulse Responses of a Parabolic Reflector Antenna", *IEEE Transactions on Antennas and Propagation, Vol.55 No.4, April 2007*

[47]   Miller E.K., Landt J.A., "Direct Time-Domain Techniques for Transient Radiation and Scattering from Wires", *Proceedings of IEEE, Vol.68 No.11, November 1980*

[48]   Sun E.Y., Rusch W.V.T., "Time-Domain Physical-Optics", *IEEE Transactions on Antennas and Propagation, Vol.42 No.1, January 1994*

[49]   Lee S.W., Jeng S.K., Yu C.L., Liang C.S., Shepherd R.A., "Physical Optics Impulse Response From Faceted Targets", *Antennas and Propagation Society International Symposium 1992, 18-25 July 1992, pp:1456-1459, Vol.3*

[50]   Skinner B.J., Donohoe J.P., Ingels F.M., "Simulation of Target Responses to High Frequency Ultra Wideband Radar Signals Using the Physical Optics Impulse Response", *Proceedings of Twenty-Fifth Southeastern Symposium on System Theory, pp:11-15, 7-9 March 1993*

[51]   Bölükbaş D., Ergin A.A., "A Radon Transform Interpretation of the Physical Optics Integral", *Microwave and Optical Technology Letters, Vol.44 No.3, February 2005*

[52]   Houshmand B., Rahmat-Samii Y., Duan D.W., "Time Response of Single and Dual Reflector Antennas", *Antennas and Propagation Society International Symposium 1992, 18-25 July 1992, pp:1161-1164, Vol.2*

[53]   Kashyap S., Stanier J., Painchaud G., Louie A., "Radar Response of Missile-Shaped Targets", *Antennas and Propagation Society International Symposium 1992, 18-23 June 1995, pp:1910-1913, Vol.4*

[54]   Knott E.F., Shaeffer J.F., Tuley M.T., "Radar Cross Section" *Artech House Boston London 1993, p:144*

[55]   Skolnik M.I., "Introduction to Radar Systems", *McGraw-Hill Higher Education 3rd Edition Singapore 2001 p:179*

[56]   Richards M.A., "Fundamentals of Radar Signal Processing" *McGraw-Hill United States 2005, pp:67-79*

APPENDIX A

PROOF OF LEVIN'S THEOREM

The proof of Levin's theorem given in [14] is as follows:

We would like to show that under the aforementioned conditions the differential equation given in (2.17) has a slowly oscillatory particular solution p_0.

$$L^{(1)}(p) = p' + jq'p = f \tag{A.1}$$

Let $q(x) = Wu(x)$ where $0 < |u'(x)| \leq 1$ and let $x(\zeta)$ be the inverse of $u(x)$ where $u(a) \leq \zeta \leq u(b)$. Since the functions f and q are slowly oscillatory functions, $f(x(\zeta))\big/q'(x(\zeta))$ is also slowly oscillatory and therefore its spectrum is bounded.

$$\frac{f(x(\zeta))}{q'(x(\zeta))} = \int_{-W_0}^{W_0} G(w)e^{jw\zeta}\,dw \tag{A.2}$$

where $0 < W_0 \leq W$.

Then the slowly oscillatory particular solution of (A.1) is found to be

$$p_0(x) = W \int_{-W_0}^{W_0} \frac{G(w)e^{jwu(x)}}{j(w+W)} dw \tag{A.3}$$

This can be verified by computing

$$L^{(1)} p_0(x) = p_0'(x) + jq'(x)p_0(x) \tag{A.4}$$

$$\Rightarrow L^{(1)} p_0(x) = W \int_{-W_0}^{W_0} \frac{G(w)}{j(w+W)} \left(jwu'(x)e^{jwu(x)} + jWu'(x)e^{jwu(x)} \right) dw \tag{A.5}$$

$$\Rightarrow L^{(1)} p_0(x) = q'(x) \int_{-W_0}^{W_0} G(w)e^{jwu(x)} dw = q'(x)\frac{f(x(u(x)))}{q'(x(u(x)))} = f(x) \tag{A.6}$$

The particular solution given in (A.3) is slowly oscillatory in comparison with $e^{jq(x)}$ since its spectrum is bounded in $[-W_0, W_0]$ and $W_0 \ll W$.

134

APPENDIX B

STATISTICAL ANALYSIS FOR COMPLEX RANDOM VARIABLES

Consider a complex random variable $\tilde{z} = \tilde{x} + j\tilde{y}$ where $\tilde{x}$ and $\tilde{y}$ are independent normally distributed random variables with same variance σ. Then the probability density function for these variables can be written as

$$f_d(x, y) = \frac{1}{2\pi\sigma^2} e^{\frac{-1}{2\sigma^2}(x^2+y^2)} \tag{B.1}$$

Then the probability for being in an arbitrary infinitesimal rectangle is

$$P(x < \tilde{x} < x + dx, y < \tilde{y} < y + dy) = \frac{1}{2\pi\sigma^2} e^{\frac{-1}{2\sigma^2}(x^2+y^2)} dxdy \tag{B.2}$$

If we define 2 new random variables $\tilde{r} = |\tilde{z}| = \sqrt{\tilde{x}^2 + \tilde{y}^2}$ and $\tilde{\psi} = \tan^{-1}\frac{\tilde{y}}{\tilde{x}}$, then the probability given in (B.2) can be rewritten as

$$P = \frac{1}{2\pi\sigma^2} e^{\frac{-1}{2\sigma^2}r^2} rdrd\psi \tag{B.3}$$

Then the probability density function may be expressed as

$$f(r,\psi) = \frac{r}{2\pi\sigma^2} e^{\frac{-1}{2\sigma^2}r^2} = f_{\tilde{r}}(r)f_{\tilde{\psi}}(\psi) \tag{B.4}$$

where

$$f_{\tilde{r}}(r) = \frac{r}{\sigma^2} e^{\frac{-1}{2\sigma^2}r^2} \tag{B.5}$$

$$f_{\tilde{\psi}}(\psi) = \frac{1}{2\pi} \tag{B.6}$$

The probability density functions given in (B.5) and (B.6) are the density functions for Rayleigh and uniform distributions respectively.